Structural and Functional Aspects of the Paradoxical ClpP Modulation by Peptidomimetic Boronate Compounds

Dissertation

Submitted to the Faculty of Mathematics, Informatics and Natural Sciences of the University of Hamburg, Department of Chemistry, for the acquisition of the Doctorate of Natural Sciences (Dr. rer. nat.)

by

Bruno Alves França

Hamburg, 2024

Reviewers:

First reviewer: **Prof. Dr. Dr. Christian Betzel**, University of Hamburg, Institute for Biochemistry and Molecular Biology, Department of Chemistry; Hamburg, Germany.

Second reviewer: **Prof. Dr. Holger Rohde**, University Medical Center Hamburg-Eppendorf, Institute for Medical Microbiology, Virology, and Hygiene; Hamburg, Germany.

Committee Members:

1st Member: **Prof. Dr. Dr. Christian Betzel**, University of Hamburg, Institute for Biochemistry and Molecular Biology, Department of Chemistry; Hamburg, Germany.

2nd Member: **Dr. Thomas Hackl**, University of Hamburg, Department of Chemistry, Scientific Services, NMR Spectroscopy; Hamburg, Germany.

3rd Member: **Prof. Dr. Ralph Holl**, University of Hamburg, Institute of Organic Chemistry, Department of Chemistry; Hamburg, Germany.

Disputation: 20.09.2024
Druckfreigabe: 01.11.2024

I: Publications

Publication as the main author:

1. Alves França, B. et al. (2024). Molecular insights into the dynamic modulation of bacterial ClpP function and oligomerization by peptidomimetic boronate compounds. Scientific Reports, 14 (1).

Contribution as one of the co-authors:

2. Srinivasan, V. et al. (2022). Antiviral activity of natural phenolic compounds in complex at an allosteric site of SARS-CoV2 papain-like protease. Communications Biology, 5 (1).

3. Günther, S. et al. (2021). X-ray screening identifies active site and allosteric inhibitors of SARS-CoV-2 main protease, Science, 372.

II: Table of Contents

III: Abbreviations

Asn – Asparagine

ClpP – Caseinolytic protease P subunit (protein)

clpP – Caseinolytic protease P subunit (encoding gene)

ΔH - Variation of enthalpy

ΔG - Variation of Gibbs free energy

DLS - Dynamic-light scattering

Gly - Glycine

IMAC - Immobilized metal affinity chromatography

ITC - Isothermal titration calorimetry

LB - Luria-Bertani medium

Leu – Leucine

Met – Methionine

MPD – 2-Methyl-2,4-penthanediol

MSA – Multiple sequence alignment

NaOAc – Sodium acetate

Native-PAGE - Native polyacrylamide gel electrophoresis

nanoDSF - Nano differential scanning fluorimetry

Ni-NTA – Nickel-nitrilotriacetic acid

PIPES - 1,4-Piperazinediethanesulfonic acid

R_h or R_H - Hydrodynamic radius in the context of DLS measurements

R_G - Radius of gyration in the context of SAXS and SEC-SAXS measurements

SAXS - Small-angle X-ray scattering

SDS-PAGE - Sodium dodecyl sulfate-polyacrylamide gel electrophoresis

SEC - Size exclusion chromatography

SEC-SAXS - Size exclusion chromatography coupled with small-angle X-ray scattering

SOC - Super optimal medium with catabolic repressor

TB - Transformation buffer used to prepare chemically competent cells. TB can also mean "Terrific Broth", a type of medium for bacterial culturing.

T_M - Melting temperature in the context of nanoDSF

Trp - Tryptophan

Tyr - Tyrosine

Abstract

The low availability of novel antibiotics and the spread of multi-resistant organisms create a severe situation worldwide. Each year, many individuals perish or develop serious disabilities due to persistent infections that conventional antimicrobial chemotherapies cannot treat. This reality also places economic pressure on governments, as strategies to cope with this burden in the public health system demand high investments.

Efforts to promote better management of this scenario involve preventive measures to promote the rational use of antimicrobials in daily life, from hospitals to agriculture. Data from several international agencies show that adopted measures and policies have been effective in recent years, helping to control the rise of new resistant strains, especially in developed countries. Unfortunately, in undeveloped and developing regions, the dramatic reality serves as a reminder that much work remains to be done.

Similarly, plans for producing new drugs are needed. Over the last decades, only a restricted portfolio of antibiotics has been available for hard-to-treat microbial diseases. For some of these drugs, like vancomycin, resistance has already been detected in certain environments.

Some *Staphylococci* are found among resistant organisms. *Staphylococcus aureus* (*Sa*) and *Staphylococcus epidermidis* (*Se*) strains, commensal organisms found on skin and mucosa, can affect immunocompromised and long-term hospitalized patients with persistent nosocomial infections. Besides that, some *Staphylococci* also have the potential to build biofilms that shield them against antibiotics effective upon metabolically active cells in the bloodstream. However, studies involving caseinolytic protease P subunit (ClpP) unveil that this enzyme is a promising drug-target macromolecule for eliminating multi-resistant and dormant *Staphylococci*.

ClpP is an endopeptidase that forms a proteolytic machine with chaperones from the AAA+ (ATPases associated with diverse cellular activities) superfamily. This machine plays an important role in bacterial protein homeostasis, keeping a controlled proteolysis in the cytosol. This control is performed by the chaperones since they make the ClpP's catalytic chamber accessible to selected substrates– unfolded, misfolded, and regulatory proteins – to be degraded. Nevertheless, in

recent years, it has been discovered that natural and synthetic molecules mimic the ATPases, dysregulating the ClpP function and unleashing extensive and promiscuous proteolysis in the intracellular milieu, which leads bacteria to death by self-digestion. On the contrary, other compounds bind to the ClpP's catalytic sites, inhibiting the enzymatic activity, affecting the organism's virulence, and hampering microbial dissemination in the host.

In both ways, activation or inhibition, there are still open questions about their mechanism. In this regard, some boron-based compounds pose as intriguing ClpP modulators. Commonly classified as canonical proteasome inhibitor, the peptidomimetic boronate known as bortezomib is linked to a paradoxical allosteric activation of a bacterial ClpP, leading to an increase of proteolysis in a linear way.While some biophysical and biochemical approaches have given insights into structural and functional aspects of the ClpP-bortezomib complex, a detailed explanation at the atomic level about how the ligand modulates the enzymatic activity is still lacking. Considering this gap, in this work, another peptidomimetic boronate, ixazomib, was selected to study its effect on the ClpP from *Staphylococcus epidermidis*. In the first two parts, the crystal structure of native *Se*ClpP and *Se*ClpP-ligand complex obtained at PETRA III/DESY and EMBL (Hamburg, Germany) are explored and compared, aiming the discovery of structural differences with the assistance of low-resolution techniques like Batch-SAXS and SEC-SAXS available at EMBL (Hamburg, Germany). This comparative investigation revealed the reorientation of a key amino acid residue related to the extension of the protein's axial pores, a process that allows the degradation of globular proteins inside the ClpP's catalytic chamber.

In the latter part, assays with *Se*ClpP and ixazomib, under distinct conditions, confirmed the degradation of β-casein from bovine milk. Peptidolytic assays in the presence of peptidomimetic boronates were taken into consideration as well, indicating a change of modulation dependent on the ligand concentration.

Additionally, SEC-SAXS measurements demonstrated that ixazomib induces the assembly of the tetradecameric *Se*ClpP from its heptamers. For the first time, experiments confirm that a ligand bound to the catalytic sites plays a role in the protein's oligomerization.

Undoubtedly, the contributions displayed in this thesis are of great relevance for the understanding of modulation and conformational shifts of ClpP. The results show that the ligand used can be a scaffold for the development of novel antibiotics against nosocomial infections caused by opportunistic pathogens.

Zusammenfassung

Die geringe Verfügbarkeit neuer Antibiotika und die Ausbreitung multiresistenter Organismen stellen weltweit ein ernstes Problem dar. Jedes Jahr erleiden viele Menschen dadurch schwere Behinderungen oder sterben an Infektionen, die mit herkömmlichen antimikrobiellen chemotherapeutischen Mitteln nicht behandelt werden können. Diese Realität setzt auch Regierungen unter wirtschaftlichen Druck, da Strategien zur Bewältigung dieser Belastung im öffentlichen Gesundheitssystem hohe Investitionen erfordern.

Die bessere Bewältigung dieses Szenarios umfasst vorbeugende Maßnahmen zur Förderung eines vernünftigen Einsatzes von Antibiotika im Alltag, von Krankenhäusern bis hin zur Landwirtschaft. Zahlen einiger internationaler Organisationen zeigen, dass die in den letzten Jahren ergriffenen Maßnahmen und Strategien wirksam waren und die stetig zunehmende Ausbreitung neuer resistenter Stämme konnte, insbesondere in den Industrieländern, eingedämmt werden. Eine vergleichbare erfolgreiche Entwicklung vollzieht sich aktuell leider nicht in den Entwicklungs- und Schwellenländern, wo sich die Situation teilweise dramatisch verschlechtert.

Gleichzeitig sind Pläne für die Entwicklung neuer Medikamente notwendig. Denn in den letzten Jahrzehnten sind durchgängig mehr wirksame Antibiotika aufgrund der Ausbildung von Resistenzen nur noch eingeschränkt einsetzbar (z.B. Vancomycin) als neue wirksame Antibiotika auf den Markt kommen.

Einige Staphylokokken gehören zu den resistenten Organismen. *Staphylococcus aureus* (*Sa*) und *Staphylococcus epidermidis* (*Se*), kommensale Organismen, die auf der Haut und den Schleimhäuten vorkommen, können bei immungeschwächten und langzeitkranken Patienten zu hartnäckigen nosokomialen Infektionen führen.

Konventionelle Antibiotika können eine gute Wirksamkeit gegen metabolisch aktive Zellen im Blutkreislauf besitzen, wohingegen die Effektivität eingeschränkt ist, falls die Staphylokokken schützende Biofilme bilden. Studien mit der Untereinheit der kaseinolytischen Protease P (ClpP) haben ergeben, dass dieses Enzym ein vielversprechendes Makromolekül für die Eliminierung multiresistenter und dormanter Staphylokokken ist.

ClpP ist eine Endopeptidase, die zusammen mit Chaperonen aus der Superfamilie AAA+ (ATPasen, die mit verschiedenen zellulären Aktivitäten verbunden sind) einen proteolytischen Komplex bildet. Diese Maschine spielt eine wichtige Rolle bei der bakteriellen Proteinhomöostase, indem sie eine kontrollierte Proteolyse im Zytosol aufrechterhält. Diese Kontrolle wird von den Chaperonen durchgeführt, da sie die katalytische Kammer von ClpP für ausgewählte Substrate – entfaltete, fehlgefaltete und regulatorische Proteine – zugänglich machen, um sie abzubauen. In den letzten Jahren wurde jedoch entdeckt, dass natürliche und synthetische Moleküle die ATPasen nachahmen, die Funktion von ClpP stören und eine umfassende und wahllose Proteolyse im intrazellulären Medium auslösen, die zum Tod der Bakterien durch Selbstverdauung führt. Im Gegensatz dazu binden sich andere Verbindungen an die katalytischen Stellen von ClpP, hemmen die enzymatische Aktivität, beeinflussen die Virulenz des Organismus und behindern die mikrobielle Ausbreitung im Wirt.

In beiden Fällen, Aktivierung oder Inhibition, gibt es noch offene Fragen zu ihrem Mechanismus. In dieser Hinsicht stellen einige Borverbindungen interessante ClpP-Modulatoren dar. Das als kanonischer Proteasom-Inhibitor klassifizierte peptidomimetische Boronat, Bortezomib, ist mit einer paradoxen allosterischen Aktivierung eines bakteriellen ClpP verbunden, die zu einer linearen Zunahme der Proteolyse führt. Einige biophysikalische und biochemische Ansätze haben Einblicke in die strukturellen und funktionellen Aspekte des ClpP-Bortezomib-Komplexes gegeben, aber die Erklärung auf atomarer Ebene, wie der Ligand die enzymatische Aktivität moduliert, fehlt noch. Angesichts dieser Lücke wurde in dieser Arbeit vorgeschlagen, ein weiteres peptidomimetisches Boronate, Ixazomib, auszuwählen, um seine Wirkung auf ClpP aus *Staphylococcus epidermidis* zu untersuchen. In den ersten beiden Teilen werden die Kristallstrukturen von nativen *Se*ClpP- und *Se*ClpP-Ligand-Komplex, die an PETRA III/DESY und EMBL (Hamburg, Deutschland) erhalten wurden, untersucht und verglichen, um mithilfe von niedrigauflösenden Techniken wie Batch-SAXS und SEC-SAXS, die am EMBL (Hamburg, Deutschland) verfügbar sind, strukturelle Unterschiede zu entdecken. Diese vergleichende Untersuchung ergab, dass sich wichtige Aminosäurereste im Zusammenhang mit der Erweiterung der axialen Poren des Proteins neu ausrichten, ein Prozess, der den

Abbau von globulären Proteinen in der katalytischen Kammer von ClpP ermöglicht.

Im letzten Teil bestätigten Tests mit SeClpP und Ixazomib den Abbau von β-Kasein aus Kuhmilch. Auch peptidolytische Tests in Gegenwart von peptidomimetischen Boronaten wurden berücksichtigt, die auf eine Änderung der Modulation in Abhängigkeit von der Ligandenkonzentration hindeuten.

Darüber hinaus zeigten SEC-SAXS-Messungen, dass Ixazomib die Bildung des tetradekameren SeClpP aus seinen Heptameren induziert. Dies ist das erste Mal, dass Experimente bestätigen, dass ein an die katalytischen Stellen gebundener Ligand eine wichtige Rolle bei der Oligomerisierung des Proteins spielt.

Zweifellos sind die in dieser Arbeit dargelegten Beiträge von großer Bedeutung für das Verständnis der Modulation und Konformationsänderungen von ClpP. Die Ergebnisse zeigen, dass der verwandte Ligand als Gerüst für die Entwicklung neuartiger Antibiotika gegen nosokomiale Infektionen durch opportunistische Krankheitserreger dienen können.

1. Introduction

1.1.   Antibiotics as a global threat: development and resistance

Evolutions of knowledge, technology, medicine, and social behavior have provided an unprecedented quality of life for billions of people around the globe. Among those improvements, the discovery and administration of antibiotics can be highlighted as one of the reasons for the increase in life expectancy from the beginning of the twentieth century. In this context, Alexander Fleming noted, in 1920s, that the mold of *Penicillium notatum* suppressed *Staphylococci* colonies' growth in Petri dishes. The mold expresses a compound named penicillin, a substance readily diffusible in agar, which causes bacterial death by hampering peptidoglycan synthesis for cell wall building (Ghooi and Thatte 1995). The antimicrobial effect of penicillin permitted the treatment of infections that led to uncountable human losses in previous centuries.

Under the influence of the Second World War (1939 – 1945) and the advances of microbial fermentation, the scenario for mass production of penicillin in vat fermenters became essential for treating soldiers in wartime (Landecker 2016). In addition, during the following years, research led to the discovery and isolation of new antibiotics triggered by a technique known as soil bioprospecting. This technique took advantage of the cooperative work of experts in soil science, resulting, for example, in the production of aureomycin, a drug used to treat typhoid fever (Landecker 2016). This compound, also known as chloramphenicol, blocks protein biosynthesis by binding to the peptidyl transferase center of the 50S subunit of microbial ribosomes.

Besides penicillin and aureomycin, many other antimicrobial drugs were identified subsequently: sulfonamides, nitrofurans, cephalosporins, and macrolides, to name a few. The "golden years" or the "golden era" (1940 – 1970) represented a prolific period of antibiotic discovery and development (Lyddiard et al. 2016). Those advances transformed the practice of medicine, reducing mortality rates from bacterial infections and enabling the successful treatment of life-threatening diseases (Maxson and Mitchell 2016).

Figure 1 shows more compounds incorporated into antimicrobial chemotherapies in previous decades.
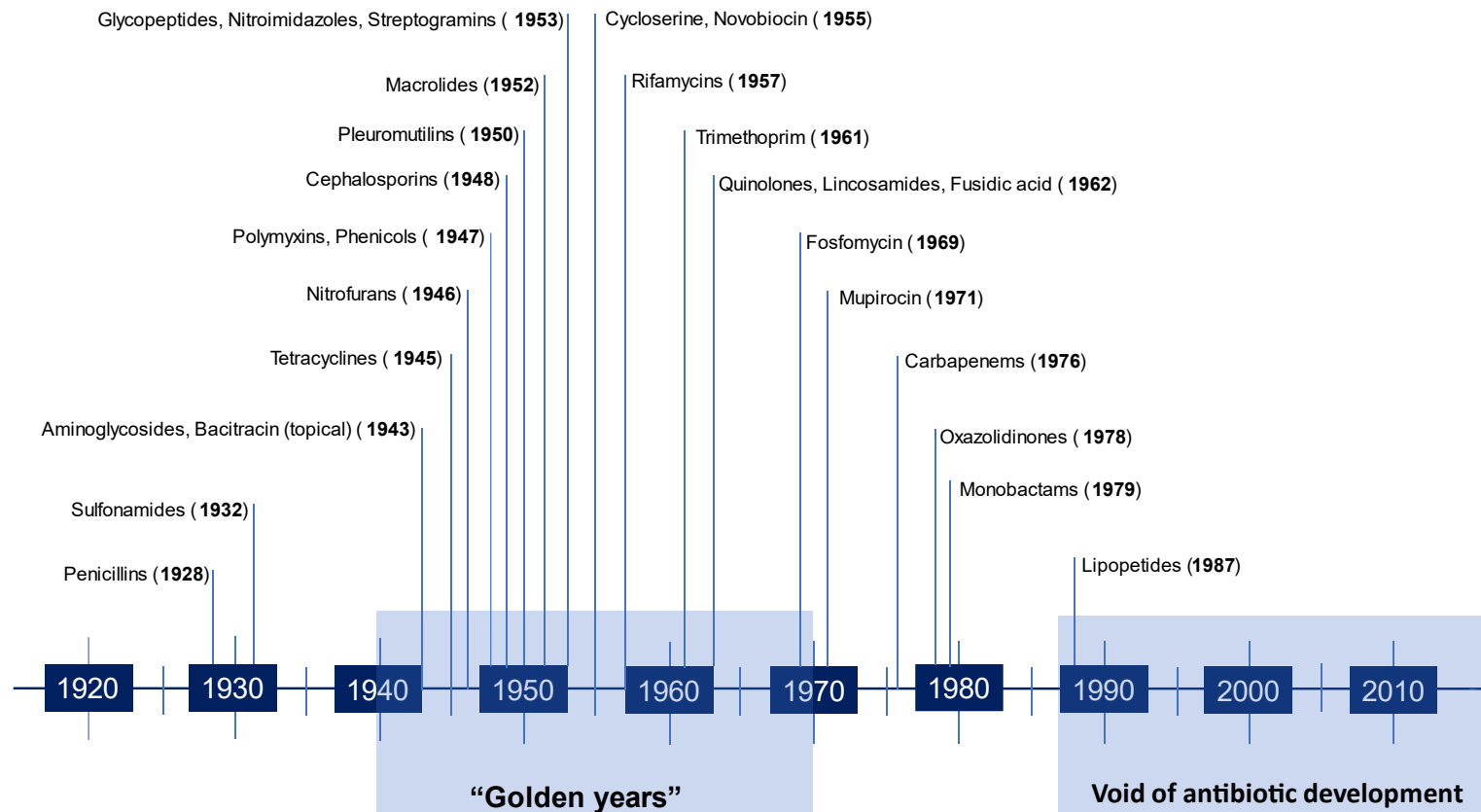
Figure 1 – Antibiotics over the years (1920 – 2010). After the isolation of penicillin, the idea summarized by the sentence "If it can happen once, surely it can happen again" moved other scientists towards the search for novel drugs (Raper, 1952). The "Golden Years," comprised between 1940 and 1970, refer to a period when different antimicrobial agents with broad spectrum were obtained (Khardori et al. 2020). Since 1990, the drastic reduction of novel antibiotics has resulted in the lack of development of a "post-antibiotic" era (Kwon and Powderly 2021). Adapted from ReAct, 2024.

The diverse options of antibiotics also represent different mechanisms of action: as cited before, some compounds act in the synthesis of cell walls or the biosynthesis of proteins. Other drugs, on the other hand, inhibit DNA replication (fluoroquinolones) and folic acid metabolism (sulfonamides), for example (Halawa et al. 2023). Table 1 enlists further examples and descriptions of their mechanisms of action.

Table 1 – Antibiotics: main mechanisms of action and examples.

Mechanism of Action	Description	Examples
Inhibition of Cell Wall Synthesis[1]	Prevents bacteria from forming cell walls, leading to cell lysis and death.	Penicillins , Cephalosporins, Carbapenems, Vancomycin, Bacitracin
Inhibition of Protein Synthesis[2]	Blocks the function of ribosomes, hindering the production of essential proteins.	Tetracyclines, Aminoglycosides, Macrolides, Chloramphenicol, Clindamycin
Inhibition of Nucleic Acid Synthesis[3]	Interferes with the synthesis of DNA or RNA, preventing bacterial replication.	Quinolones, Rifamycins
Disruption of Cell Membrane Function[4]	Causes damage to the bacterial cell membrane, leading to leakage of cell contents and death.	Polymyxins, Daptomycin
Inhibition of Metabolic Pathways[5]	Blocks key metabolic pathways that are crucial for bacterial survival and growth.	Sulfonamides, Trimethoprim

[1] (Livermore 1995),[2] (Wilson 2014),[3] (Hooper 2000), [4] (Storm et al. 1977), and [5] (Bushby and Hitchings 1968).

While this plethora of biochemical strategies is essential for human and animal health, as well as for agriculture, the wide use and misuse of those drugs increase a severe issue: antibiotic resistance (Levy and Marshall 2004) (Figure 2), especially by selective pressure, a process that favors the prevalence of resistant bacteria over susceptible ones (Pouladfar et al. 2015; Witte 2000).
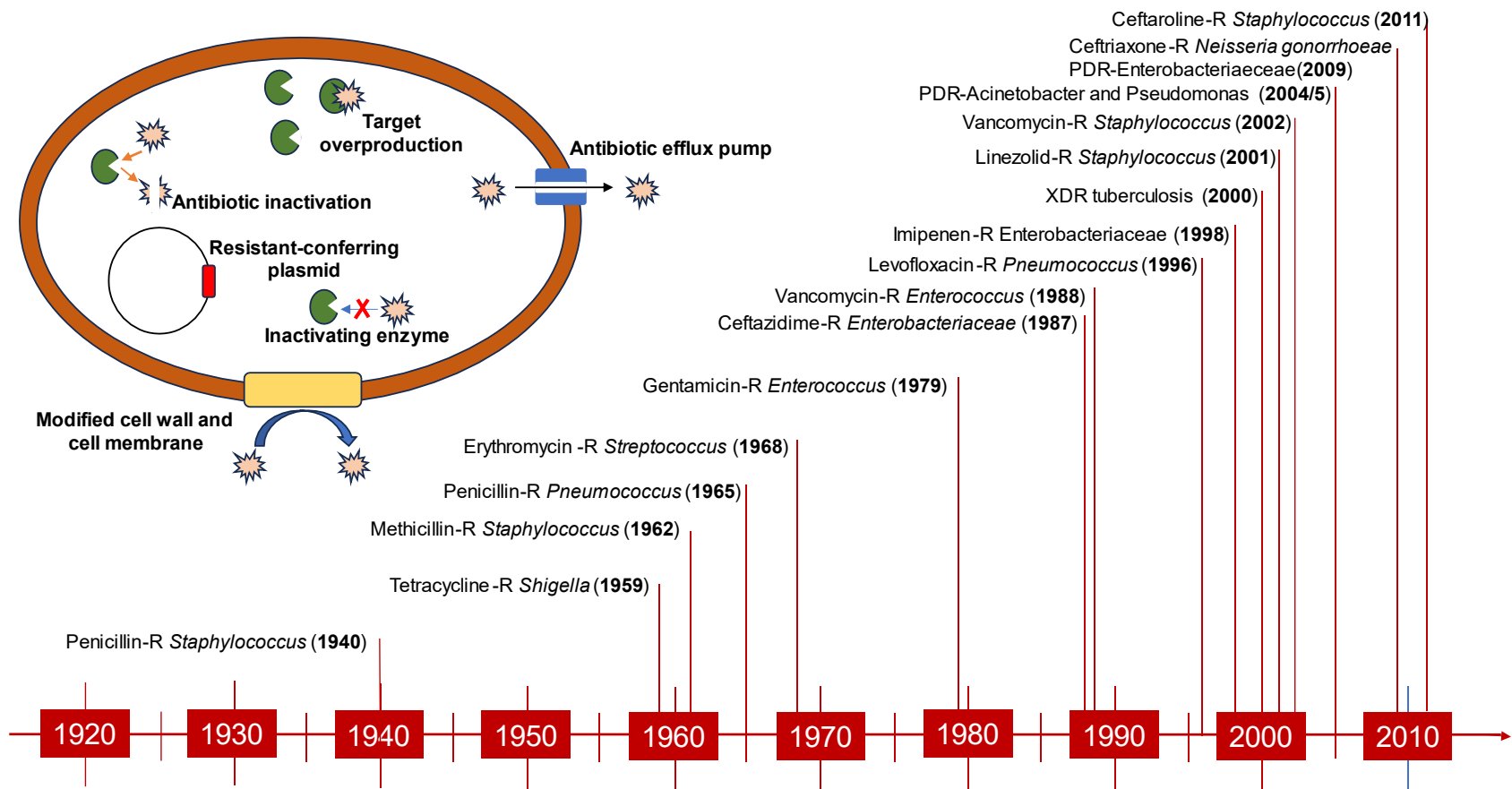
Figure 2—Main mechanisms of antibiotic resistance and discovery of resistant bacterial strains over the years. The timeline was adapted from the Center for Disease Control and Prevention, 2024.

Resistance comes from the ability of the microbe to withstand the antimicrobial effect through genetic mutations, enzymatic degradation, efflux pumps, alteration of bacterial cell permeability, and acquisition of resistance genes (Li et al. 2024; Nasrollahian et al. 2024; Kolár et al. 2001). The time-resolved spread of antibiotic-resistant bacteria leads to treatment failures, prolonged illnesses, increased healthcare costs, and higher mortality rates (Nwobodo et al. 2022).

The communication of antibiotic resistance happens in many ways, such as direct contact and environmental contamination. The horizontal transmission through strains, like the accumulation of mutations, leads to the emergence of "superbugs," and the risk management of this scenario requires effective strategies.

A clear understanding of each country's reality helps to implement infection hindrances by reducing drug overuse in agriculture, food processing, food safety, and medical fields (D'Agata et al. 2007; Silbergeld et al. 2008; Wu-Wu et al. 2023). Some projections consider that the consumption of antimicrobials will be 200% higher in 2030 than in 2015 (Sutherland 2018), if the current status remains unaltered. For instance, the number of daily doses consumed in high-income, upper-middle-income, lower-middle-income, and lower-income communities in the last years is alarming. Figure 3 shows a comparative analysis using data from 2000 and 2015.
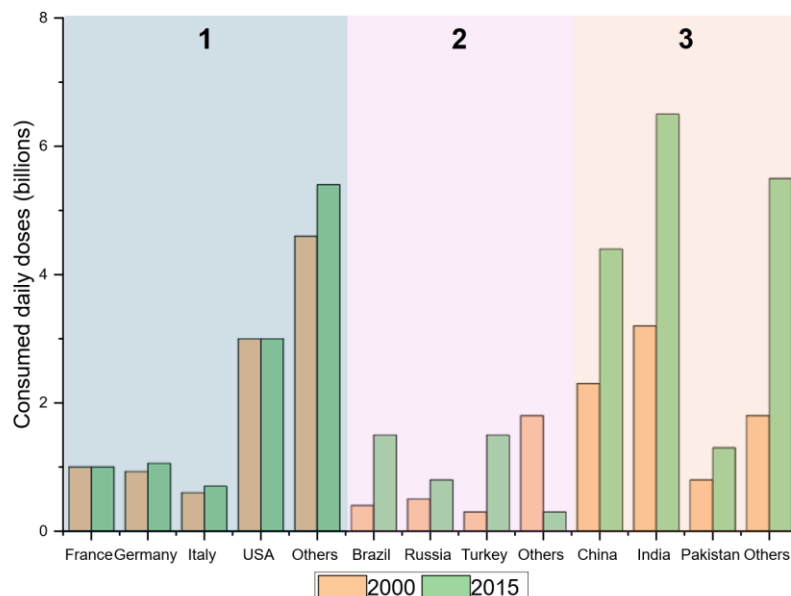
Figure 3 – Trends in antibiotic consumption in some developed countries (blue section, 1), developing regions (purple section, 2), and third world (orange section, 3). The graph is adapted from Chin et al. 2023 and Larsen et al. 2022.

A second aspect is the combined action of the public and private sectors (Edwards et al. 2018). Cooperative actions could provide the necessary infrastructure to facilitate access to clean water and improved sanitation facilities (Guo et al. 2020), assuring prophylactic means against infections and reducing antimicrobial chemotherapies.

Apart from the preventive means, the emergence of antibiotic resistance also demands the development of new biochemical strategies to deal with "superbug" infections. Antibiotic-resistant organisms are found in different areas, from farms to public markets, causing severe problems, particularly negative impacts on human health. Studies on this ever-growing issue estimate that approximately 10 million lives will be lost by 2050 (Walsh et al. 2023). Besides that, thousands of serious disabilities are expected from this scenario, according to data reported by the European Antimicrobial Resistance Surveillance System (EARS-Net) in 2015 (Antoñanzas and Goossens 2019).

In the European area, the main antimicrobial multi-resistant (AMR) agents are the gram-negative bacteria *Escherichia coli* (*E.coli*), *Klebsiella pneumoniae* (*K.pneumoniae*), *Pseudomonas aeruginosa* (*P. aeruginosa*), and *Acinetobacter baumannii* (*A. baumannii*), as well as gram-positive bacteria *Enterococcus faecalis* (*E.faecalis*), *Streptococcus pneumoniae* (*S.pneumoniae*), and *Staphylococci* (Vivas et al. 2019). In Table 2, there are further details about the isolates of those microorganisms in the European Union (EU) / European Economic Area (EEA).

Table 2 – Total number of invasive isolates tested and AMR percentage (%): EU/EEA, 2020/2021 (European Centre for Disease Prevention and Control, 2023).

AMR profile [1]	Number of isolates (2020)	Percentage of total (%) (2020)	Number of isolates (2021)	Percentage of total (%) (2021)
Total of isolates	219 765	100.0	241 063	100
Fully susceptible	124 201	56.5	139 345	57.8
Any single resistance	45 967	20.9	47 771	19.8
Any resistance to two antimicrobial groups [2]	24 188	11.0	25 351	10.5
Resistance to three antimicrobial groups [2]	18 427	8.4	21 134	8.8

[1]In this table, the presented values are the sum of the isolates of the following bacteria: *E. coli*, *P. aeruginosa*, *Acinetobacter sp.*, *E. faecalis*, *S. pneumoniae*, and *Staphylococcus aureus* (*S. aureus*).

[2]The combination of antibiotics (two or three combinations) may differ for each organism.

The numbers still present an alarming situation, especially when the availability of new antibiotics on the market is scarce. The prohibitive costs of research and development negatively affect the profitability of pharmaceutical companies. Even with subsidies from governments, the cost-effectiveness is still low. This reality makes the industry invest more resources in "lucrative noncommunicable medication," such as the ones related to cancer and lifestyle. Therefore, some European countries, such as France, Germany, and Sweden, establish differential price references, annual revenues, market entry rewards, transferable exclusivity extensions, and milestone payments for some groups of antimicrobials (Anderson et al. 2023). In the intercontinental context, offices associated with the United Nations (UN) develop strategies against antibiotic resistance with global action plans, taskforces, budgets, and the release of periodic reports (Hoffman et al. 2015; Mendelson et al. 2024).

1.2. *Staphylococcus epidermidis*: an opportunistic pathogen

In the group of organisms that participate in the crisis above, *Staphylococci* are some of interest. These organisms were first discovered by Alexander Ogston, while he was analyzing the causes of wound infections (Baird-Parker 1990). These investigations allowed the isolation of spherical bacteria from surgical abscesses, and these cells tended to form grape-like clusters. This feature justifies the term "*Staphylococcus*", from the Greek words "staphyle" (grape) and kokkos (berry) (Makinde et al. 2019).

Many *Staphylococci* species are naturally found in normal skin flora, and they are classified according to colony morphology, growth conditions (oxygen need, temperature, salt tolerance), catalase and coagulase production, pathogenicity, and antibiotic resistance.

Staphylococcus aureus (*S. aureus*) and *Staphyococcus epidermidis* (*S. epidermidis*) are of great clinical relevance. Unquestionably, multi-resistant *S. aureus* (MRSA) strains are the main players in a plethora of animal conditions: infections of the skin and soft tissues, respiratory tract, bone and joints, bloodstream, gastrointestinal system, etc. (Garcia et al. 2019). These diseases represent high hospital costs and national economic impacts: per patient, the amount can reach approx. $27,000 (Clancy et al. 2006; Nissenson et al. 2005; Rao

et al. 2008), and in the United States alone, treating *S.aureus* infections leads to public expenses of roughly $2.2 billion (Cobb et al. 2019).

Staphylococcus epidermidis is a probiotic bacterium that keeps a balance in microbiota, controls the skin's pH, and degrades sebum (McLoughlin et al. 2022). That organism also protects the body against conditions like acne and atopic dermatitis (Fournière et al. 2020; Nakatsuji and Gallo 2018).

Although *S. epidermidis* is advantageous for life in many ways, some strains have clinical importance as they pose deleterious health effects, particularly in immunocompromised and long-term hospitalized patients. In 2009, the estimated annual cost of *S. epidermidis* infections was $2 billion in the United States (Otto 2009).

Considering both species, the common mechanism for infecting the host organism involves the expression of enzymes for tissue invasion, and the secretion of toxins helps the pathogen to evade the immune system and disseminate (Cohen 1986; Eiff et al. 2002). The bacterial spread always represents a life-threatening risk, increasing the possibility of bacteremia and sepsis (Di Franco et al. 2021; Minasyan 2019).

The trends and prevalence of antibiotic resistance in *Staphylococci* are alarming, and examples are found in Table 3. During the last decades, drugs that target nucleic acid biosynthesis, β-lactams, glycopeptides, inhibitors of protein synthesis at the 30S and 50S subunits, and the folic acid metabolism have been losing efficacy in combatting diseases caused by multi-resistant strains (Baran et al. 2023; Foster 2017). Derivatives that still work against MRSA, such as vancomycin and linezolid, require precautious administration so as not to become ineffective soon. Considering vancomycin as an example, a "golden" drug for serious infections, some resistant strains were already detected, but they still have not spread and have not become predominant in hospital environments (Périchon and Courvalin 2009; Appelbaum 2006; Hiramatsu 2001).

Table 3 – Examples of ineffective antimicrobials against multi-resistant *Staphylococci* and the cause of resistance.

Antibiotic	Cause of resistance	Examples
Penicillins[1]	Beta-lactamase production	Methicillin, Oxacillin, Nafcillin
Cephalosporins[2]	Altered penicillin-binding proteins (PBPs)	Cefazolin, Cefuroxime, Ceftriaxone
Macrolides[3]	Efflux pumps, methylation of ribosomal RNA	Erythromycin, Azithromycin
Aminoglycosides[4]	Modifying enzymes, target modification	Gentamicin, Tobramycin, Amikacin
Tetracyclines[5]	Efflux pumps, ribosomal protection proteins	Tetracyclin, Doxycycline
Quinolones[6]	Mutations in DNA gyrase/topoisomerase IV	Ciprofloxacin, Levofloxacin
Glycopeptides[7]	Thickened cell wall, altered target sites	Vancomycin, Teicoplanin

[1](Chambers 2001), [2](Chambers 1997), [3](Leclercq 2002), [4](Shaw et al. 1993), [5](Roberts 1996), [6](McDonald and Blondeau 2010), and [7](Witte 2004).

A further form of protection for the *Staphylococcus* species is biofilm synthesis. This structure can form on almost any surface where moisture and nutrients are available, including natural spaces, industrial systems, and medical devices, being responsible for 80% of all chronic bacterial infections (Rather et al. 2021; Veerachamy et al. 2014). Representing a highly adaptive and resilient mode of microbial life (Yin et al. 2019), the biofilm synthesis process is divided into the following stages of development: initial attachment, microcolony formation, maturation, and dispersal (Kaplan 2010), as demonstrated in Figure 4.

During the initial step, attachment (1), planktonic cells are held together through weak interactions, mainly van der Waals forces and electrostatic interactions (O'Toole and Kolter 1998). The microcolony formation (2) happens once the production of the extracellular polymeric substance (EPS) matrix has started with consequent bacterial aggregation and the establishment of cellular communication via quorum sensing, a mechanism that is instituted by a system of signaling molecules, detection, and response (Parsek and Singh 2003). The maturation (3) is the formation of a tridimensional complex as more layers of bacterial cells and EPS accumulate (Donlan 2002). Finally, the dispersal (4) is the return of the dormant cells to a free-floating state (Kaplan 2010).
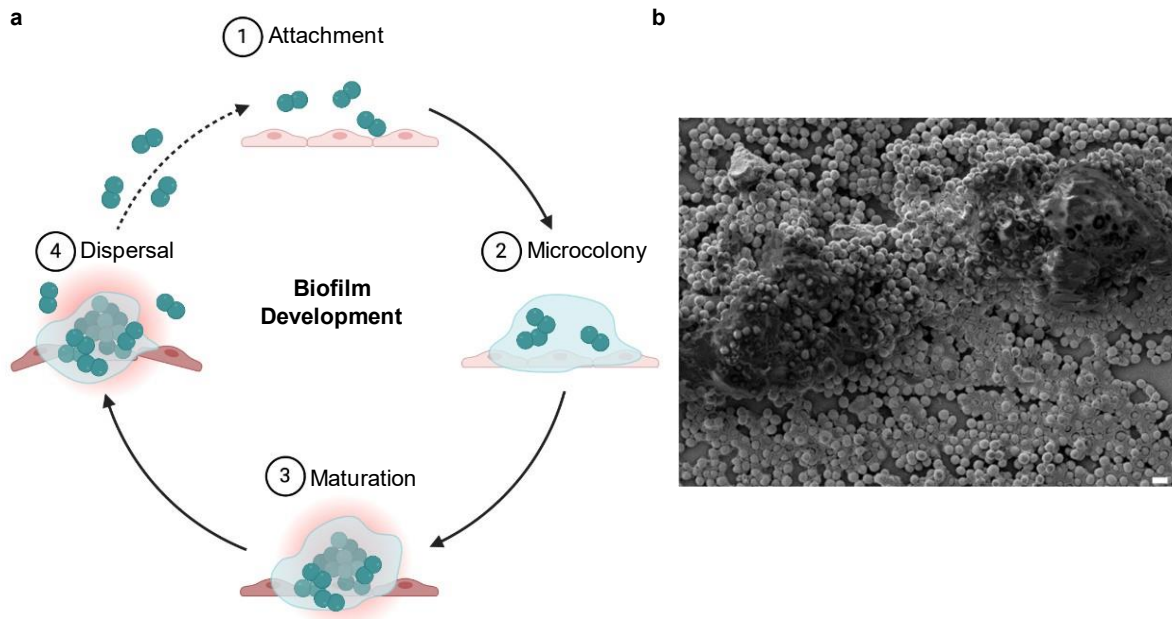
Figure 4 – Biofilm as a protection mechanism of bacteria. In this structure, dormant cells are "shielded" from antibiotics that aim for metabolically active planktonic ones. (**a**) Stages of biofilm evolution: attachment, microcolony, maturation, and dispersal. Created with BioRender.com. (**b**) Microscopic image of a *S.aureus* biofilm *in vitro* (Lamret et al. 2020).

Biofilm infection issues are more critical for individuals who use medical devices like catheters, orthopedic implants, cardiac/intravascular devices, and surgical implants (Di Domenico et al. 2022). Due to its persistence, biofilm can cause chronic infections in many cases. Many antibiotics of common use can only eliminate planktonic microbes, not reaching the shielded and less susceptible dormant cells (Høiby et al. 2010). These cells grow more slowly and exhibit altered metabolic activity, making them less vulnerable to drugs that affect the cellular division (Stewart et al. 2019).

1.3. Caseinolytic protease P subunit (ClpP): a promising drug-target protein

1.3.1. Bacterial ClpP and its role in natural processes

The computer-aided and rational drug design is commonly focused on the synthesis of novel derivatives from old compounds (Figure 5). It results in the absence of new antimicrobials with high efficiency and low toxicity (Coates et al. 2011). In this context, the discovery of other mechanisms of action is still lacking. This situation urges investments in more targeted drug discovery programs to

develop new treatments against microbial infections, like the studies on caseinolytic protease P subunit (ClpP).
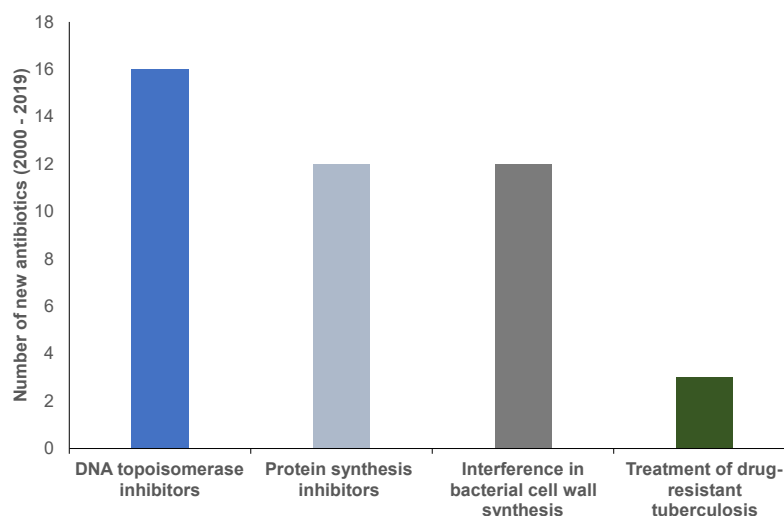
Figure 5 – Approved antibiotics according to the mechanism of action between 2000-2019. Data obtained from Shi et al. 2023.

ClpP, a serine endopeptidase (EC 3.4.21.92) that constitutes a proteasome with ATPases, chaperones from the AAA+ superfamily (Queraltó et al. 2023), participates in protein homeostasis. This natural process is associated with the degradation of misfolded, unfolded, and regulatory proteins (Stahlhut et al. 2017; Thomsen et al. 2002; Frees and Ingmer 1999), conferring bacteria conditions to withstand heat/oxidative shock (Xie et al. 2013) and virulence factors to escape the host's immune system (Gaillot et al. 2000; Frees et al. 2013).

The homeostasis promoted by ClpP is directly linked to the regulation of virulence at the transcriptional level. For example, when ClpP is inhibited, the process of biofilm formation is depleted, and the cell vulnerability to the host's immune system increases, reducing the chances of the organism's survival (Feng et al. 2021).

If the protein's activity is dysregulated, then a promiscuous proteolysis initiates and the cells are submitted to self-digestion, a process that leads to a bactericidal effect (Shen et al. 2017). Then, to avoid an uncontrolled proteolytic activity in the intracellular environment, there is a natural controlling strategy to modulate ClpP function: it needs an ATPase that selects the substrate to be degraded and promotes conformational changes on ClpP, in order to activate it (Aljghami et al. 2022).

The chaperones involved with ClpP are found in the Clp/Hsp100 family. ClpP and ATPases act in synergy, building a complete proteolytic system, to ensure the maintenance of cellular proteostasis. Nonetheless, each organism has a specific set of chaperones that identify and select certain types of substrates to be unfolded and degraded. It is important to consider that those chaperones are also associated with adaptors responsible for regulating them before and after homeostasis (Zeth et al. 2002; Kirstein et al. 2009; Martin et al. 2008; Kirstein et al. 2006).

Bacterial members of Clp/Hsp100 family include ClpA, ClpB, ClpC, and ClpX (Maurizi and Di Xia 2004). ClpA and ClpX initiate the depletion of misfolded or damaged proteins, preventing their accumulation and potential toxicity (Olivares et al. 2018). Additionally, ClpA still interacts with diversified substrates, thereby expanding the range of subjects to proteolysis (Hoskins et al. 2000).

ClpB disaggregates proteins submitted to heat and oxidative stress (Mishra and Grover 2016; Katikaridis et al. 2021; Sangpuii et al. 2018). Furthermore, ClpC found in gram-positive bacteria partners with ClpP to degrade regulatory biomacromolecules of diverse biochemical mechanisms, including the control of development and virulence (Queraltó et al. 2023).

The functional versatility of the ATPases is underscored by their structural attributes: an N-terminal domain for substrate recognition, a central ATPase domain for ATP binding and hydrolysis, and in some cases, a C-terminal domain which is a mediator in interactions with other proteins (Sauer and Baker 2011). The energy derived from ATP hydrolysis is harnessed to induce conformational changes in substrate proteins, facilitating their unfolding, disaggregation, and translocation into the proteolytic chamber in ClpP (Fei et al. 2020).

In Figure 6, a cryo-EM structure of the ClpP-ATPase complex is displayed. ClpP, a barrel-shaped peptidase, comprises two-stacked heptameric rings and a central chamber that sequesters 14 catalytic sites (Liu et al. 2014; Alexopoulos et al. 2012). This chamber is protected by two axial pores controlled by ATPAses. Once bound to ClpP, these chaperones control the orientation of the N-terminal loops that constitute the gating mechanism (Lee et al. 2010b), in a way that the pores get open for the substrate's access (Xu et al. 2024).
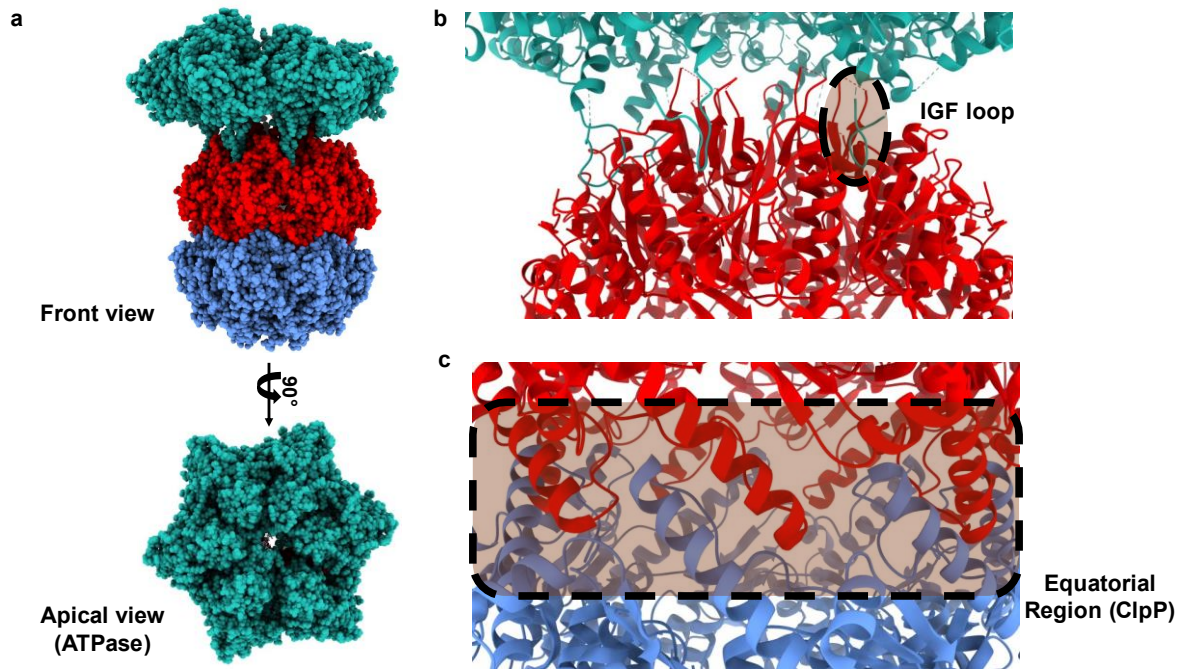
Figure 6 – cryo-EM structure of a ClpP-ATPase complex (Ripstein et al. 2020a). (**a**) Front and apical views of the complex. (**b**) Both proteins are connected: IGF loops from the ATPase bind to ClpP's allosteric sites known as "hydrophobic pockets". (**c**) Equatorial area where ClpP rings are connected.

The symmetry mismatch allows the hexameric ATPases to be connected to the ClpP's heptameric rings in a tilted manner. It is the consequence of an evolutionary process that improves the efficiency of the substrate's unfolding and translocation (Joshi et al. 2004).

1.3.2. General structural and functional aspects of ClpP

As a chymotrypsin-like peptidase, the main elements in ClpP's activity include 14 catalytic triads composed of serine (Ser), histidine (His), and aspartic acid (Asp), acting in synergism to cleave peptide bonds (Figure 7).
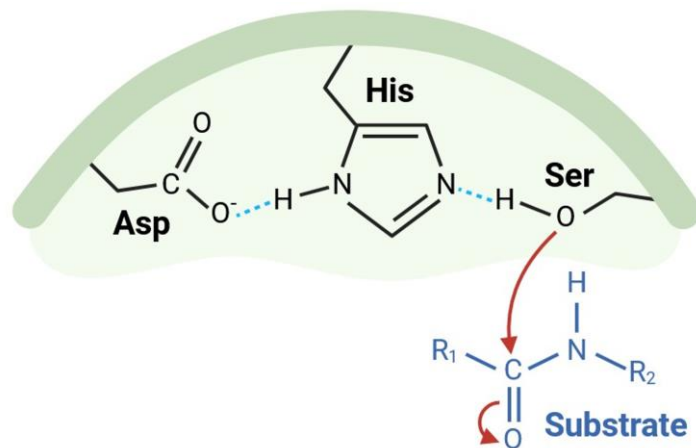
Figure 7 – Catalytic triad in serine proteases. Created with BioRender.com.

Figure 8 divides the entire mechanism into two main steps: acylation and deacylation. In acylation, Ser binds to the substrate, generating a tetrahedral intermediate and a subsequent covalent acyl-enzyme with the release of the first product fragment. In deacylation, the following process occurs: the development of a second tetrahedral intermediate, hydrolysis of the acyl-enzyme, and the breakdown of the second product fragment (Alves França et al. 2024).

The interaction with the histidine residue makes the serine's side chain, in its alcoholic form, become a stronger nucleophile (alkoxide conjugate), disposing of a higher electron density around the oxygen atom. Moreover, Asp keeps His in its proper orientation through electrostatic interaction. Another point is that, initially, there is a sp^2

hybridization in the substrate's alkyl group, which makes its structure planar. After the nucleophilic attack, the tetrahedral intermediate no longer displays planarity and has

a negative charge in oxygen. At this moment, this intermediate is stabilized by an oxyanion pocket (Ménard and Storer 1992).
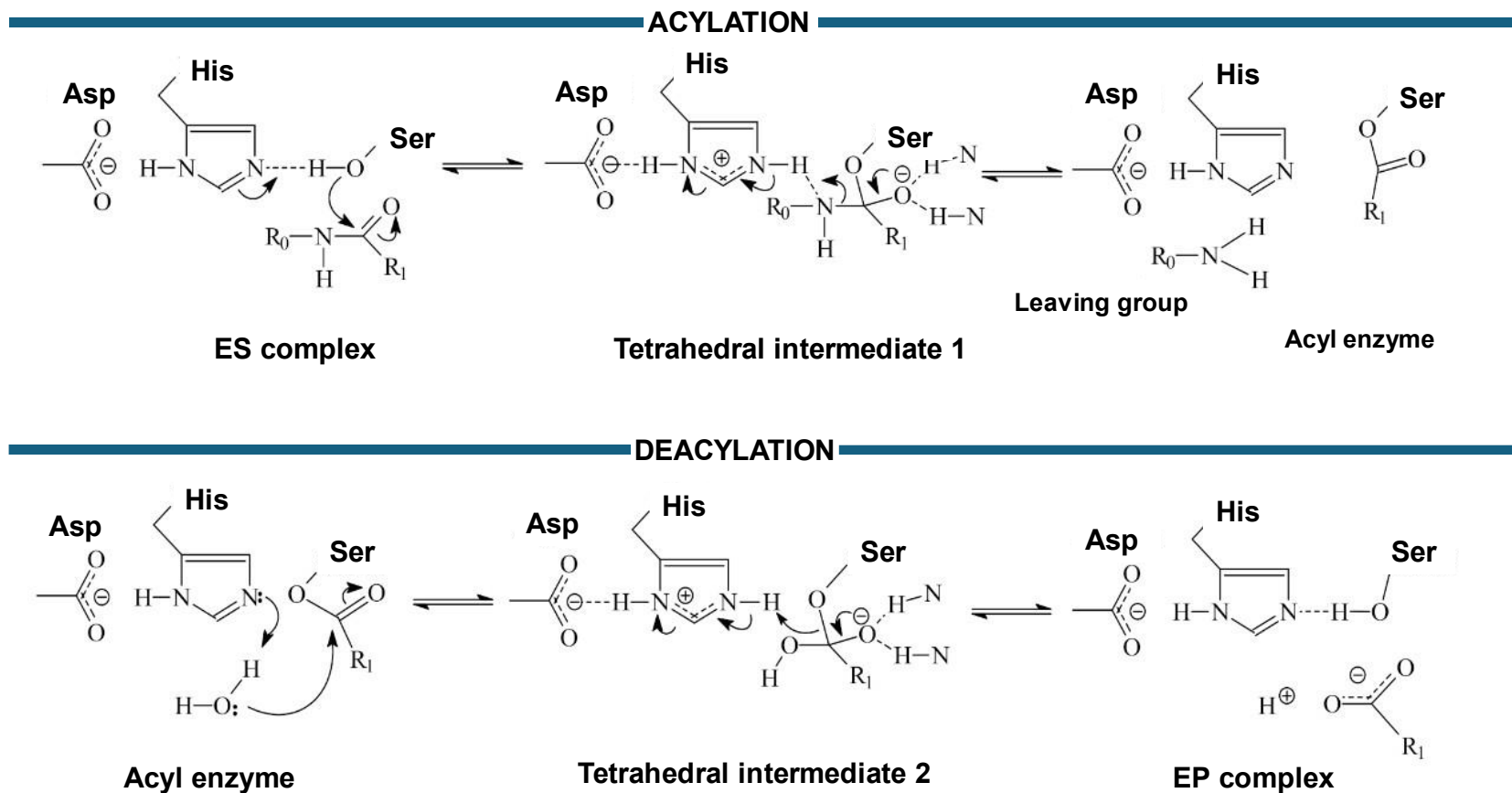
Figure 8 – ClpP's mechanism of action and its main steps: acylation and deacylation. The process is triggered by serine's alkoxide conjugate, evolving from tetrahedral intermediates to the release of product fragments. The stabilization of the intermediates is promoted by the oxyanion pocket or hole. Adapted from Kovach 2021.

The handle regions of ClpP, in the equatorial area, correspond to a β-strand and a long α-helix (αE-helix) that keep both heptameric rings connected by interdigitation (Lee et al. 2011; Mabanglo and Houry 2022; Yu and Houry 2007) (Figure 9). Those regions are flexible, and their extension or compactness directly influences the enzymatic function (Alves França et al. 2024) by controlling the alignment of the Ser-His-Asp triads.

The ClpP structure with an extended handle region is the only active state because of the proper geometry of the catalytic triad (Figure 9a). When ClpP becomes more compact, the αE helix loses helical turns, the β-strands become disordered (Mabanglo et al. 2023), and consequently, the Ser and His of the catalytic triad are misaligned (Stahl and Sieber 2017) (Figure 9b). This misalignment hampers the process of acylation and deacylation depicted in Figure 8.
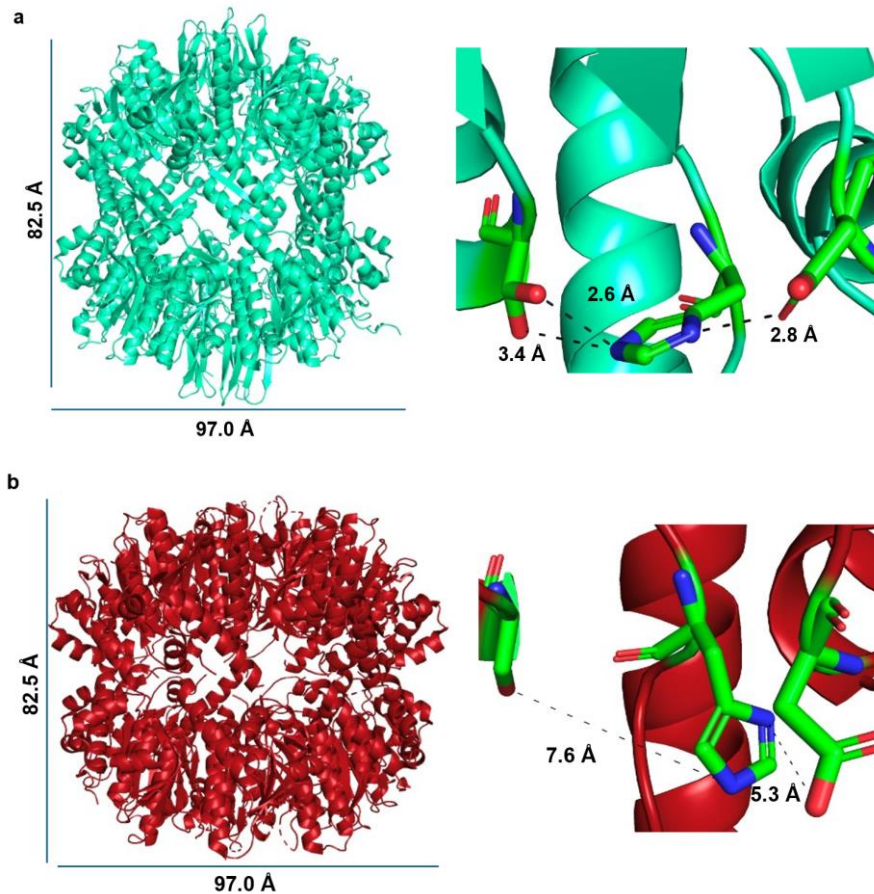
Figure 9 – (**a**) Extended ClpP and aligned catalytic triad (Malik et al. 2020). (**b**) Compact ClpP and misaligned catalytic triad (Ye et al. 2013).

1.3.3. Non-enzymatic activation and inhibition of ClpP

As stated previously, the inhibition and dysregulation of ClpP activity are significant mechanisms for investigations on drug targets. A way to replace a regulated function of ClpP by a dysregulated one is essential for medical purposes. Along these lines, non-enzymatic compounds that mimic the ClpP-ATPase interaction have been studied. The first ClpP activator, acyldepsipeptide (ADEP), an antibiotic naturally synthesized by *Streptomyces hawaiiensis* (Goodreid et al. 2014), was found to bind to the allosteric sites in ClpP, the same ones where the chaperones bind with their IGF loops (Martin et al. 2007; Joshi et al. 2004), and once ADEP is bound, its interaction cannot be revoked by ATPase anymore (Lee et al. 2010a). Then, when ClpP-ADEP is formed, promiscuous proteolysis initiates, many globular proteins are degraded, and a consequent bactericidal action occurs (Lavey et al. 2018). Table 4 shows potential substrates of the ClpP from *Escherichia coli* (*Ec*ClpP) and *Bacillus subtilis* (*Bc*ClpP).

Table 4 – Identified potential substrates of *Ec*ClpP and *Bs*ClpP. Substrates are listed based on their function, except those in "Unknown function". Adapted from (Bhandari et al. 2018).

Protein	Biochemical roles and substrates
*Ec*ClpP	**Metabolic processes** AceA, AcnB, AldA, AtpD, CysD, DadA, FabB, GapA, GatY, GatZ, GlcB, GlpD, GlyA, LldD, PaaA, TnaA, Udp **Stress response/ oxidation - reduction**: Dps, KatE, NrdH, Tpx **Transcription regulation** Crl, DksA, Fnr, IscR, LexA, RpoS, Rsd, RseA, YbaQ **Translation**: RplE, RplJ, RplK, RplN, RplS, RplU, TufB **Protein folding and proteolysis** ClpX, DnaK, GroEL, Lon, PepB **Transport**: CysA, ExbB, GatA, OmpA, SecA **Biosynthesis**: LipA, MoaA, PncB, RibB **Signal transduction**: CheW **Protein maturation**: IscA, IscU **Cell division**: FtsZ **Unknown function**: YebO, YcbW, YdaM, YgaT
*Bs*ClpP	**Metabolic processes** RapC, PdhC, Tkt, Cmk, PurA, PurH, PurS, YdbM, YoxD, RecA, YhfH, YdaE, ClpC, ClpE, GspA **Stress response/ oxidation - reduction**: NfrA, TrxA, TrxB, Yfmj, YqiG, YqjM, YwrO, YhdN, YqkF, YugJ, PhdD, CysH, KatE, MsrA, SodA, Tpx, YdbD, McsB **Transcription regulation** SigB, AbrB, GreA **Translation**: GatB **Protein folding and proteolysis** YmfH, YpwA, PpiB, YfkM, ClpX, YraA **Cell division**: MurAA **Biosynthesis**: PurL, PurM **Sporulation**: MecA **DNA repair/homologous recombination** RecA Unknown function: YflT, YuaE, GsiB, YceH, YvaA, YwfL

Subsequently, other compounds with the same mode of action were synthesized, providing more information about the activated enzyme's functional and structural features. Examples are ADEP derivatives (Li et al. 2017; Lee et al. 2010a), ureadepsipeptides (Griffith et al. 2019), and (S)-ZG197 (Wei et al. 2022).

Some mutations that protect ClpP against complete dysregulation have already been discovered (Malik et al. 2020). To avoid this issue, the combined administration of ClpP activators and other antibiotics tends to be adopted (Culp and Wright 2017).

Another way to modulate the ClpP function is to use inhibitors. Although this mechanism mainly produces a bacteriostatic effect, it impairs biochemical processes that downregulate or upregulate the expression of virulence factors (Aljghami et al. 2022). Thus, cell survival before environmental challenges is reduced (Moreno-Cinos et al. 2019).

The main advantage of using ClpP inhibitors is that bacteria are less prone to suffer selection pressure (Moreno-Cinos et al. 2019). In this case, a non-lethal mechanism is involved since it does not correspond to essential cellular processes (e.g., cell wall synthesis, protein synthesis, DNA replication). While some inhibitors only impede the substrates from being cleaved (Pahl et al. 2015), others disrupt the tetradecameric structure into its heptameric constituents (Gersch et al. 2014b).

1.3.4. ClpP modulation and multi-drug resistant (MDR) bacteria

The effectiveness of ClpP activators against MDR is registered in the scientific literature. To illustrate this, ADEPs exerted potent activity against methicillin-resistant *Staphylococcus aureus* (MRSA) (Arvanitis et al. 2016) and vancomycin-resistant *Enterococci* (VRE) (Mroue et al. 2019). Pre-treatment of mice with the variant ADEP B315 before the injection of lethal MRSA strain assured a survival benefit, being more effective than the administration of vancomycin.

1.3.5. ClpP modulation for the eradication of biofilms

Various procedures combat biofilm, including physical removal, chemical treatments, antimicrobial coatings, and quorum sensing inhibitors (Yin et al. 2021; Sadekuzzaman et al. 2015). Once established in living organisms, some techniques are adopted as biofilm disruptors: percussion, low-level laser, ultrasound, pulsed magnetic field, etc (Basso et al. 2011; Baumann et al. 2009;

Khan et al. 2016; Sousa Farias et al. 2016). However, in terms of antimicrobial chemotherapies, the options are scarce since, according to previous discussion, the mechanism of action of most antibiotics on the market does not insult dormant cells.

ClpP participates in the biofilm formation, as concluded from Table 5, as well as in its eradication (Zheng et al. 2020; Wang et al. 2007; Brown Gandt et al. 2018; Liu et al. 2017), once ClpP activation and inhibition can promote the unbalancing of the transcription factors. For instance, in the case of *Staphylococcus epidermidis*, using a mutant strain without the *clpP* gene helped better elucidate the building mechanism of biofilm. Semiquantitative assays demonstrated that the mutant was 22-fold less prone to produce biofilms than wild-type cells. The attachment capability of the mutant to polystyrene was also compromised by the upregulation of *agr* quorum-sensing system in the absence of ClpP (Frees et al. 2005).

Table 5- Transcription factors regulated by ClpP and their role in biofilm formation.

Transcription factor	Organism	Role in biofilm formation	ClpP regulation mechanism
RpoS [1]	*Escherichia coli*	Master regulator of stationary phase and stress response	ClpP degrades RpoS, balancing its levels for optimal biofilm formation
Spx [2]	*Staphylococcus aureus*	Regulates genes involved in stress response and biofilm formation	ClpP degrades Spx to control its activity under stress conditions
AlgU [3]	*Pseudomonas aeruginosa*	Controls alginate production, critical for biofilm matrix formation	ClpP regulates the stability of AlgU, influencing biofilm matrix synthesis
BrpR [4]	*Vibrio cholerae*	Activates biofilm-associated genes, enhancing biofilm formation	ClpP degradation of BrpR modulates its activity, affecting biofilm formation
CcpA [5]	*Bacillus subtilis*	Control carbon catabolite repression, impacting biofilm formation	ClpP regulates CcpA, affecting biofilm-related metabolic processes
CsgD [6]	*Escherichia coli*	Regulates production and cellulose synthesis, key components of biofilms	ClpP indirectly influences CsgD levels by modulating upstream regulators
PqsR [7]	*Pseudomonas aeruginosa*	Regulates quorum sensing and biofilm formation through *Pseudomonas* quinolone signal	ClpP regulates PqsR indirectly by controlling related regulatory proteins

[1] (Adnan et al. 2010), [2] (Pamp et al. 2006),[3](Bazire et al. 2010),[4] (Hwang et al. 2021), [5] (Stanley et al. 2003), [6] (Da Re and Ghigo 2006), [7] (Guo et al. 2014).

In another scenario, ClpP dysregulation of *Staphylococcus aureus* with ADEP-4, a more potent ADEP derivative, resulted in the depletion of a chronic biofilm infection (Conlon et al. 2013). According to a qualitative proteomic analysis, the activation of uncontrolled activity promoted extensive protein degradation, culminating in the subsequent killing of persister cells. As ClpP is not essential to *Staphylococci*, null mutants tend to grow after 3 days of treatment with ADEP-4. However, the combined use with rifampicin, linezolid, or ciprofloxacin eradicated the stationary phase *S. aureus* in 72 h, *in vitro* and in a deep-seated mouse thigh model (Conlon et al. 2013).

When comparing the two previous contexts, it is possible to conclude that a regulated ClpP function is a key factor for biofilm formation. Both inhibition and activation hamper the fixation and survival of dormant cells, respectively. Therefore, these strategies can be explored to eliminate chronic bacterial infections.

The discovery/production of new non-enzymatic modulators is important for elucidating the structural/functional aspects of the peptidase and further comprehending the whole biochemical pathway to overcome bacterial resistance with ClpP. To this date, published ClpP-ligand complexes and mutants revealed some connections between the protein activation/inhibition and its function. In any case, some mechanisms involved with the protein's modulation still lack detailed explanation, biochemically and biophysically. One of these observations is the interaction between ClpP and boron-based compounds, especially the peptidomimetic boronates.

1.4.   Peptidomimetic boronates as ClpP modulators and their paradoxical mode of action

Boron-containing compounds constitute a group of drugs of clinical relevance, even though that element is not naturally found in living organisms. Given its chemical reactivity and versatility, boron can form covalent bonds with carbon, nitrogen, and oxygen in building blocks of organic synthesis (Diaz and Yudin 2017). Besides that, boronates act as potential enzyme modulators for their ability to form covalent bonds with the nucleophilic sidechains of certain amino acid residues, such as serine and threonine in active sites, inhibiting enzymatic activities (Smoum et al. 2012). In both residues, there is a hydroxyl group with a lone pair of electrons

on the oxygen atom to be donated to the electron-deficient boron (Charzewski et al. 2021). The negative charge that may develop on the boron atom when covalently bound to a protein is stabilized by the delocalization of electron density promoted by oxygen. (Grams et al. 2024).

These chemical properties have resulted in various therapeutical applications, from cancer (Scorei and Popa 2010) to onychomycosis (Jackson et al. 2020). In 2003, bortezomib (Figure 10), the first boron-based drug, was approved by the Food and Drug Administration (FDA) in the United States (Fernandes et al. 2019). Bortezomib is considered a first-line treatment for multiple myeloma by inhibiting the 26S proteasome (Bonvini et al. 2007).

Studies with ClpP and boronate compounds also provided relevant observations. Firstly, in a complex with ClpP and a peptidomimetic boronate named 43Hf, the tetradecameric structure was not destabilized or compressed like with other inihibitors (Gersch et al. 2014a). Thermal shift assays showed that the stability of the protein assembly even increased with a variation of melting temperature (T_M) from 50°C to approximately 70°C. 43Hf was the best hit from a screening containing 2632 molecules (Ju et al. 2020), indicating that the peptidomimetic portion plays a role in the protein-ligand interaction, and confirming the structural stabilization demonstrated by a work with an inactive mutant of ClpP and peptides (Kim and Kim 2008). In this last case, it was additionally confirmed that the presence of oligopeptides in the active sites induced the proper alignment of the catalytic triads and reduced the distance between Ser98, His123, and Asp172.
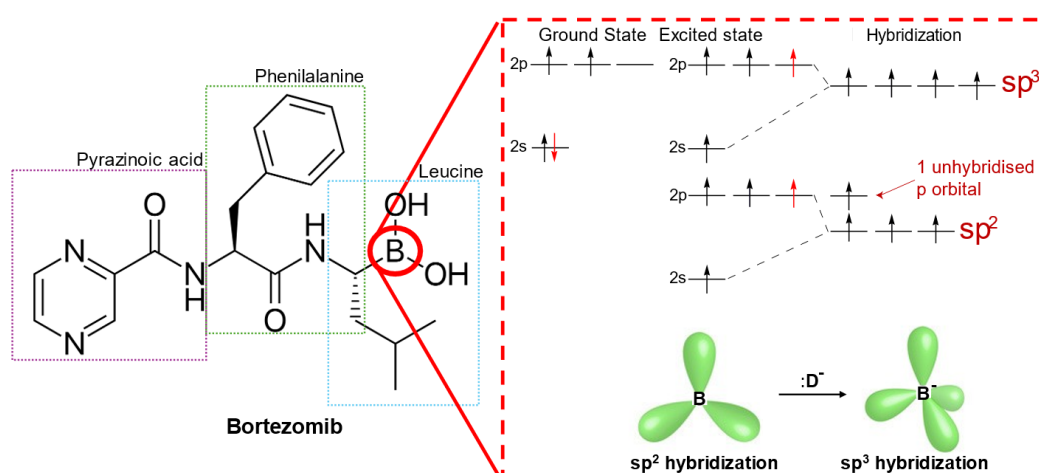
Figure 10 – Bortezomib, a canonical proteasome inhibitor, is an example of a boron-based compound. Adapted from Micale et al. 2013.

In a recently published work, the "cornerstone" of this thesis, another anticancer peptidomimetic boronate, ixazomib, complexed with ClpP from *Staphylococcus epidermidis* (*Se*ClpP) illustrated how that ligand can influence protein activity and oligomerization. It was the first demonstration that a canonical proteasome inhibitor induces the assembly of the tetradecameric enzyme, a process previously associated with ClpP modulation via allosteric sites (Alves França et al. 2024). At the same time, ixazomib modulates the protein in a paradoxical way, activating proteolysis through interactions in the catalytic sites (Alves França et al. 2024), as detected in investigations with bortezomib as well. The in-depth mechanism behind this is still to be fully elucidated, notwithstanding.

1.5. Biophysical tools for the characterization of ClpP and ClpP-ligand complexes

Structural perspectives of proteins are significant to understand their role in treating bacterial infections. Applying low and high-resolution techniques unveils features of enzymes under the influence of various physicochemical conditions and other molecules. In this scenario, small-angle X-ray scattering (SAXS) is one of the experimental approaches worth considering. Firstly discovered by André Guinier in 1938 (Gräwert and Svergun 2020), SAXS was expanded from studies of metallic alloys to biological macromolecules in the 1960s (Pouget et al. 2019), passing through advances with synchrotron radiation in the 1970s (Bras et al. 2014) and breakthroughs in data processing methods in the 1990s (Blanchet and Svergun 2013). This evolution produced some advantages: non-destructive measurements, reduced sample amount, and the ability to characterize systems in native or close-to-native states. Furthermore, SAXS can provide critical information on the overall shapes, oligomeric states, and dynamics of biological molecules in solutions. Figure 11 shows an image of the SAXS beamline in EMBL's outstation in Hamburg, Germany.

For multimeric proteins like ClpP, research hinged on SAXS measurements is commonly beneficial to complement X-ray crystallography. For example, crystal packing may cause difficulties in distinguishing net changes associated with mutations and interactions with ligands.

Figure 11 – P12 beamline for Batch-SAXS and SEC-SAXS experiments. Picture obtained from EMBL, 2024.

Sometimes, flexible parts of a macromolecule cannot be resolved from X-ray diffraction, given the lack of electron density around certain amino acid residues. In this regard, an issue frequently found in crystal structures of ClpP is the omission of the N-terminal loops in the axial pores. Because of this, the interpretation of how ligands may influence this region is compromised. To better explain this *status quo*, the complete structure of *S. epidermidis* ClpP (*Se*ClpP) applying the AlphaFold 3 (AF3) server and the native *S. aureus* ClpP (*Sa*ClpP) are compared in Figure 12.
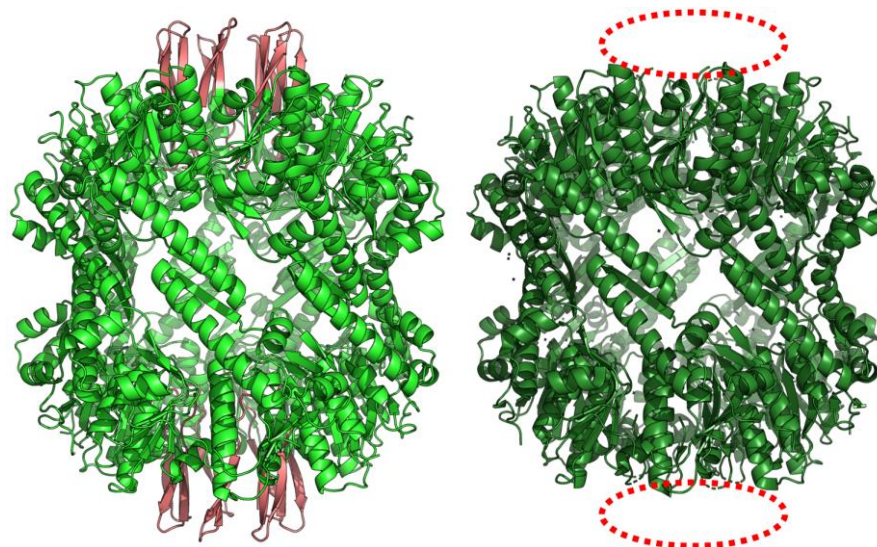
Figure 12 – Depiction of the extended state of *Se*ClpP obtained from AlphaFold 3 (light green) (Abramson et al. 2024) and as an experimental crystal structure (dark green) (Gersch et al. 2012). The N-terminal loops depicted in rosé could not be resolved by X-ray diffraction in many cases.

Both models represent the extended and closed state of the peptidase, but the difference in terms of the pore's diameter is considerable. This is the consequence of a partially non-modeled N-terminal loop in *Sa*ClpP. As a low-resolution experiment, SAXS cannot provide an in-depth description of the secondary structures or atomic placement in the same region, and the protein's envelope can only indicate the enlargement of the axial pores, though.

X-ray crystallography was originated in 1912 with the work of Max von Laue, William Henry Bragg, and William Lawrence Bragg (Pope 1997). If X-rays were waves and regularly spaced atoms constituted crystals, van Laue hypothesized that X-rays could be diffracted. The diffraction pattern of X-rays that passed through a copper sulfate crystal on photographic plates confirmed the hypothesis. From the rationale of those initial experiments to this date, many advances led to the use of X-ray beams to describe the world at a whole new level. The construction of powerful synchrotrons (Figure 13) in many regions granted the obtaining of a high amount of datasets that give structural information of relevant enzymes, their functions in various conditions, and their interactions with a plethora of drugs and drug-like compounds.
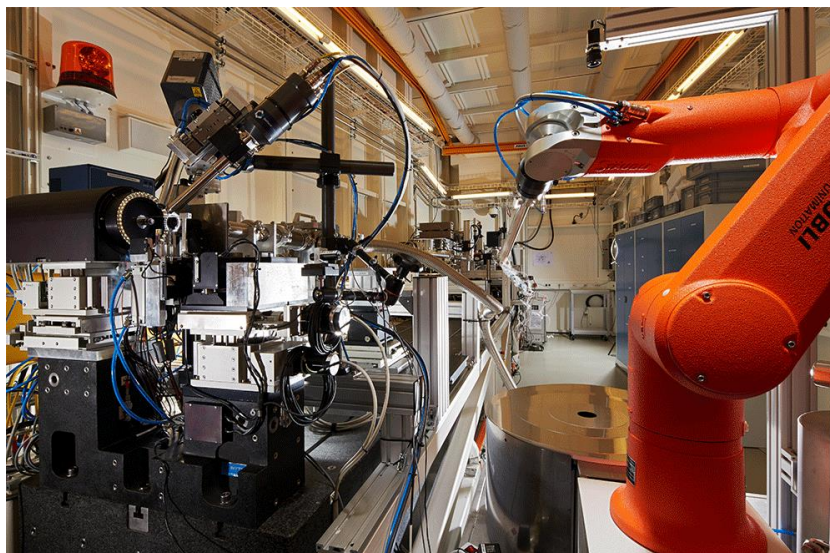
Figure 13 – P11 beamline and the sample robot for data collection with single crystals (MX crystallography). Picture obtained from Photon Science, 2024.

The Protein Data Bank (PDB) is the biggest source of crystal structures online (Bittrich et al. 2024; Burley et al. 2024). In this archive, it is possible to find 186,358 crystal structures, representing approximately 84% of all the available entries. Among them, there are ClpPs from humans to bacteria. This availability conferred

the possibility to delineate the mechanisms behind the modulated action of ClpP on the treatment of microbial infections. Nevertheless, the discussions about the paradoxical influence of peptidomimetic boronates on the protein's activity point out that there is more to be discerned. This lack of information is the "driving force" of the present PhD thesis. Here, low and high-resolution data are combined, in order to provide insights into the relationship between ClpP and ixazomib in an "alternative" allosteric activation that is intriguing for being propagated from the catalytic sites.

2. Aims of the Present Study

So far, the relevance of ClpP in drug development research has been addressed, and a summary of studies in recent years has shown advances in the characterization of the protein's structure and functionality. Publications have demonstrated the mechanisms behind the most diverse mutations, inhibitors, and activators. On the other hand, there is still a lot to be learned about modulating the activity of the enzyme in question.

In this context, peptidomimetic boronates are good examples. As canonical inhibitors, they bind to the catalytic site of various proteases. However, when they form complexes with ClpP, they do not behave like canonical inhibitors: in tests with bortezomib, it was discovered that this drug promoted a paradoxical allosteric activation defined as organism dependent. Even so, a more complete description of what happens is still not clear. Therefore, in order to develop a more detailed study of coordinated modulation by the same class of ligands, the goals of this PhD thesis are:

Use of ixazomib, another peptidomimetic boronate, as a potential protease activator of *Staphylococcus epidermidis* ClpP (*Se*ClpP).

Adoption of SAXS techniques to verify conformational changes in the SeClpP-ixazomib complex.

Analysis, at the atomic level, of changes in the orientation of amino acid residues important for enzyme activation, as well as interactions between ligand and protein.

Enzymatic assays and modulation: monitoring the evolution of peptidolytic and proteolytic reactions mediated by ixazomib, by quantifying variations through the concept of relative activity.

Other biophysical techniques: isothermal titration calorimetry (ITC) and nanoDSF were performed to evaluate the stability of the native protein and the protein-ligand complex.

3.   Materials and Methods

3.1.   List of devices used

The instruments used for the experiments are listed in Table 6.

Table 6 – List of instruments.

Type of device	Model	Manufacturer
Orbital shaker	Innova 44	New Brunswick Scientific
	KS 3000 I control	IKA
Incubator	BD 56	Binder
Roller shaker	RS-TR05	Phoenix instruments
DLS instrument	SpectroLight 600	Xtal Concepts GmbH
	SpectroLight 300	Xtal Concepts GmbH
	Möbius	Wyatt
FPLC system	ÄKTAPurifier 10	GE Healthcare
	ÄKTA Start	Cytiva
Protein gel electrophoresis	SE 245 Dual Gel Caster	Hoefer
Power supply for electrophoresis	EV231	PEQLAB Biotechnology
Crystallization robot	Honexbee 961	Genomic Solutions
Magnetic stirrer	VMS-A	VWR International
Microscope	SZX12	Olympus
	CLSM	Zeiss
UV spectrophotometer	NanoDrop ND-1000	Thermo Fisher Scientific
	NanoDrop ND-2000	
pH meter	SevenEasy	Mettler-Toledo
UV/Vis spectrophotometer	GeneQuantTM 1300	GE Heathcare
Thermomixer	ThermoMixer comfort	Eppendorf
Ultrasonic homogenizer	Soniprep 150	MSE
Analytical balance	TE3102S	Sartorius
	CP2245-OCE	

Type of device	Model	Manufacturer
Centrifuge	Multifuge X1R	Thermo Fisher Scientific
	5415 R	Eppendorf
	Minispin Plus	Eppendorf
	5418 R	Eppendorf
nanoDSF	Prometheus nDSF	Nanotemper
ITC	MicroCal PEAQ-ITC	Malvern Panalytical
Freezer -20°C	Liebherr premium	Liebherr International S.A.
Freezer -80°C	B35-85	FRYKA-Kältetechnik GmbH
TECAN plate reader	Infinite M Flex	TECAN
Magnetic stirrer	VMS-A	VWR International LLC

Table 7 - List of general consumables

Item	Manufacturer
Falcon-like tubes	Sarstedt
Pipette tips	Sarstedt
Serological pipettes	Fisher Scientific
Reaction vessels	Sarstedt
Amicon Ultra 4, 15, 0.5; MWCO 10, 50, 100 kDa	Merck Millipore
Dialysis membrane	Roth
Ni-NTA agarose matrix	Qiagen
Syringes: 1, 5, 10, and 20 mL	VWR
Syringe filter: 0.22 and 0.45 µm	VWR

3.2. Compounds used

Unless otherwise stated, the chemicals (analytical grade) used in the present work's experiments were obtained from the following suppliers: VWR, Sigma-Aldrich, SERVA, Merck, Fluka, and Applichem.

3.3. Sample buffers

The preparation of media and buffers involved the use of distilled water (dH$_2$O), sodium acetate, HEPES, Tris base, sodium chloride, dithiothreitol, and glycerol. The combination of these compounds and the final pH value depends on the experiment, and the proper amounts are described in the "Methods" section when applicable.

Table 8 - Composition of acrylamide gels for SDS-PAGE.

Gel type	Component	Volume (mL)
Stacking gel (4%)	Acrylamide/bisacrylamide (37.5:1): 30% solution	2.0
	Stacking gel buffer	3.8
	10% (w/v) SDS solution	0.15
	TEMED	0.015
	10% /w/v) APS solution	0.075
	ddH2O	9.2
Separating gel (15%)	Acrylamide/bisacrylamide (37.5:1): 30% solution	15.0
	Separating gel buffer	7.5
	10% (w/v) SDS solution	0.3
	TEMED	0.015
	10% (w/v) APS solution	0.15
	ddH$_2$O	7.2

Table 9 - Media composition and antibiotic concentration

Growth and expression media	Composition
Luria-Bertani, Lennox (LB) medium	Tryptone (10 g/L), yeast extract (5 g/L), NaCl (10 g/L)
LB-agar medium	1.5% (w/v) of agar in LB medium
TB medium	12 g tryptone, 24 g yeast extract, 4 mL glycerol, 2.31 g KH_2PO_4, 12.54 g K_2HPO_4
SOC medium	20 g/L tryptone, 5 g/L yeast extract, 0.5 g/L NaCl, 25 mL of 1 MKCl, 10 mL of 2 M $MgCl_2$ and 1 M $MgSO_4$, 20 mL 2 M dextrose.
Antibiotic	**Working concentration**
Ampicillin	100 µg/mL
Kanamycin	50 µg/mL

Methods

3.4. Gene selection, cloning, preparation of competent cells, and bacterial transformation

UniProt database (https://www.uniprot.org) provided the *clpP* encoding gene sequence from *Staphylococcus epidermidis* (UniProtKB A0A0N1MQL5). The company Biocat (https://www.biocat.com) received the complete native sequence in FASTA format and the request for codon optimization, considering *E. coli* expression systems (Figures 14a and 14b). After cloning, copies of the open reading frame (ORF) of the *clpP* gene were inserted into the vector pET28a(+) (Figure 14c), using the restriction enzymes NcoI and XhoI. The GenScript server (https://www.genscript.com) indicated that there were not any sites in the ORF for those enzymes to cleave.

To improve protein purification, removing the stop codon (TAA) from *clpP* allowed the inclusion of a histidine expression tag (6x His-Tag) at the C-terminal position. Initially, the idea was to add the tag to the N-terminal portion, but in this case, it would be autoproteolytically cut after protein expression (Zhang et al. 2011).

For a high-yield expression of heterologous ClpP, the *E.coli* system BL21 Star (DE3) (Studier 1991) was selected, as ClpP is not toxic for the bacterium. Aiming

to prepare chemically competent cells, 50 µL from the cell line culture grown overnight in LB medium were subsequently cultivated in 250 mL SOB medium at 37°C and 200 rpm, until the optical density (OD) was between 0.4 and 0.6. Afterward, the culture flask was placed on ice for 10 minutes, and the suspension was then centrifuged at 4000 rpm and 4°C, for 10 minutes. The pellet was resuspended in 80 mL ice-cold TB solution (10 mM PIPES pH 6.7, 250 mM KCl, 15 mM $CaCl_2$, and 55 mM $MnCl_2$) and kept on ice for another 10 minutes. A second round of centrifugation was performed under the same conditions as before, and the new pellet was resuspended in 20 mL ice-cold TB solution / 1.4 mL DMSO and placed on ice for an additional 10 minutes. In this final step, 50 µL aliquots of the resulting material were distributed into 1.5 mL Eppendorf-like tubes and immediately frozen in liquid nitrogen for storage in an ultra-freezer (- 80°C).

One of the previous aliquots was thawed prior to bacterial transformation. 0.5 – 1 µL from Biocat plasmid solution (pET28a(+) with *clpP* gene) (approx. 200 ng/µL) was mixed with the suspension containing the competent cells, and the mixture was kept on ice for 30 minutes. The tube was then put into a Thermomixer Comfort (Thermo Fisher Scientific, Germany), at 42°C, for 90 seconds and transferred to ice for 5 minutes. This heat stress makes the cell membranes more permeable for a while, allowing the uptake of DNA molecules from the surrounding environment (Rahimzadeh et al. 2016).

Bacterial growth took place in 1 mL SOC medium, also in a Thermomixer Comfort (Thermo Fisher Scientific, Germany) at 37°C, for 3 hours. The final culture was centrifuged, and the cells were resuspended in 100 µL SOC medium for ulterior streaking on agar-LB medium supplemented with 50 µg/mL kanamycin (antibiotic resistance acquired after transformation with pET28a(+)). After 16 hours, some colonies were seen, harvested, and used to prepare glycerol stocks to be frozen in liquid nitrogen and stored in an ultra-freezer at -80°C.
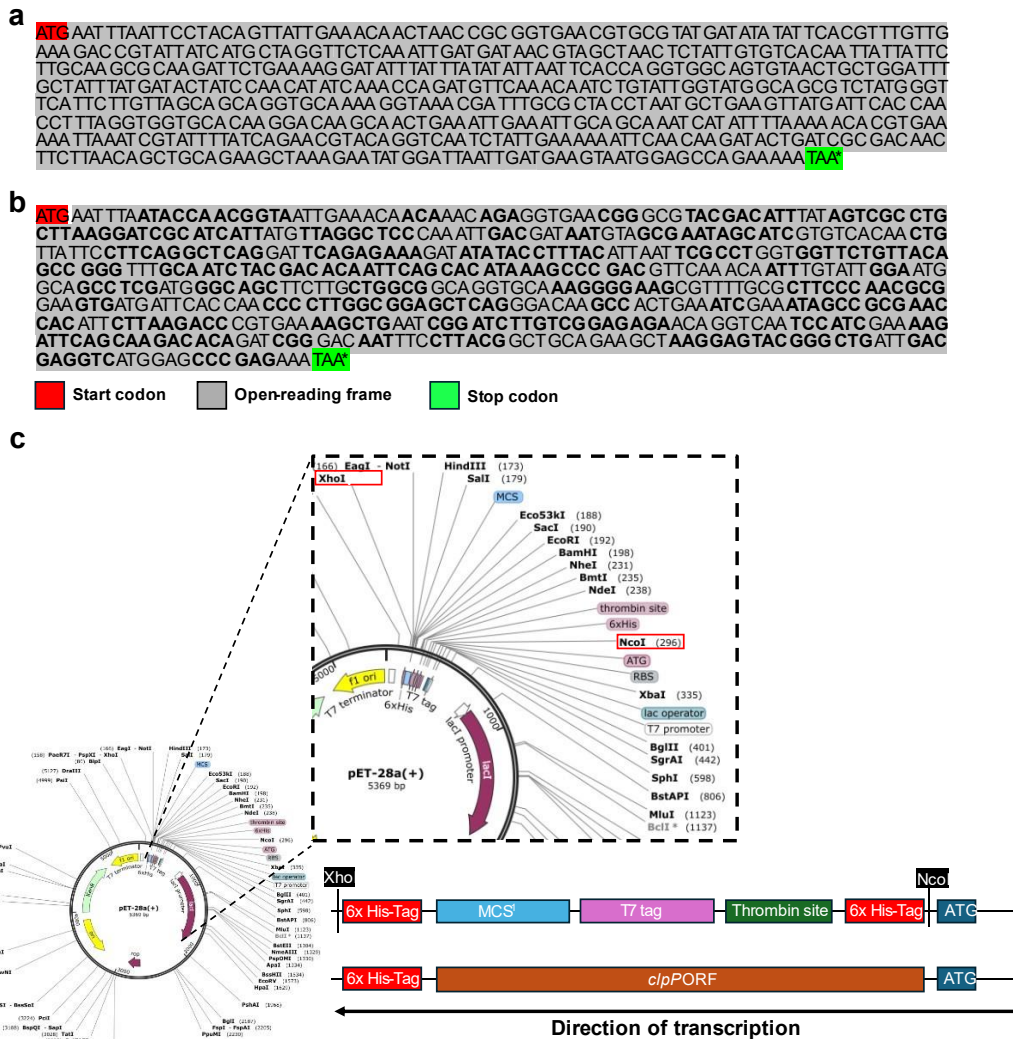
Figure 14 – (**a**) Encoding gene sequence of ClpP from *S. epidermidis* (*Se*ClpP) found on UniProt database (UniProtKB: A0A0N1MQL5). (**b**) Gene of *Se*ClpP after codon optimization for heterologous expression in *E. coli* (altered codons are in bold). (**c**) The illustration of the vector pET28a(+) and the region where the gene copy was inserted is zoomed in. The removed portion of the plasmid between the restriction sites for NcoI and XhoI is displayed. The insert (brown color), the *clpP* gene, is also shown after the assembly.

3.5. Heterologous expression of *Se*ClpP and its purification

Glycerol stock with transformed *E. coli* BL21 Star (DE3) cells was thawed, and 50 µL were taken to be added to 60 mL LB medium supplemented with 50 µg/mL kanamycin for overnight pre-inoculum, in the bench shaker KS3000 I control (IKA, Germany), at 37°C and 180 rpm. 10 mL of the obtained suspension were transferred to 1 L fresh LB medium containing 50 µg/mL kanamycin, and the OD between 0.6 – 0.8 was reached in 5 – 6 hours. At this point, the heterologous

expression started once induced by 0.5 mM IPTG. During this step, the temperature and flask stirring were kept constant under 18°C and 180 rpm in an orbital shaker Innova 44 (New Brunswick Scientific, Germany) for approx. 16 hours.

The pellet was collected and resuspended in lysis buffer composed of 50 mM Tris base (pH 8.0), 300 mM sodium chloride (NaCl), and 2 mM DTT, or 50 mM Tris base (pH 8.0), 300 mM NaCl, and 20 %w/v glycerol. The buffer supplementation with glycerol will be discussed later.

The purification procedure is divided into two main parts: immobilized metal affinity chromatography (IMAC), the first one, and size-exclusion chromatography (SEC), the second one. For IMAC, nickel resin (Ni-NTA) (QIAGEN, The Netherlands), in a bench column (Bio-Rad, USA), was selected to take advantage of the histidine tag connected to the protein. This resin is constituted by nitrilotriacetic acid (NTA), a tetradentate chelating ligand, in a highly cross-linked 6% agarose matrix. NTA binds to Ni^{2+} by four coordination sites (Crowe et al. 1996). When the ClpP solution is added to the column, the enzyme of interest with 6x His-Tag gets trapped in Ni-NTA and is eluted by 300 mM imidazole once the unbound/weakly bound species are removed.

In sequence, the device ÄKTA Purifier 10 (GE Life Sciences, Sweden) coupled with the SEC column HiLoad 26/60 Superdex 200 preparative grade (pg) composes the following stage of purification: size exclusion chromatography (SEC), also known as the polishing step. Since ClpP may be present in different oligomeric states, a big column (325 mL) like the one mentioned above is more efficient in separating the protein into distinct fractions.

At this moment, the void was not intended to be collected; therefore, the purification method set in Unicorn 5.31 software (GE Life Sciences, Sweden) discarded 40% of the initial column volume (CV) once the run had started.

In Figure 15, there is an illustration of the purification steps.
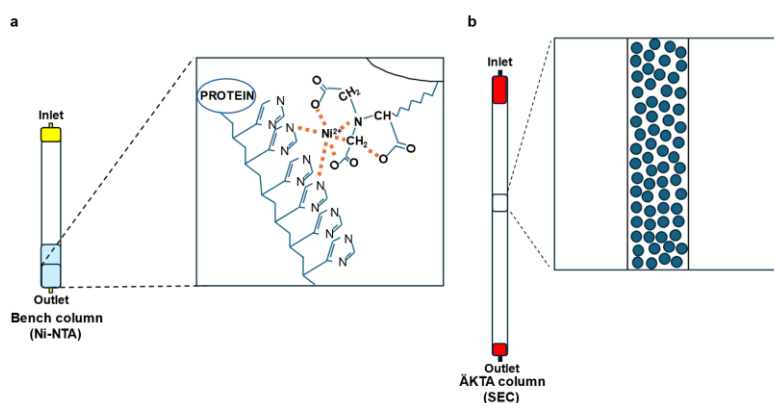
Figure 15 – Depiction of (**a**) IMAC with Ni-NTA matrix and (**b**) SEC as a polishing step.

3.6. Use of SDS-PAGE, Native-PAGE, and DLS for quality assessment of *Se*ClpP

3.6.1. SDS-PAGE and the identification of protein species in a sample

Sodium dodecyl sulfate polyacrylamide electrophoresis (SDS-PAGE) is a technique that separates proteins according to their molecular weight (MW) (Brunelle and Green 2014). After the macromolecules are denatured and coated with sodium dodecyl sulfate (SDS), they are loaded into the polyacrylamide gel and migrate through the matrix inside. The migration depends on each macromolecule's MW/volume ratio and is induced by an electric current. The proteins move toward the positively charged electrode because of the overall negative charge conferred by SDS. When the electrophoresis is done, the result allows the user to check the sample purity.

Considering the experiment's benefits, the same procedure was adopted after the purification of *Se*ClpP. The fractions corresponding to each peak were separately pooled to be submitted to SDS-PAGE. As two prominent peaks were observed after SEC, fraction pooling resulted in two final protein samples. 7.5 µL from each sample was added to the 10 µL buffer and 2.5 µL dithiothreitol (DTT) in 1.5-mL Eppendorf-like tubes. DTT disrupts disulfide bonds, maintaining the reduced state of the *Se*ClpP and avoiding aggregate formation.

After mixing, the SDS-PAGE samples were heated to 95°C for 5 minutes in a Thermomixer Comfort (Thermo Fisher Scientific, Germany) for protein denaturation. This step was followed by gel loading and the electrophoresis itself in SE 245 Dual Gel Caster (Hoefer, Germany). It is relevant to highlight that a protein marker/ladder (Thermo Fisher Scientific, Germany) was also used. This

marker assists in estimating the MW of the macromolecules under analysis and monitoring the gel run.

During the first step of electrophoresis, for the first 20 minutes, the power supply EV231 (PEQLAB Biotechnologie, Germany) was set at 120 V and 25 mA. The voltage was increased to 250 V for the remaining time, approx. 90 minutes, and the current was kept the same as beforehand.

When the SDS-PAGE was done, the gel was treated with a staining solution composed of Coomassie Brilliant Blue for approximately 1 hour and finally with a homemade destaining solution twice for approximately 1 hour each time. The proteins could be identified as gel bands.

3.6.2. Native-PAGE and the identification of the oligomerization state of *Se*ClpP

Native polyacrylamide gel electrophoresis (native-PAGE) can also be used to assess the quality of *Se*ClpP samples (Wittig and Schägger 2008). In this case, denaturing conditions, such as SDS and sample heating, are not applicable. The protein is kept in its native conformation and functional state.

The gel used in native-PAGE experiments is a mixture of 4% v/v acrylamide and 16% v/v bisacrylamide monomers (SERVA, Germany). Through an electric field, macromolecules migrate through the gel pores according to their sizes and charges.

Among the native-PAGE options, the blue polyacrylamide gel electrophoresis (BN-PAGE) (Wittig et al. 2006) was chosen for the analysis of *Se*ClpP samples, as it resulted in the best conditions for visualizing the results. SERVA (SERVA, Germany) provided the kit with precast gels, protein markers, sample buffer for BN, running buffers (10 x anode and 10x cathode), and a Coomassie G-250 solution.

For this experiment, frozen stocks of *Se*CpP samples were thawed, and the NanoDrop ND-2000 / ND-1000 devices (Thermo Fisher Scientific, Germany) determined the protein concentration at 280 nm. The resolution of the gel bands depends on the *Se*ClpP concentration: if high amounts were loaded, well defined bands could not be seen. Then, after checking various dilutions, 3 mg/mL was found to be the best value for properly observing oligomers.

The protein sample was mixed with 2x sample buffer and immediately loaded into the gel. The 1x anode and 1x cathode buffers were previously added to the

electrophoresis apparatus SE 245 Dual Gel Caster (Hoefer, Germany). The Coomassie G-250 solution was 1000x diluted in the cathode buffer, as this dye replaces SDS by conferring a negative charge to the macromolecules. The power supply was set at 50 V for the first 10 minutes, then at 200 V for ca. 120 minutes. The system was monitored during the run to prevent its heating. If the temperature increases considerably, protein denaturation may happen.

When the electrophoresis was over, the gel was washed with demineralized water and incubated with the staining solution. After 30 minutes, this solution was replaced by a destainer with subsequent incubation for 60 minutes. If the blue background was still intense, a fresh destainer was used for another 60 minutes.

As in SDS-PAGE, the protein marker (Thermo Fisher Scientific, Germany) conferred the MW estimation of the protein bands.

3.6.3. DLS and sample monodispersity/polydispersity

Dynamic-light scattering (DLS), also known as photon correlation spectroscopy or quasi-elastic light scattering, is a technique used to measure the size of molecules in a solution (Stetefeld et al. 2016). In a DLS device, a beam of light that passes through a sample is scattered by its particles. Regarding proteins, the fluctuations in the intensity of scattered light over time give information about the size distribution of the macromolecules in a solution. This temporal correlation can be represented by the following equations found in the scientific literature (**1**) (Stetefeld et al. 2016):

$$G_2(\tau) = \langle I(t)I(t+\tau)\rangle \tag{1}$$

$I(t)$ is the intensity of the scattered light at time t

t is time

τ is the lag between two time-points

Once normalized, the function $g_2(\tau)$ is given (**2**):

$$g_2(\tau) = \frac{\langle I(t)I(t+\tau)\rangle}{\langle I(t)\rangle^2} \tag{2}$$

The angle brackets in (**1**) and (**2**) indicate the averaging of properties over time t.

$G_2(\tau)$ is a second-order correlation function that is related to the motion of the macromolecules under investigation. Nonetheless, there is no precise way to determine how particles individually move in solution. Therefore, instead of $G_2(\tau)$, the motion of particles relative to each other is mathematically described by an electric field correlation function, $G_1(\tau)$, or a first-order correlation function (**3**):

$$G_1(\tau) = \langle E(t)E(t+\tau)\rangle \tag{3}$$

  E(t) scattered electric field at time τ;

  E(t + τ) scattered electric field at time t + τ

$g_1(\tau)$ is resulted from the normalization of $G_1(\tau)$ (**4**):

$$g_1(\tau) = \frac{\langle E(t)E(t+\tau)\rangle}{\langle E(t)\rangle^2} \tag{4}$$

The Siegert relation (Wang et al. 2021) combines $g_1(\tau)$ and $g_2(\tau)$, resulting in the following equation (**5**):

$$g_2(\tau) = B + \beta|g_1(\tau)|^2 \tag{5}$$

  B is the baseline (~1);

  β is the coherence factor dependent on the detector area, optical alignment, and scattering properties of macromolecules.

Considering a monodisperse system and the Brownian motion (Hassan et al. 2015) of particles, the electric field correlation factor, or autocorrelation function (ACT), can be calculated as follows (**6**):

$$g_1(\tau) = 1 + \beta e^{-2D_\tau q^2 \tau} \tag{6}$$

  D_τ is the diffusion behavior of macromolecules;

  q is the scattering wave vector (Jin et al. 2022).

The relationship between D_τ and the hydrodynamic radius (R_H) of proteins is found in the Stokes-Einstein equation (**7**) (Falke and Betzel 2019):

$$D = \frac{k_B T}{6\pi\eta R_H}$$ (7)

  k_B is Boltzmann's constant (1.380648×10^{-23} J.K^{-1})

  T is temperature

  η is viscosity

Besides the dispersity profile in a solution, by using the equation above and DLS measurements, the calculation of the R_H indicates whether the macromolecule of interest is present. Here, the particle that scatters the light is considered a sphere (Falke and Betzel 2019).

After SEC, the purified *Se*ClpP is centrifuged at 21,600 x g and 15°C, for 1 hour in Eppendorf 5415 R centrifuge (Eppendorf, Germany) to avoid the influence of aggregates on DLS measurements. Then, 60 µL of the sample is added to the quartz cuvette (Wyatt, USA) that is positioned in the chamber where the laser beam passes through the solution, and the intensity fluctuations of the scattered light at a specific angle is measured.

Technical details about the DLS device used in this experiment are below (Table 10):

Table 10 – Supplier specifications of the DLS device (Wyatt, 2024).

Device name	Wyatt Möbius (Waters, USA)
Mobility measurements	
Size range (radius)	1 nm – 50 Mm
Detection angle	163.5°
Size sensitivity	0.05 mg/mL (lysozyme)
Maximum detector auto attenuation	3000x
Sample cell / minimum sample volume	Quartz cuvette / 45 µL
Sample temperature control	4 – 70°C
Optics	
Light source	50mW diode-pumped, solid-state, single-longitudinal-mode laser
Laser wavelength	532 nm

All the measurements were performed at 20°C, acquision time: 20 s, number of acquisions: 20, interval between acquisition: 5 s. The degree of monodispersity was evaluated by inspecting the histogram in the graph % intensity *vs* radius (nm) and % number *vs* radius (nm). The software for data processing was Dynamics software (Wyatt, USA).

A schematic concept of a DLS experiment is shown in Figure 16.
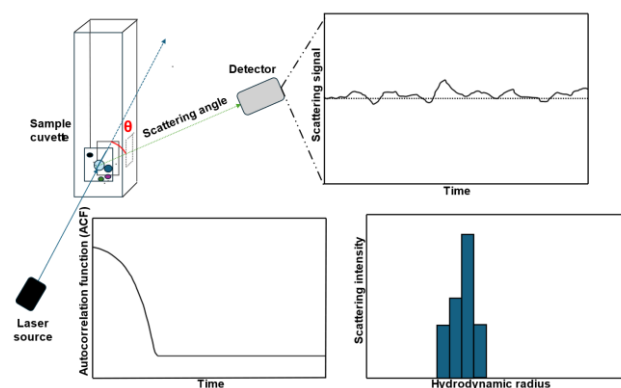
Figure 16 – General illustration of main elements in DLS measurements.

3.7. Structural analysis of *Se*ClpP in solution

3.7.1. SAXS measurements

Small-angle X-ray scattering (SAXS) produces low-resolution information about the shape, size, and oligomeric state of a protein, from a nanometer to a micrometer scale (Skou et al. 2014). The electron cloud surrounding the atoms in a macromolecule can diffract an X-ray beam, and the scattered waves are recorded by a detector opposite to the X-ray source (Figure 17). From the data collected, structural details about the sample are extracted, especially at lower angles up to 0.5°.
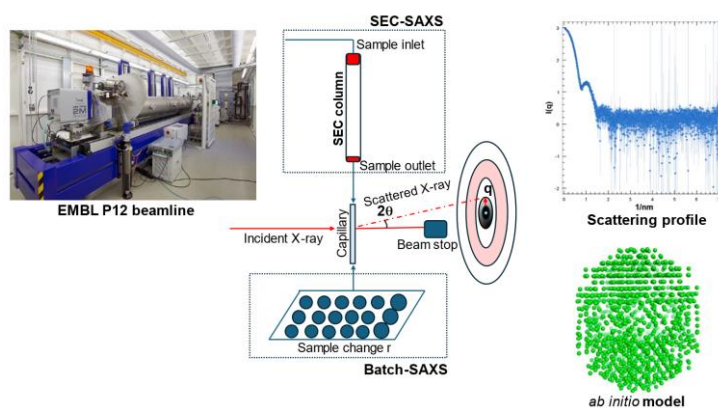
Figure 17 – P12 beamline (EMBL/PETRA III) in Hamburg, Germany. Illustration of SEC-SAXS and Batch-SAXS setups. Regardless of the method of choice, the sample is conducted to a capillary where the incident X-ray beam is scattered. The recorded one-dimensional scattering profile is then used for the low-resolution structural analysis and the *ab initio* modeling of native protein and protein-ligand complexes in solution.

The important equations for the SAXS measurements and processing are below, and they were adapted from Putnam et al. 2013:

$$q = \frac{4\pi}{\lambda}\sin(\Theta)$$
(8)

λ: wavelength of the incident X-rays.

θ: scattering angle.

$$I(q) = |F(q)|^2 S(q)$$
(9)

I(q): scattering intensity;

F(q): Fourier transform of the electron density distribution of the sample;

S(q): structure factor.

$$I(q) = I(0)e\left(-\frac{q^2 R_G^2}{3}\right)$$
(10)

I(0): intensity at q=0;

R_G: radius of gyration.

$$I(q) \sim q^{-4}$$
(11)

Scattering vectors (q), in some plots also indicated as s, describe the momentum transfer of the incident X-rays in (**8**) and are spatially distributed within the sample, constituting the structure factor (S(q)) in (**9**). S(q) is related to the scattering intensity (I(q)) through the Fourier transform (F(q)) of the electron density of molecules. F(q), as a fundamental tool in data analysis, generates the pair distribution function (P(r)), equation (**12**), which describes the spatial distribution of scattering centers, like particles, molecules, or domains (Gräwert and Svergun 2020).

$$P(r) = \frac{1}{2\pi^2}\int_0^\infty q^2 I(0)\sin(qr)\,dq$$
(12)

The P(r) function gives essential structural parameters such as the radius of gyration (R_G) and the maximum particle dimension (D_{max}) of the protein. R_G is a measure of the spatial distribution of mass within an object (Okuno and Fratin

56

2014). That function plays a major role in the building of *ab initio* models to illustrate features of the macromolecule's envelope under analysis.

Another definition to consider is the Guinier Law in (**10**). This law considers the scattering patterns at very small scattering angles to also determine R_G. In this data range, multiple scattering is discarded, and a linear approximation is made (Michels et al. 2020).

Finally, there is the Porod Law in (**11**) as well. By also considering the information in high-q values, this function is used to determine the surface and shape of particles in a sample.

Considering the brief description of SAXS and its mathematical background, this context can be used for ClpP studies. This enzyme can be isolated in four different states: disassembled heptameric rings and as tetradecamers in compressed, compact, and extended forms. Some publications show that the states are interchangeable, and the shifts occur under specific conditions, although the mechanisms behind this are not fully elucidated yet. Along those lines, the present technique is intended to extend the understanding of ClpP's overall structure and its transition. For this purpose, a conventional approach was selected: batch-SAXS (Paquete-Ferreira et al. 2023). In this setup, dilutions of purified and dialyzed *Se*ClpP samples are prepared to discard any undesirable effects of high and low concentrations on the measurements, such as aggregation, intermolecular repulsion, and radiation damage. Prior to the experiment, the samples were centrifuged for 60 minutes at 21,000 x g, and then 60 µL of each one were transferred to empty 200-µL PCR tubes to be placed into a block with 32 slots distributed in 4 rows inside the Arinax BioSAXS sample changer (Arinax, France). Besides that, more slots were available for 1.5-mL Eppendorf-like tubes filled with protein-free control buffer for subsequent data subtraction. It is important to note that all the compounds found in the main sample must be in the buffer, too. Otherwise, a mismatch may happen, and the measurements will be compromised for subsequent analysis, considering that even small molecules scatter X-ray in solution. When the protein was incubated with ixazomib, 1% v/v DMSO was added to the control buffer, as this was the final concentration of this solvent in the protein sample.

After the previous procedure, data was collected at P12/EMBL/PETRA III in Hamburg, Germany. The beamline characteristics are the following (Table 11):

Table 11 – P12 beamline features at EMBL/PETRA III.

Source[1]	Petra III U29 undulator
Monochromator[1]	Double crystal Si (111)
Wavelength[1]	0.124 nm
Flux[1]	10^{13} ph/s
Slits[1]	Individually motorized blades of Hybrid Scatterless in a module from Xenocs
Beam size at the detector[1]	0.2 x 0.05 mm^2
Exposure unit[1]	1.7 or 0.9 mm capillary
Temperature[2]	20°C
Exposure time[2]	0.095 s
Transmission[2]	20%
Detector[1]	Pilatus 6M
Sample-detector distance[2]	1.5 m
Sample changer[1]	Arinax BioSAXS (2018 model)

[1] Specifications found at EMBL-BIOSAXS, 2024.

[2] This parameter was defined prior to the measurements. The setup was kept constant in all experiments.

Results from batch-SAXS show aspects of the protein's envelope and, consequently, how parameters like volume, size, R_G, and D_{max} vary under distinct conditions. However, for a better study of protein oligomerization, another technique, size-exclusion chromatography coupled with SAXS (SEC-SAXS), was proven to be more appropriate.

The use of SEC can be significant in avoiding ambiguity in the SAXS measurements analysis and improving data quality. SEC is useful for providing an extra step in the separation of molecules with distinguished MW/volume ratios. In addition to that, chromatography also confirms changes in ClpP's oligomerization that may be induced by ligands or certain physicochemical conditions.

Here, the preliminary sample preparation follows the same procedures as in the previous subsection. Nonetheless, for SEC-SAXS, a running buffer must be taken to the beamline for the equilibration of the column/chromatography system and the sample run. The buffer was comprised of 50 mM Tris base (pH8.0), 100 mM NaCl and 2 mM DTT. It was not supplemented with the ligand ixazomib, as they were not removed from ClpP during SEC, according to initial tests performed with small-scale Superdex 200 increase (10 x 300 mm) (Cytiva, Sweden) and Superose 6

increase (10 x 300 mm) (Cytiva, Sweden) in ÄKTA Purifer 10 system (GE HealthCare, Sweden).

For the measurements at P12, the Superose 6 increase column was chosen. Each run was performed at room temperature (RT) and flow rate of 0.75 mL/min. After SEC, everything eluted from the FPLC system was immediately submitted to SAXS, in the same conditions shown in Table 11, but without the sample changer used for batch-SAXS. Moreover, the sample volume for each automatic injection into the Agilent 1260 Infinity Bio-Inert HPLC/FPLC system (Agilent, USA) was 100 µL, and the protein concentration was 10 mg/mL.

The programs used for data processing are found in the ATSAS 3.2.1 Suite (Manalastas-Cantos et al. 2021). In steps where other computational tools were necessary, the names of each are informed.

Data from both batch-SAXS and SEC-SAXS were initially auto-processed in the beamline's server (P12/EMBL/PETRA II, Hamburg, Germany). Nonetheless, to ensure that any radiation damage/buffer issue interfered with the study of the experimental information, all the images (protein sample and control buffer) were manually visualized. Once this issue was discarded, data processing proceeded. For preliminary data visualization, the program PRIMUS (Manalastas-Cantos et al. 2021) was used. In the case of SEC-SAXS, the program CHROMIXS (Panjkovich and Svergun 2018) is important for the selection of frames of chromatography peaks under analysis and the void where there is only buffer. After this, CHROMIXS proceeded with data subtraction, and the generated graph could also be analyzed on PRIMUS.

When the previous procedure was done, there was a .dat file for each dataset comprising the scattering intensity $I(s)$ over s (nm^{-1}) graph. This file is the basis for all the relevant studies and further quality assessments of SAXS measurements. From this point, the Guinier plot was analyzed (Putnam 2016), where the $I(s)$ vs. s linearity was observed at small angles. As mentioned before, this region is critical for the shape/size determination of the macromolecule, and it also demonstrates the existence of aggregation and any other deleterious intermolecular interactions that may interfere in the data quality. If no issue is detected, the R_G value could be calculated, considering the equation (**10**). The selected data range was the one that resulted in a fidelity value of at least 0.6 or higher.

Subsequently, on PRIMUS, the pair distribution function P(r) showed the means for determining the data range, D_{max}, the alpha value, and the total quality estimation by using the program GNOM (Gräwert and Svergun 2020). The alpha value is particularly important: a high value means a smooth descent of the P(r) function, but also causes difficulties to build the edges of the protein's envelope. Then, that value was kept as low as possible. Considering there is no consensus for a threshold, the one defined for this work was approx. 20.

After checking all the previous parameters and the P(r) function, the .out file was saved and used for posterior low-resolution structure modeling.

The program DAMMIN (Franke and Svergun 2009) was used to build *ab initio* models. For all runs involving native *Se*ClpP, 5 reconstructions were obtained by selecting symmetry P72 and cylinder shape. DAMAVER constructed average models through the processing of the reconstructions. In some cases, GASBOR (Svergun et al. 2001) was also used, if its model indicated further details for structural analysis. To assess the fitting of the calculated I(s) into the experimental I(s) curve (reciprocal space), statistical parameters were evaluated: Anderson-Darling's P-test, *CorMap* P-value, and χ^2 (chi-square) value.

To complement the assessment of protein flexibility and extension/compactness, the dimensionless Porod, Porod-Debye, Kratky-Debye, and SYBILS plots were constructed (Rambo and Tainer 2011), especially for the scrutiny of the effect of the ligand used.

3.7.2. DLS measurements for the analysis of conformational shifts and protein unfolding

Besides SAXS, DLS can also indicate structural shifts, especially if conformational changes with significant R_H variation occur. Then, to confirm whether *Se*ClpP tetradecamers were assembled under the induction of ligands, the present technique was applied as a complementary procedure. The rationale of the present experiment corresponds to the same discussion in subsection 3.6.3.

Measurements were performed with the following samples: native *Se*ClpP, native *Se*ClpP supplemented with 1% (v/v) DMSO, native *Se*ClpP supplemented with glycerol, and *Se*ClpP incubated with 1 mM ixazomib. For the analysis of induced protein extension, tetradecameric *Se*ClpP sample was used. On the other hand, to

observe any oligomerization promoted by the ligand, heptameric *Se*ClpP sample was adopted instead.

All the samples were incubated in a ThermoMixer Comfort (Thermo Fisher Scientific, Germany) at 37°C, for 30 minutes, prior to the experiments. After that, they were centrifuged at 15°C and 21,600 x g, for 1 hour.

For t-ramp experiments, the same setup was used for sample preparation and incubation. Nevertheless, a 20 – 60°C temperature range was set instead of measurements at constant temperature for a time-resolved follow-up of the R_H change and protein stability.

For all the experiments, the same device specifications and software for data processing and analysis discussed in subsection 3.6.3 should be taken into account.

3.8.   Structural analysis of *Se*ClpP: X-ray crystallography

X-ray crystallography is a technique that determines a crystal's atomic and molecular structure. A beam of X-rays is directed to a crystallized sample and diffracted in specific directions due to the regular arrangement of atoms in solid-state. Determining the angles and intensities of these diffracted beams creates a three-dimensional picture of the electron density within the crystal. This information is crucial for the positioning of the atoms, their chemical bonds, and other details.

The starting point for the development of analytic methods in crystallography is the Bragg's law (Humphreys 2013) (Figure 18). This law ($n\lambda = 2d\sin\theta$) associates the wavelength of X-ray (λ) with the interatomic spacing (θ), which allows the atomic organization in a crystal lattice from the observed diffraction pattern. This structural determination comes from strong peaks caused by constructive interference of scattered X-rays in phase. Other relevant information like crystal symmetry and unit cell parameters can be inferred from the Bragg's law as well.
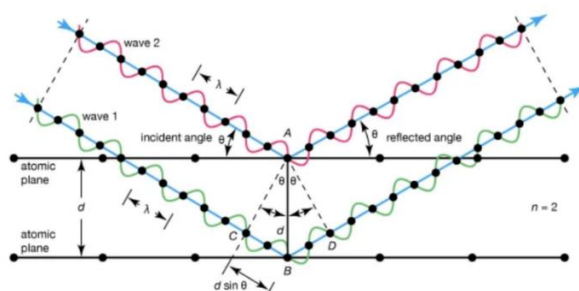
Figure 18 – Illustration of the Bragg's law. Extracted from Britannica, 2024.

Data collection and advances of the Bragg's law led to the building of the electron density map of the crystal by mathematically analyzing the intensities of the diffracted beam, a series of spots on a detector, through Fourier transformations, which convert the reciprocal space back into the real one.

The intensity of each spot in the diffraction pattern relates to the square of the amplitude of the scattered wave, describing the structure factor F(h). F(h) is a complex number that informs about the amplitude and the phase of the scattered wave for a set of crystal planes indexed by the reciprocal lattice vector h. The structure factor is described by the following function (**13**):

$$F(h) = \sum_j f_j e^{2\pi i h . r_j} \tag{13}$$

where

f_j is the scattering factor of the j-th atom

r_j represents the atom position within the unit cell

Additionally, the variation of the electron density, $\rho(r)$, in the unit cell is defined by the inverse Fourier transform of F(h) (**14**):

$$\rho(r) = \frac{1}{V} \sum_h F(h) e^{-2\pi i h r} \tag{14}$$

where

V is the volume of the unit cell

h is the reciprocal lattice vectors represented as (h, k, l)

F(h) are the structure factors

r is the position vector that indicates the point within a unit cell where the electron density is being calculated.

It is essential to consider that the phases of the waves cannot be recovered experimentally, and this fact constitutes what is known as the phase problem. One of the ways to solve this problem is by extracting those parameters from the crystal structure of a homologous macromolecule, or search model, by molecular replacement (MR). This computational method positions the selected model according to the experimental data, splitting the searching procedure into rotation

and translation functions and consequently defining the orientation and location of the structure, respectively. Both functions rely on the Patterson function, which indicates the relative positions of atoms and groups of atoms within the crystal. The Patterson map is determined by the Fourier transform of the squared magnitudes of the observed structure factors and does not consider the phases.

After MR, a first model is available, and the refinement procedure can be initiated. At this moment, chemical and structural information are incorporated to improve the model with the appropriate bond lengths and angles, the reduction of steric clashes, and the consistency of the protein's secondary and tertiary structures according to known biophysical principles.

Other aspects to be considered for structural refinement are anisotropy and disorder. Anisotropy refers to the direction-dependent variability in atomic displacement parameters (ADPs), also called temperature factors or B-factors. This kind of analysis can indicate whether the atoms do not vibrate or move uniformly in all directions, having variable degrees of displacement along the axes. Furthermore, regions of positive peaks in a refined electron density map or difference Fourier map (Fo-Fc) shown below (**15**) demonstrate that ligands, solvent molecules, or parts of amino acid residues could be modelled there. In addition, errors such as misplaced atoms, the modelling of multiple conformations, and partial occupancy can be corrected by analyzing negative peaks.

$$\rho_{diff}(r) = \sum_h (|F_o(h)| - |F_c(h)|)e^{-2\pi i h r} \qquad \textbf{(15)}$$

where

$\rho_{diff}(r)$ is electron density difference at position r.

h is the reciprocal lattice vectors (h, k, l).

$|F_o(h)|$ are the magnitudes of the observed structure factors.

$|F_c(h)|$ are the magnitudes of the calculated structure factors.

$e^{-2\pi i h r}$ is the phase factor obtained from the calculated structure factors.

Other metrics to evaluate the quality of the model fitting into the experimental data are the R_{work} and R_{free}. The first one measures the agreement between the observed diffraction data and the calculated data for the reflections used in the

refinement. To avoid overfitting, the R_{free} measures the agreement for a set of reflections not adopted to refine the model.

The assessment of the stereochemistry helps in the definition of proper values for bond lengths and angles, planarity, and chirality of certain functional groups, backbone, and side chain conformations, assuring geometric accuracy, model reliability, detection and correction of errors, as well as leading to the selection of chemical reasonable structures. In this regard, one of the essential tools is the Ramachandran plot (Carugo and Djinovic-Carugo 2013), which demonstrates if the dihedral angles of the amino acid residues fall into allowed or disallowed regions, based on steric hindrance and favorable interactions.

An unfavorable geometry is also related to rotamer outliers. It is a deviation from the common, energetically adequate conformation of the model under scrutiny.

The processing of all the parameters cited in the last paragraphs is an efficient way to guarantee that the structural interpretation will give useful biophysical data for protein characterization.

For a protein to crystallize, different parameters must be defined through the interpretation of many trials. Generally, values such as pH, temperature, the concentration of salts and precipitant agents are adjusted until crystals are noticed for the first time.

The phase diagram (Figure 19) divided into the undersaturation, metastable, nucleation, labile, and precipitation zones highlights the best setups for crystal growth in relation to the concentration of the protein and the precipitant agent. This agent induces the macromolecule to migrate from the undersaturation to the formation of spontaneous nucleation in specific physicochemical conditions. Once this step is reached, the crystal can grow in the labile and metastable zones, or the system migrates to the precipitation zone. The first zones are ideal, as the presence of nucleation sites and the solute result in the formation of bigger crystals. However, if a high amount of nucleations are present, microcrystals can be generated. For conventional X-ray diffraction with single crystals, a microcrystal may not be proper for a sufficient diffraction intensity, more prone to the effect of radiation damage, producing a low signal-to-noise ratio and limited data completeness.
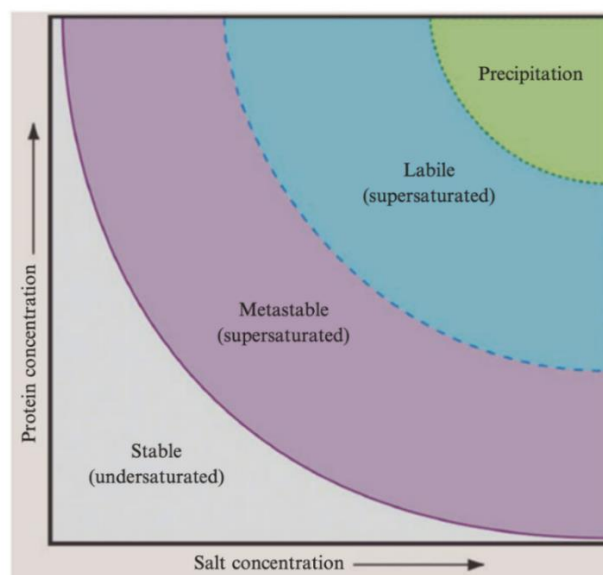
Figure 19 – The phase diagram and its main zones (Wlodawer et al. 2017).

The most common techniques applied for obtaining protein crystals are hanging-drop and sitting-drop. In both configurations, a process of vapor diffusion is triggered by differences in the concentration of the precipitant agent in a droplet containing the biomacromolecule and in a reservoir solution filling a chamber where the droplet is sealed and suspended on a surface of a glass cover (hanging drop), or "sitted" on a surface beside and over the well containing the reservoir solution (sitting drop).

For the crystallization of the native *Se*ClpP, the hanging-drop technique was successful. The setups tested for this purpose are found in Table 12. In all cases, the protein sample and the reservoir solution were mixed at 1:1 ratio. *Se*ClpP concentration was 10 mg/mL for the crystallization of apo protein and ClpP-ligand complex.

The most suitable conditions for getting macrocrystals (bigger than 200 μm) are highlighted in pink, and for microcrystals (around 50 – 60 μm) are delimited in green.

Macrocrystals were harvested and flash-frozen in liquid nitrogen. As the precipitant agent MPD, also a cryoprotectant, was in the mother liquor, the satisfactory vitrification of the crystals was assured, and any "ice ring" was detected during X-ray diffraction under cryoconditions.

With the native tetradecameric *Se*ClpP crystal free from ligand and after soaking with 10 mM ixazomib, diffraction data at various angles were collected at P11 beamline (PETRA III / DESY), in Hamburg, Germany. The crystals of *Se*ClpP bound to glycerol were taken to P13 beamline (EMBL / DESY) after crystallization, in Hamburg, Germany, for data collection.

Once the experimental information was available, the performance of MR started by using homologous structures of *Se*ClpP (PDB ID 3V5E or PDB ID 5C90) as search models. Thus, the initial models were built as single MR solutions with high Top-LLG (Log-Likelihood Gain) and Top-TFZ (Translation Function Z-Score) values. The program adopted for this part was PHASER in the Phenix 1.21.1-5286 Suite (Adams et al. 2010).

The refinement procedure on *phenix.refine* (Afonine et al. 2012) was performed with the standard options and local non-crystallographic symmetry (NCS) (torsion-angle).

After each refinement cycle, manual inspections and corrections were performed on Coot 0.9.8.93 software (Emsley and Cowtan 2004), especially stereochemistry checks associated with clashes, Ramachandran outliers, dihedral angles, bond lengths, and rotamer outliers. Atoms, amino acid residues, or sidechains without a corresponding electron density were removed, and alternative conformations were modeled according to positive peaks (green "blobs") displayed in the difference Fourier map. The negative peaks (red "blobs") in the same map guided the changes in atom positioning or manual occupancy alteration for a subsequent refinement round.

When the refinement statistics demonstrated that the model quality was good enough for the structural studies of the apo *Se*ClpP and its complex with peptidomimetic boronate compound, the last pdb file was submitted to a final check on the Molprobity server (Chen et al. 2010). Without issues, files with the model coordinates and structure factors were validated and deposited on PDB (Young et al. 2017). The PDB entries of the crystal structures are in the table of X-ray diffraction data and refinement statistics of each one of them along the "Result and Discussion" section.

Table 12 – Different setups for the crystallization of *Se*ClpP in its tetradecameric form.

0.1 M NaOAc (pH 4.5) 10 mM CaCl$_2$ 18 % MPD	0.1 M NaOAc (pH 4.5) 10 mM CaCl$_2$ 20 % MPD	0.1 M NaOAc (pH 4.5) 10 mM CaCl$_2$ 25 % MPD	0.1 M NaOAc (pH 4.5) 10 mM CaCl$_2$ 30 % MPD	0.1 M NaOAc (pH 4.5) 10 mM CaCl$_2$ 35 % MPD	0.1 M NaOAc (pH 4.5) 10 mM CaCl$_2$ 40% MPD
0.1 M NaOAc (pH 4.5) 20 mM CaCl$_2$ 18% MPD	0.1 M NaOAc (pH 4.5) 20 mM CaCl$_2$ 20 % MPD	0.1 M NaOAc (pH 4.5) 20 mM CaCl$_2$ 25 % MPD	0.1 M NaOAc (pH 4.5) 20 mM CaCl$_2$ 30 % MPD	0.1 M NaOAc (pH 4.5) 20 mM CaCl$_2$ 35 % MPD	0.1 M NaOAc (pH 4.5) 20 mM CaCl$_2$ 40 % MPD
0.1 M NaOAc (pH 4.5) 30 mM CaCl$_2$ 18 % MPD	0.1 M NaOAc (pH 4.5) 30 mM CaCl$_2$ 20 % MPD	0.1 M NaOAc (pH 4.5) 30 mM CaCl$_2$ 25 % MPD	0.1 M NaOAc (pH 4.5) 30 mM CaCl$_2$ 30 % MPD	0.1 M NaOAc (pH 4.5) 30 mM CaCl$_2$ 35 % MPD	0.1 M NaOAc (pH 4.5) 30 mM CaCl$_2$ 40 % MPD
0.1 M NaOAc (pH 4.5) 40 mM CaCl$_2$ 18 % MPD	0.1 M NaOAc (pH 4.5) 40 mM CaCl$_2$ 20 % MPD	0.1 M NaOAc (pH 4.5) 40 mM CaCl$_2$ 25 % MPD	0.1 M NaOAc (pH 4.5) 40 mM CaCl$_2$ 30 % MPD	0.1 M NaOAc (pH 4.5) 40 mM CaCl$_2$ 35 % MPD	0.1 M NaOAc (pH 4.5) 40 mM CaCl$_2$ 40 % MPD

3.9. Additional biophysical characterizations: differential scanning fluorimetry (nanoDSF) and isothermal titration calorimetry (ITC)

For the evaluation of *Se*ClpP thermal stability and the binding process in the *Se*ClpP-ligand complex, experiments with nanoDSF and ITC were conducted. nanoDSF is a label-free method where the thermal unfolding of a macromolecule is inspected by variations of the intrinsic fluorescence of the tryptophan and tyrosine residues. It is sensitive and precise enough to detect fluorescence emission at specific wavelengths as protein unfolds and the aforementioned residues are in a hydrophobic environment. With nanoDSF measurements, it is possible to evaluate how the peptidomimetic boronate compound influence the proten's thermostability, and if there are more than two species with distinct melting temperatures (T_M) in the sample.

For nanoDSF experiments, samples with 10 µM *Se*ClpP were prepared in replicates with different concentrations of ixazomib, and at least 12 µl of each one was transferred to clear capillaries (NanoTemper, Germany). The measurements were done in a temperature range between 25 and 90 °C. Data collected were automatically processed using the Prometheus NT.48 software (NanoTemper, Germany), and the resulting data were further analyzed using the MoltenProt server (Kotov et al. 2021). Independent measurements with distinct DMSO concentrations and the same amount of ClpP (10µM) were already performed.

ITC measurements, on the other hand, unveil a quantitative and qualitative analysis of the thermodynamics behind the protein-ligand interactions, by measuring the heat released or absorbed. In this experiment, *Se*ClpP concentration is kept constant, and the titrant (ligand) is incrementally injected into the calorimeter cell.

The ITC results used to assess the interaction between *Se*ClpP and ixazomib were collected with the device Auto-iTC200 microcalorimeter (MicroCal-Malvern Panalytical, Malvern, UK). Calorimetric titrations were performed using 800 µM ixazomib and a 10µM *Se*ClpP solutions (buffer containing 50 mM Tris (pH 7.5), 150 mM NaCl and 2 mM DTT). The heat evolved after the injection of ixazomib was calculated from the integral of the measured calorimetric signal. Experiments were performed in replicates, and data were analyzed using Origin 7.0 (OriginLab, USA).

3.10. Peptidolytic assays: degradation of Suc-LY-AMC

The substrate Suc-LY-AMC is a synthetic compound named N-Succinyl-Leu-Tyr-7-amido-4-methylcoumarin commonly used to study ClpP activity, as it is a small oligopeptide capable of entering the enzyme's catalytic chamber, even if its axial pores are closed. The N-succinyl group is attached to the N-terminal, providing stability, increasing the solubility, and influencing the specificity of the ClpP for the substrate. The amino acids leucine (L) and tyrosine (Y) are crucial for substrate recognition by proteases, and the last portion, 7-amido-4-methylcoumarin (AMC) is a fluorescent leaving group linked to the C-terminus of the peptide. When the enzymatic deconstruction of Suc-LY-AMC starts, AMC is released, and a fluorescent signal is detected.

*Se*ClpP in buffer composed by 50 mM Tris base (pH 7.5), 150 mM NaCl, and 2 mM DTT (Buffer A); or 50 mM Tris base (pH 7.5), 150 mM NaCl, and 10% w/v glycerol (Buffer B) was used for peptidolytic assays in TECAN Infinite M Flex plate reader (TECAN, Austria). This device is equipped with a detector capable of quantifying variations of the fluorescence intensity caused by the AMC release in the reaction mixture.

Buffer B was used to observe if glycerol affects the ClpP function somehow, since this triol is a common chemical chaperone (Welch and Brown 1996) that improves protein stability. The protein was in its tetradecameric form in both buffers.

The quantities of protein and substrate, as well as the physicochemical conditions for the assays, were defined according to previous experiments described in the "Results and Discussion" section.

In order to compare results obtained from reactions with apo *Se*ClpP and *Se*ClpP-ligand complex, graphs with relative activity in % were explored. All the values of the initial velocity (V_0) were normalized with the V_0 calculated from control (samples free from ligand).

3.11. Proteolytic assays: degradation of β-casein from bovine milk

Aiming to observe the degradation of β-casein by *Se*ClpP bound to peptidomimetic compounds, 10 µM of the protein were incubated with three different ixazomib concentrations: 200 µM, 500 µM, and 1000 µM. The substrate at 60 µM was also added to the reaction mixture in a 1.5-mL Eppendorf-like tube, and the resulting samples were incubated in a ThermoMixer Comfort (Thermo Fisher Scientific, Germany) at 37°C and under stirring at 800 rpm. During specific time intervals, one

tube was removed, and its content was heated at 95°C to submit the protein to 15% SDS-PAGE in denaturing conditions. A control without the ligand under analysis was prepared for each experiment, proving that no proteolytic activity could be detected with the apo protein.

In order to compare the degradation induced by ixazomib to one promoted by a canonical ClpP activator, the compound ONC206 was also added to the present experiment.

The result was qualitatively interpreted based on the casein's band fading and the consequent formation of bands associated with the degradation products in a time-resolved fashion. An unstained protein market (Thermo Fisher Scientific, Germany) was added to gel for molecular weight (MW) estimation.
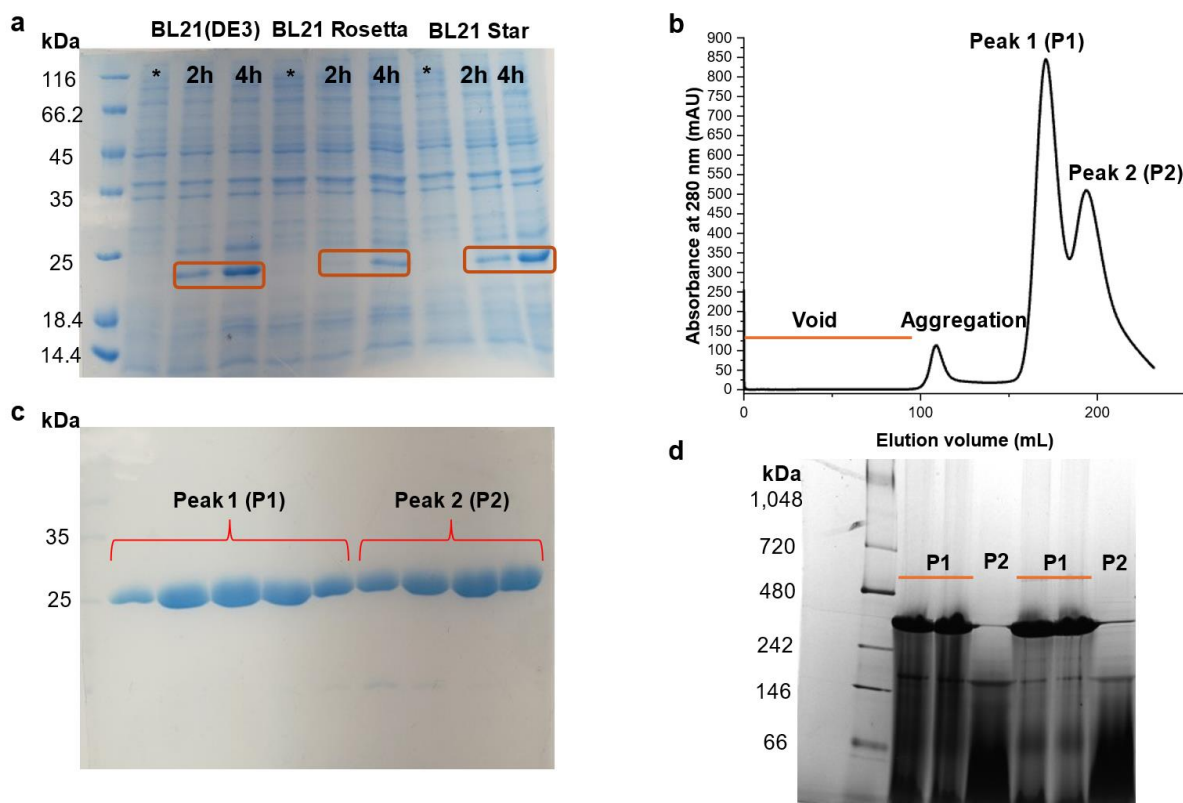
4. Results and Discussion

4.1. Insights into structural and functional aspects of native *Se*ClpP

For the determination of the best conditions to express *Se*ClpP, three engineered *E. coli* strains, BL21(DE3), BL21 Rosetta (DE3), and BL21 Star (DE3) were used for small-scaled trials in 250-mL flasks with 50 mL LB medium. The tests with 0.5 mM IPTG and 50 μg/mL kanamycin took up to 4 hours, at 20°C and 180 rpm, and in Figure 20a, the SDS-PAGE result confirms successful expression by all the strains. However, as it is well established in the literature that BL21 Star (DE3) provides higher amounts of non-toxic proteins such as ClpP, this system was chosen for the scaling-up process in a 5L flask containing 1 liter of LB medium. In this case, the IPTG/kanamycin concentration and temperature/stirring parameters were the same as in the tests performed in small flasks. Using this setup, the obtained yield was approx. 267 g of macromolecules per 1 L of culture.

The procedures of cell lysis and purification led to a final SEC chromatogram composed of two prominent peaks: one starting at 150 mL and the other at 175 mL (Figure 20b), which were named peak 1 (P1) and peak 2 (P2), respectively. By collecting fractions of P1 and P2 and submitting them to SDS-PAGE, bands displayed in the gel image are located at similar heights (approx. 25 kDa), an indication that *Se*ClpP is isolated as two distinct oligomers (Figure 20c). Along these lines, some publications have already demonstrated that ClpP's oligomerization, or the presence of different oligomeric states, is influenced by conditions like single-point mutations (Kang et al. 2004), the sample buffer of choice (Gersch et al. 2015), or even protein concentration.

To identify the molecular weight/oligomerization of the species isolated in P1 and P2, an experimental technique that did not expose the macromolecules to denaturing conditions was needed. In this regard, native-PAGE was performed, and in Figure 20d, the most prominent P1 band is found between 480 and 242 kDa, and the P2 band is positioned between 242 and 146 kDa. Based on this result, there is strong evidence that *Se*ClpP is found as tetradecamers (300 kDa) and heptamers (150 kDa).

Figure 20 – Expression and purification of *Se*ClpP. (**a**) 15% SDS-PAGE after expression tests with three *E. coli* expression systems: BL21(DE3), BL21 Rosetta, and BL21 Star. Note that the control sample, the one without IPTG, is marked with an asterisk. Control was removed after 4h to prove there was no band in the control lanes at around 25 kDa, the region where ClpP is expected to be seen. (**b**) SEC chromatogram after the last purification step of *Se*ClpP with the preparative column HiLoad 26/600 Superdex 200 pg. The presence of two main peaks, P1 and P2, is observed at this stage. (**c**) 15% SDS-PAGE with fractions from P1 and P2. (**d**) Native-PAGE after pooling the fractions from P1 and P2.

SEC-SAXS measurements also make available insights into the oligomerization of ClpP. Even using a small analytical SEC column (Superdex 200 Increase 10/300), the chromatogram profile in Figure 21a is similar to the one presented in Figure 20a. For the analysis, frames from both peaks were selected, and the buffer contribution to the X-ray scattering was subtracted. This process resulted in two curves of X-ray scattering intensities (Figure 21b). From these curves, the Guinier plots (Figures 21c and 21d), P(r) functions (Figure 21e), and the Kratky Plots (Figure 21f) were defined, and the R_G and D_{max} could be calculated as well.
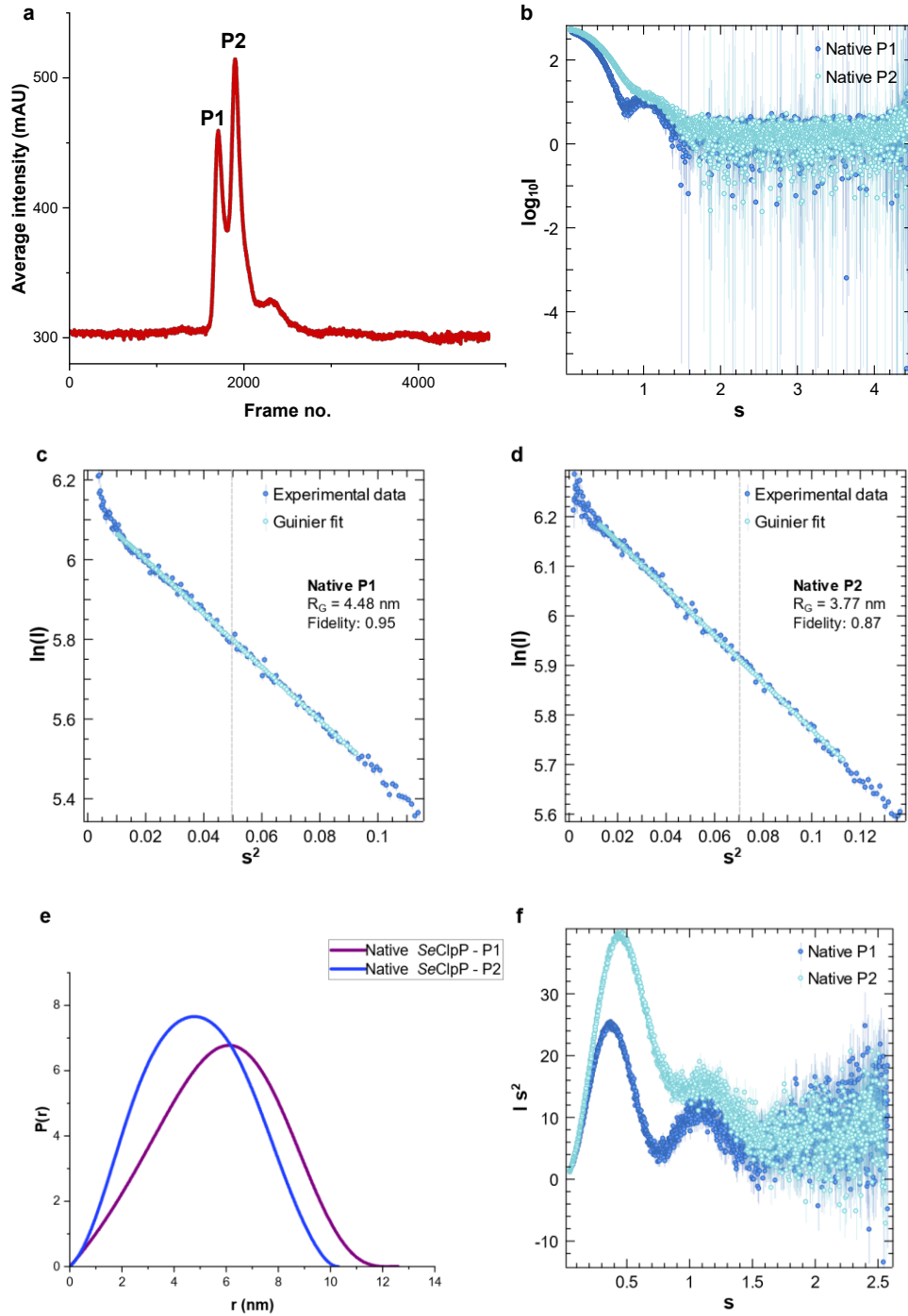
Figure 21 – Main graphs obtained from SAXS measurements with native *Se*ClpP. (**a**) SEC chromatogram confirms the presence of two main species: P1 and P2. (**b**) X-ray scattering intensities were measured from P1 (dark blue curve) and P2 (light blue curve) samples. Moreover, (**c**) and (**d**) represent Guinier fits, the calculation of R_G, and the fidelity values within the validity range $0 < sR_G < 1.3$. (**e**) P(r) functions of P1 (purple curve) and P2 (blue curve). (**f**) Kratky plot for P1 and P2 demonstrates the complete folding of both species. **s** in 1/nm.

Table 13 meticulously enlists all the previous parameters, as well as other relevant ones extracted from SAXS data, providing a comprehensive overview of the measurements.

Table 13 – Parameters calculated from SEC-SAXS measurements.

	Native *Se*ClpP – P1	Native *Se*ClpP – P2
Data collection parameters X-ray source Wavelength (nm) Detector distance (m) Temperature (K)	PETRA III, EMBL'S P12 beamline	
I(0) (P(r) function)	1011.00	553.00±0.24
I(0) (Guinier/AutoR$_G$)	1018.21±0.91	553.00±0.76
I(0) (SAXSMoW[1])	1015.57	412.40
R$_G$ (nm) (P(r) function)	4.38±0.002	3.78±0.008
R$_G$ (nm) (Guinier / AutoR$_G$)	4.48±0.006	3.77±0.003
R$_G$ (nm) (SAXSMoW[1])	4.46	3.73
qR$_G$ limit (Guinier/AutoR$_G$)	1.30	1.34
qR$_G$ limit (SAXSMoW[1])	1.29	1.30
D$_{max}$ (nm) (P(r) function)	12.91	10.58
Estimated porod volume (Å^3)	392108	186890
χ^2 value [2]	1.00	1.00
CorMap P-value [3]	0.37	0.45
Anderson-Darling test's P-value [4]	0.88	1.00
Molecular mass (SAXSMoW[1])	288.53	135.00
Molecular mass (sequence)	299.15	149.57
Oligomeric state	Tetradecamer	Heptamer

[1] Values calculated on SAXSMoW server (Piiadov et al. 2019).

[2] Statistical measure to determine whether an observed data fits an expected distribution.

[3] Goodness-of-fit test to assess discrepancies between one-dimensional spectra emerging from X-ray scattering experiments (Franke et al. 2015).

[4] Statistical test that compares the fit of an observed cumulative distribution function to an expected cumulative distribution function (MacKenzie 2013).

The previous SAXS graphs and table help to interpret further the characteristics of P1 and P2 in the solution. The broader aspect of the P(r) curve of native P1 confirms its higher oligomerization degree with higher I(0) and R_G values. I(0), the intensity of scattered X-rays at zero scattering angle, is more prominent for P1 because of its higher electron count and contrast factor. Besides that, since native P2 is a smaller structure, its P(r) curve has a smaller D_{max} than the one representing P1. By definition, D_{max} is the maximum distance between any two points within a particle (Nirschl and Guo 2018).

In both cases, a pair of peaks in the Kratky plot (Figure 21f) describes multimeric structures. The discrepancy between the heights of the first peaks provides some detailed information: the scattering intensity from P1 sample is spread over a more extensive range of s values, making its peak smaller. This aspect demonstrates that P1 is bigger than P2. The P2 peak results from higher scattering promoted by smaller particles with uniform density and a well-defined shape at high s values.

The program DAMMIN built the *ab initio* models of P1 and P2. This modeling allows the reconstitution of the protein envelope at low resolution with shape and size details extracted from the P(r) function. In Figure 22, the representations are an average of five reconstructions of P1 and P2 with good statistics (χ^2 value, Anderson-Darling test, and *CorMap* test), as observed in Appendix, Figures A6.1/Tables A6.1 (P1), and Figures A6.2/Tables A6.2 (P2). The statistical parameters confirmed as correct the assumptions of P72 symmetry with prolate anisometry for P1 and P7 symmetry for P2. In Figure 22a, the tetradecameric state is depicted as barrel-like in a low-resolution model with dummy atoms (DAMs), and the heptamer consists of only one ring, as seen in Figure 22b.

Complementing the previous DAMs, other models were built using dummy residues on GASBOR, and they highlight some details: the tetradecamer contains two axial pores with a diameter of approx. 9 Å (Figure 22c), characteristic of the closed ClpP (Yu and Houry 2007). Conversely, in the heptamer, the unique pore is slightly bigger: approx.13 Å (Figure 22d).

The GASBOR variant, GASBORI, constructs a model in the reciprocal space, by fitting the theoretical I(s) scattering curve into the experimental I(s) scattering curve. The quality assessment of GASBOR is presented in Figure 23 and Table 14.
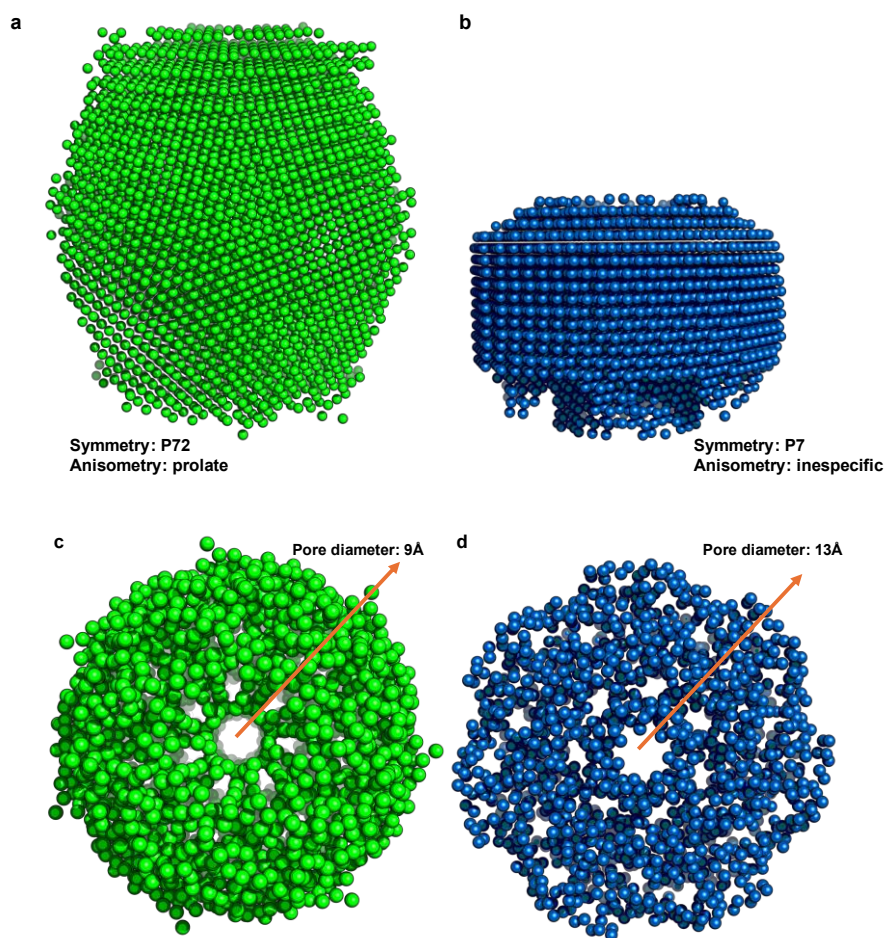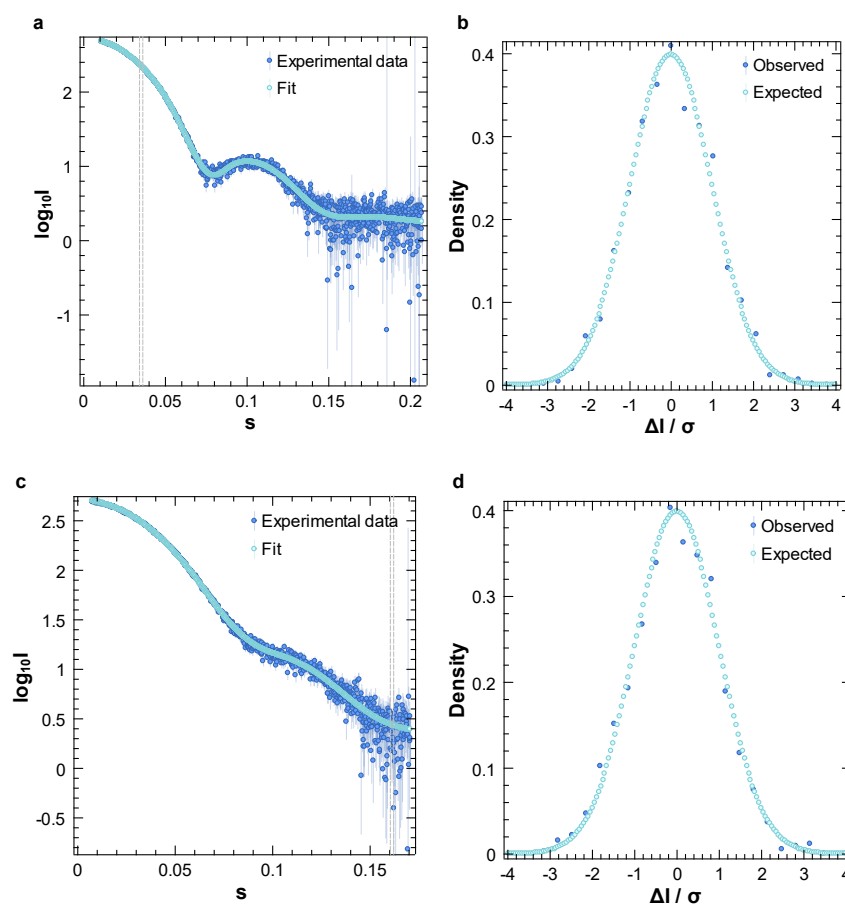
Figure 22 – *ab initio* representations of native *Se*ClpP. The models confirm the oligomeric state of the protein samples P1 and P2: tetradecamer and heptamer, respectively. (**a**) DAM of the 14-mer structure and (**b**) DAM of the 7-mer structure. Both were constructed by DAMMIN/ATSAS suite with a collection of densely packed beads within a search volume. (**c**) Model of the 14-mer and (**d**) 7-mer structures obtained by GASBOR/ATSAS suite. This program uses the concept of dummy residues corresponding to amino acids in the protein chain.

Table 14 – Statistics of *ab initio* modeling with GASBOR.

	Native *Se*ClpP – P1	Native *Se*ClpP – P2
Program[1]	GASBORI (command line)	GASBORI (command line)
χ^2 value	1.02	1.04
CorMap P-value	0.13	0.19
Anderson-Darling's P-test	0.68	0.44

[1] Offline program available on ATSAS 3.2.1 suite (Manalastas-Cantos et al. 2021).

Figure 23 – Quality assessment of how well the theoretical curve (light blue) calculated from GASBOR models fits the experimental data (dark blue). (**a**) Scattering intensity in logarithmic scale ($\log_{10}I$) *vs.* the scattering magnitude (**s** as 1/nm), and (**b**) normalized residual plot for P1 sample. Likewise, for P2 sample, (**c**) the graph scattering intensity in logarithmic scale *vs.* the scattering magnitude (**s** as 1/nm) and the (**d**) normalized residual plot. In (**c**) and (**d**), the electron density is well distributed along $\Delta I/\sigma$ within ±3, not informing systematic errors or model inadequacies. $\Delta I/\sigma$ is dimensionless.

For further characterization of the 14-mer *Se*ClpP at an atomic level, after the last purification step, P1 fractions were pooled and concentrated to 10 mg/mL for subsequent crystallization trials. The focus on P1 here is justified because it is the only active oligomer. To check the degree of monodispersity of the resulting sample, it was centrifuged at high speed and submitted to DLS measurements. The radius distribution and radius plots in Figures 24a and 24b, respectively, do not present any impurities or aggregations that could be deleterious to the crystal formation. The calculated hydrodynamic for the protein radius is 5.40 nm.

Using variations of a crystallization setup for ClpP from *Staphylococcus aureus* (*Sa*) composed of NaOAc, MPD, and $CaCl_2$ (Gersch et al. 2012), Table 12, in the "Material and Methods" section, was defined to attempt crystallizing *Se*ClpP. The precipitant agent MPD is commonly applied in protein crystallography and offers the advantage of being a cryoprotectant. This kind of compound exerts a crucial role in preserving the integrity of crystals during the cooling process with liquid nitrogen (Vera and Stura 2014). Furthermore, this protection avoids the formation of a pathology known as "ice ring" that compromises data quality and frequently causes resolution loss (Parkhurst et al. 2017).

After 20 minutes, microcrystals could be seen, and in two days, bigger needle-like crystals (Figure 24c) were collected and flash-frozen for X-ray diffraction (Figure 24d). Data were obtained at the highest resolution of 1.9 Å and the reflection file (.mtz) was generated by the software XDSAPP (Krug et al. 2012). Quality check by *phenix.xtriage* did not retrieve any issue or pathology.
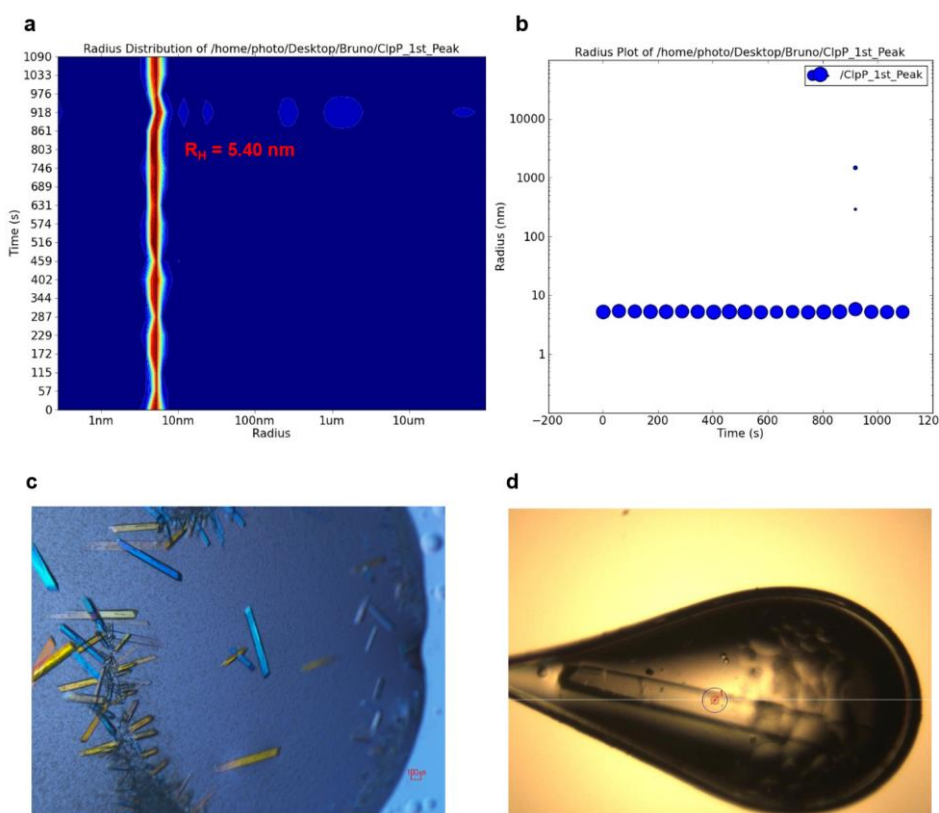

Figure 24 – Steps prior to X-ray diffraction: (**a**) Radius distribution and (**b**) radius plots to evaluate the sample monodispersity. (**c**) Needle-like crystals in a droplet inside a Linbro-like plate (vapor diffusion, hanging-drop technique) and (**d**) Single native *Se*ClpP crystals prior to X-ray diffraction at different angles.

After solving the phase problem with the 14-mer *Sa*ClpP as the search model (PDB ID: 5C90; homology: 97.95%) by molecular replacement (MR), only one solution with high Top-LLG and Top-FTZ values was obtained. Those are metrics to assure the statistical confidence and success of the result.

The "Material and methods" section describes the refinement protocol. Figures 25a -25c depict the final crystal structure in several ways. Table 15 has details about data collection and statistics.

Calculation of Matthews probability with the help of the Matthews tool/CCP4 (Morgan et al. 2015) has shown that 14 subunits are in the asymmetric unit (ASU), a region of space in a crystal that contains all the information to describe its structure (Xu and Dunbrack 2019), and a Matthews coefficient of 2.50 Å^3/Da. The assembly's global symmetry is D7-dihedral, its molecular mass is 3129569.28 u, and its surface area accessible to solvent is 1048576 Å^2. The latter parameters were calculated by PyMOL.
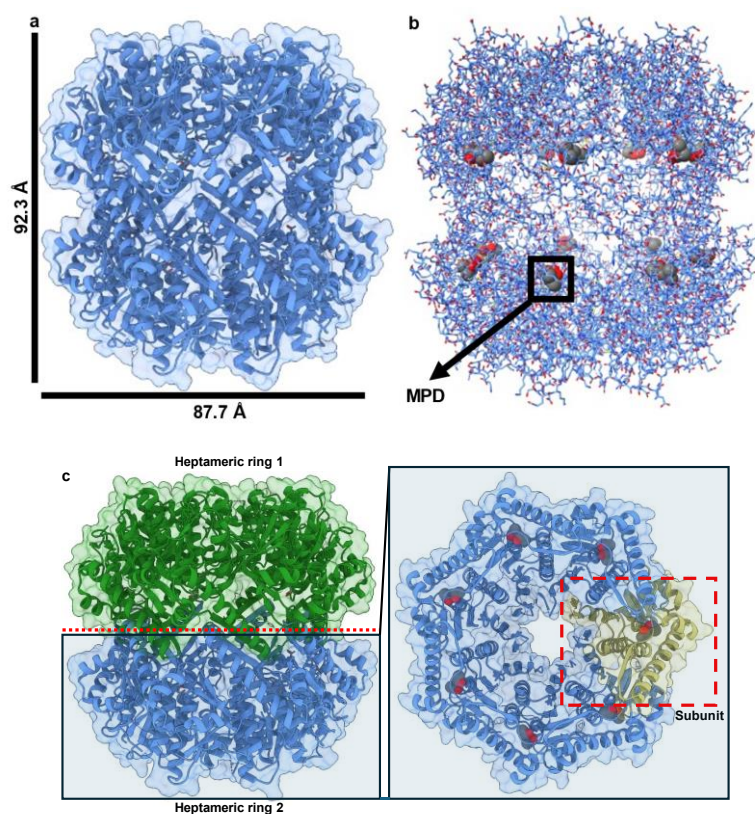
Figure 25 – Overview of the crystal structure of native *Se*ClpP – P1 (14-mer). (**a**) Front view of the barrel-like structure. (**b**) Another illustration where 14 molecules of MPD, the precipitating agent, are found in each of the protein's catalytic sites. (**c**) Two-color scheme of the stacked heptameric rings forming the tetradecamer. An internal view of a heptamer with 7 MPD molecules and a subunit in yellow.

Table 15 – X-ray diffraction data and refinement statistics (native P1 oligomer).

Native *Se*ClpP - P1	
Data collection	
X-ray source	P11, PETRA III, DESY
Detector	Pilatus 6M
Space group	P 2_1
Cell dimensions	
a, b, c (Å)	95.42, 123.66, 126.79
Wavelength (Å)	1.03
Resolution (Å)	48.21 – 1.90 (1.94 – 1.90)
Total reflections	1613744 (87103)
Total unique reflections	456211 (25528)
Redundancy	3.5 (3.4)
Wilson B-factor (Å^2)	27.83
R_{meas}	0.17 (1.01)
$CC_{1/2}$	0.98 (0.68)
V_M (Å^3/Da)	2.5
I/σI	4.72 (0.58)
Completeness (%)	98.59 (96.16)
Refinement	
Reflections used	228269 (13047)
Reflections used for R_{free}	2396 (137)
R_{work}	0.18 (0.25)
R_{free}	0.22 (0.29)
No. of atoms	
protein	19446
ligand	112
water	1641
Average *B*-factor (Å^2)	31.38
macromolecules	30.88
ligands	34.04
water	37.09
R.m.s deviations	
bond lengths (Å)	0.008
bond angles (°)	0.96
Ramachandran	
favored (%)	98.46
allowed (%)	1.54
outliers (%)	0.00
PDB ID	8CJ4

Values in parentheses refer to the last shell.

The compartmentalized analysis of the apo crystal structure reveals essential observations. Firstly, the axial pores seem more extended than expected (Figure
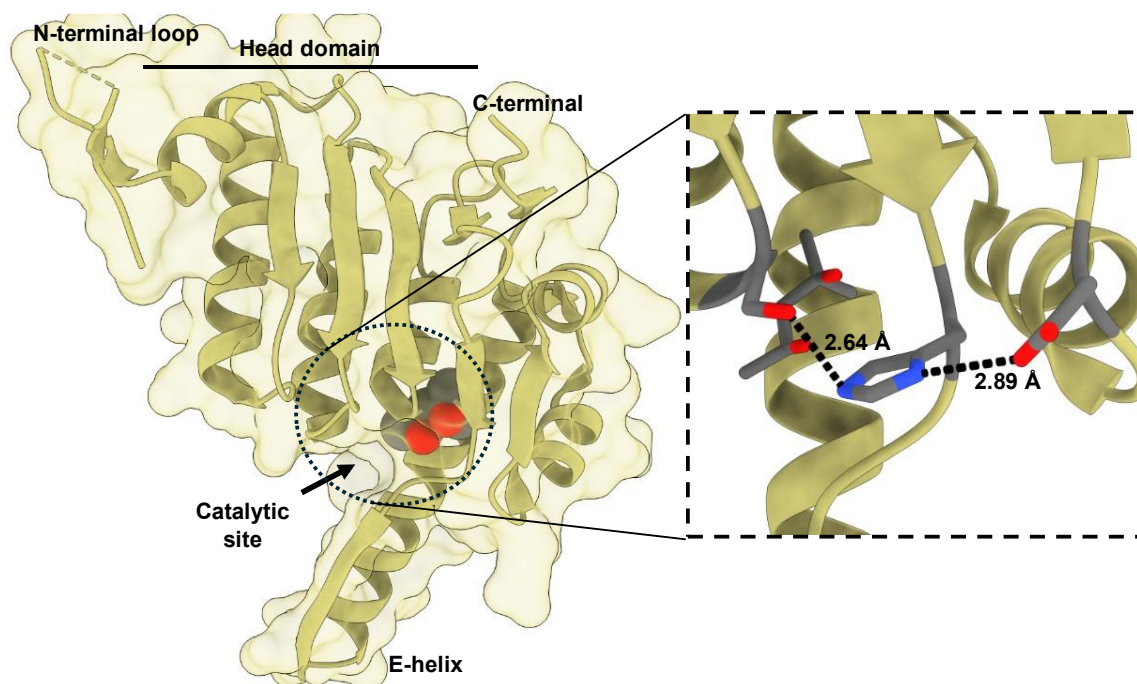
26a). Because of the high flexibility of the N-terminal loops that enclose this area, the electron density of some of their amino acid residues is missing, and therefore they were not modeled. This aspect is also noticed in many other PDB entries related to ClpP and obtained from crystals grown in distinct conditions. Then, SAXS data assists this work in making conclusions about the gating mechanism of *Se*ClpP, and the GASBOR model of the apo protein is demonstrated again in Figure 26b for comparison.
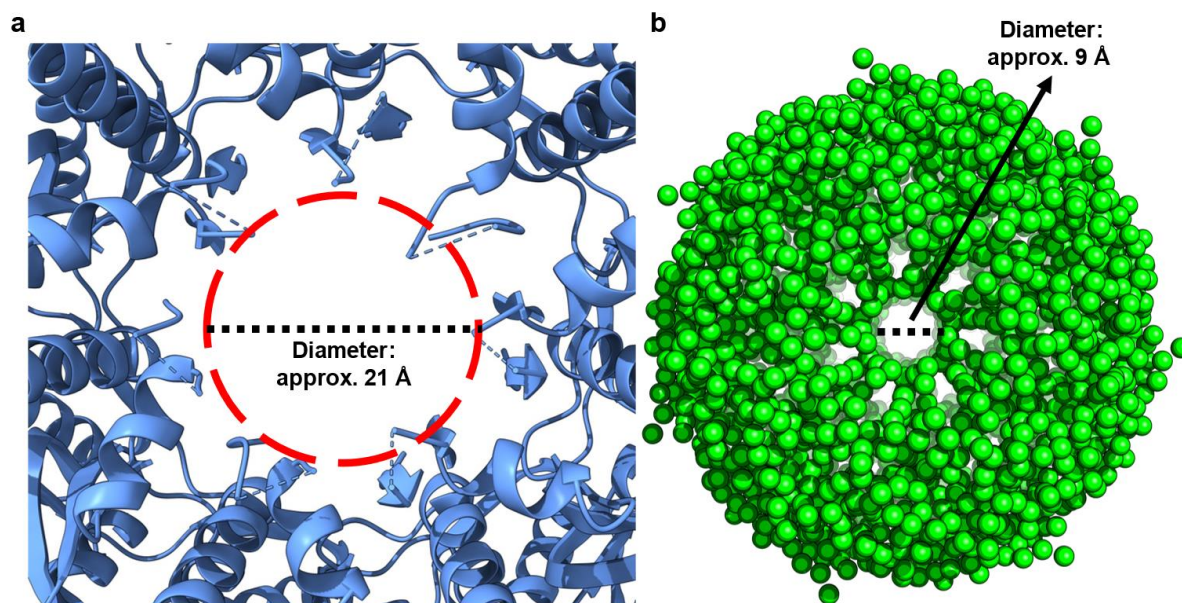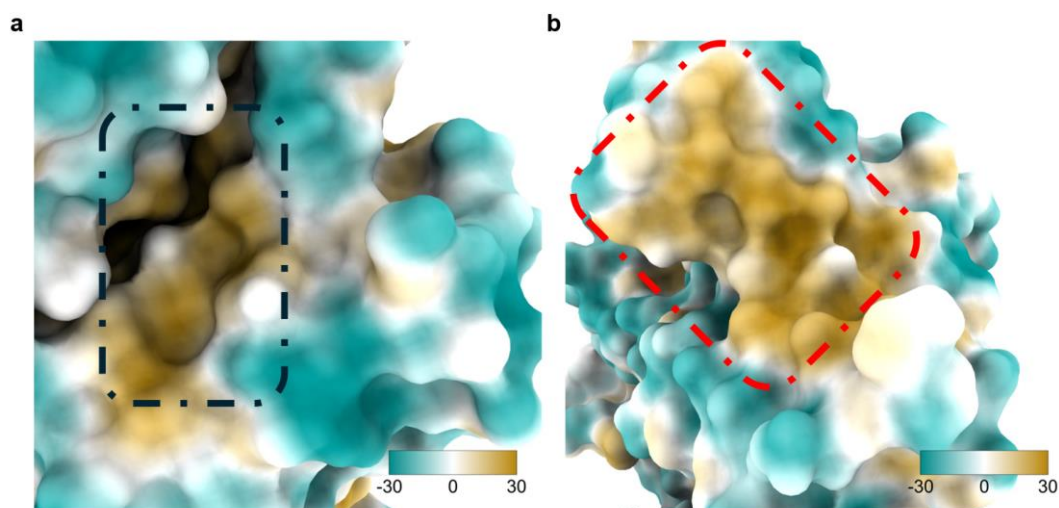

Figure 26 – One axial pore, two representations. (**a**) Given the flexibility of the loops that constitute the ClpP's gating mechanism, they could not be wholly resolved by using X-ray diffraction data. Then, the pore looks larger than it really is. Nevertheless, in (**b**), a low-resolution *ab initio* model, even without a view at an atomic level, demonstrates the actual dimension of the same region. The diameter, in both cases, is represented by approximate values defined with PyMOL.

A complete *Se*ClpP subunit is composed of the following conserved parts: the compact and globular body of the monomer (head domain), the N-terminal region (gating mechanism and substrate translocation), the active site, and the handle region (Figure 27). The allosteric sites, or "hydrophobic pockets," are delineated from the hydrophobic interactions between two vicinal monomers, as seen in Figure 28a. In Figure 28b, the lipophilic aspect of the region is presented with two adjacent subunits, while the profile of the entire protein is shown in Figure 29.
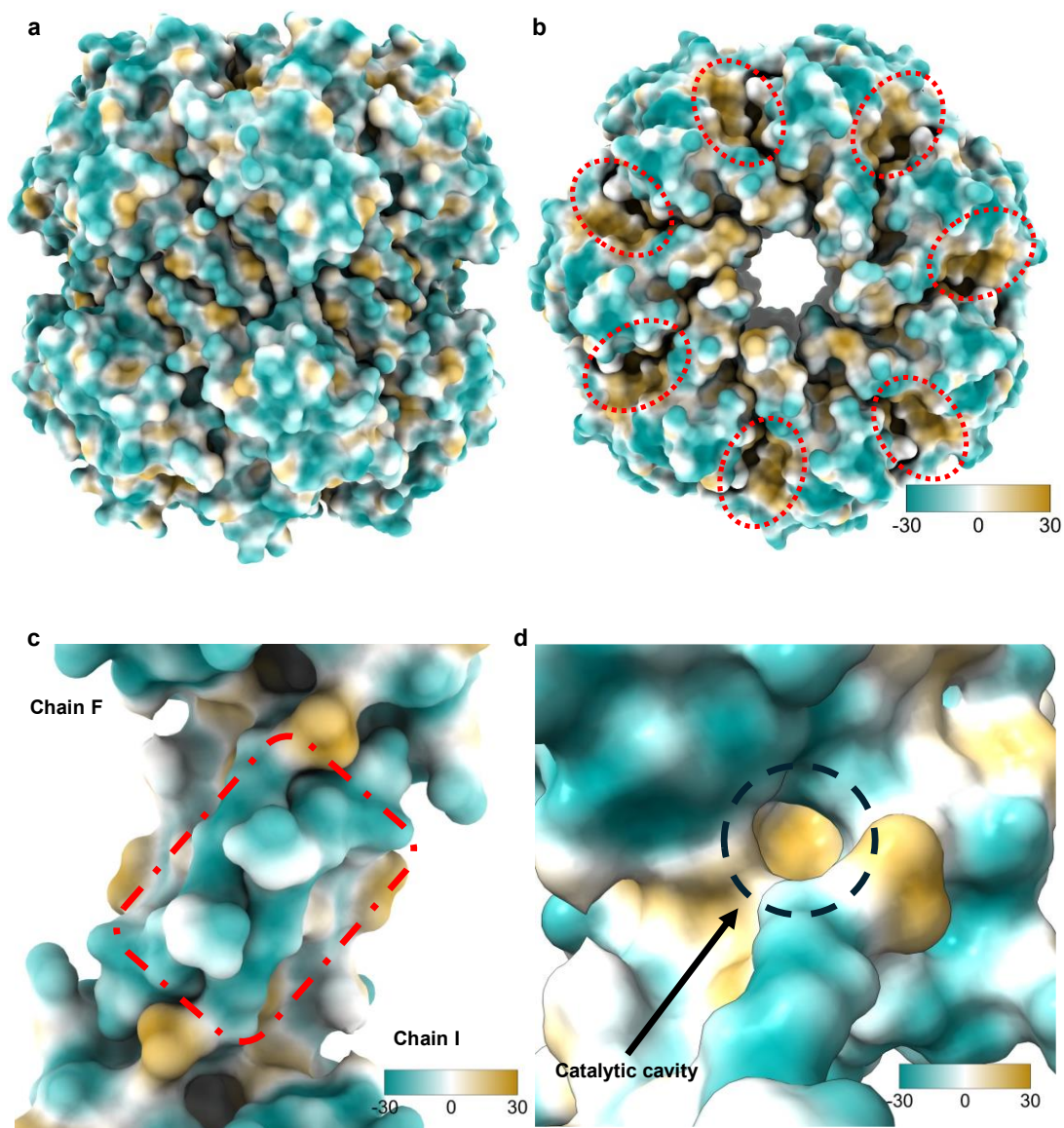
Figure 27 – General view of a *Se*ClpP subunit with its main constituent parts: partial N-terminal loop (gating mechanism), head domain, E-helix region (connection between the opposing rings), catalytic site with a MPD molecule, and C-terminal portion. Zoomed-in depiction of the catalytic site with the Ser98-His123-Asp142 triad: the alignment of those residues with the formation of hydrogen bonds (black dashed lines) makes the protein active for hydrolysis.


Figure 28 – Lipophilicity profile of the contact region between two vicinal subunits. (**a**) An example of a "hydrophobic pocket" is delimited by a black dashed rectangle. (**b**) In one *Se*ClpP subunit, the contact zone responsible for forming the allosteric site is shown inside a red dashed rectangle. According to the scale, blue areas are more hydrophilic, and brownish portions are more hydrophobic.

Figure 29 – Overall lipophilic profile of *Se*ClpP. As seen in (**a**), the external area of the head domain of each monomer is predominantly hydrophilic. At the same time, in (**b**), the allosteric sites (red dashed circles) and the portion surrounding the axial pore are more lipophilic, unveiling that hydrophobic interactions constitute the controlling mechanism of the pore geometry. (**c**) Hydrophilic zone of interactions between gly-rich regions protruding from monomers in opposing rings, and (**d**) catalytic cavity with a hydrophobicity around 0.70, according to the GeoMine server (Diedrich et al. 2024).

The equatorial region of *Se*ClpP is essential for the protein's state and the alignment of the catalytic triads. In Figure 30, the network of hydrogen bonds between two opposing subunits is depicted. Those interactions confer stability to

the entire tetradecameric state and keep the geometry of the catalytic sites proper for receiving the substrate for posterior deconstruction by hydrolysis.
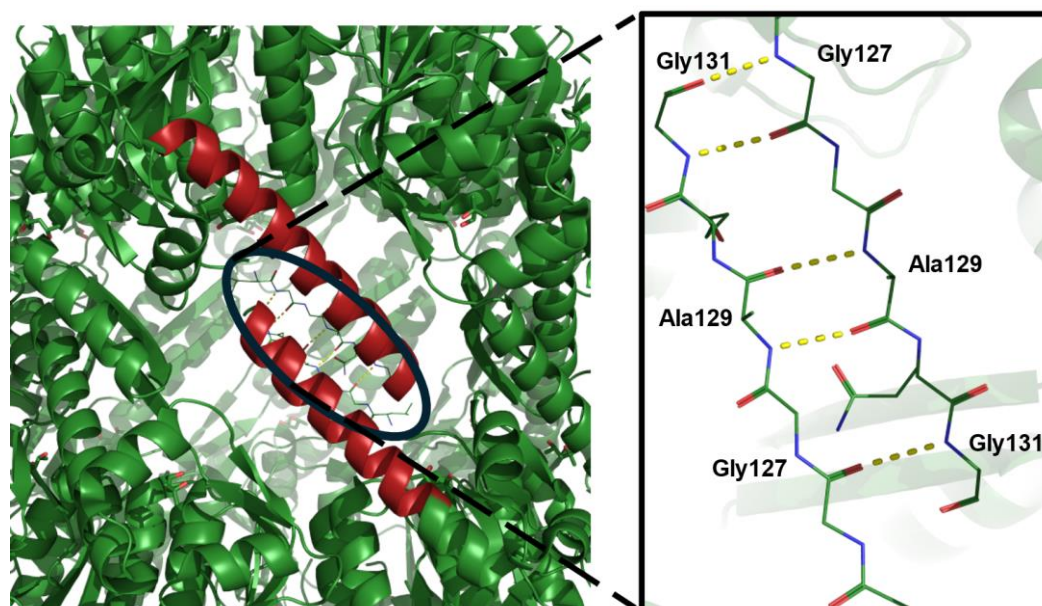
Figure 30 – Detailed depiction of the connection between two monomers from opposing subunits. E-helices are in red, and sticks represent the amino acid residues in the gly-rich regions. The hydrogen bonds, as yellow dashed lines, have lengths of approx. 2.8 – 3.0 Å and form an ordered secondary structure of antiparallel beta-sheets that support stability to a functional ClpP.

The primary features of native *Se*ClpP described hitherto are relevant to the upcoming study of the structural and functional characteristics of the *Se*ClpP-ligand complex.

4.2.   Sample preparation for structural studies on *Se*ClpP-ligand complex

E. coli has a native ClpP (*Ec*ClpP) with considerable peptidolytic activity. Then, to confirm that there was no contamination of the sample by the homologous ClpP from the expression system, a simple test was performed prior to the further experimental steps with the ligand of interest: enzymatic assays with Suc-LY-AMC, keeping in mind that this substrate is small enough to diffuse through the closed ClpP pores and access the catalytic sites. The control used here was the inactive *Se*ClpP mutant, obtained from the replacement of the active Ser98 by Ala98. The graph in Figure 31 proves that no peptidolysis is detected in the assay with *Se*ClpP S98A. Thus, no *Ec*ClpP is present after the purification steps. Moreover, the data also demonstrate that the native *Se*ClpP is isolated in its active form without adding

any chaperone or modulator, differing from human ClpP (*Hs*ClpP) (Kang et al. 2005) and some ClpPs from gram-negative bacteria (Akopian et al. 2012).
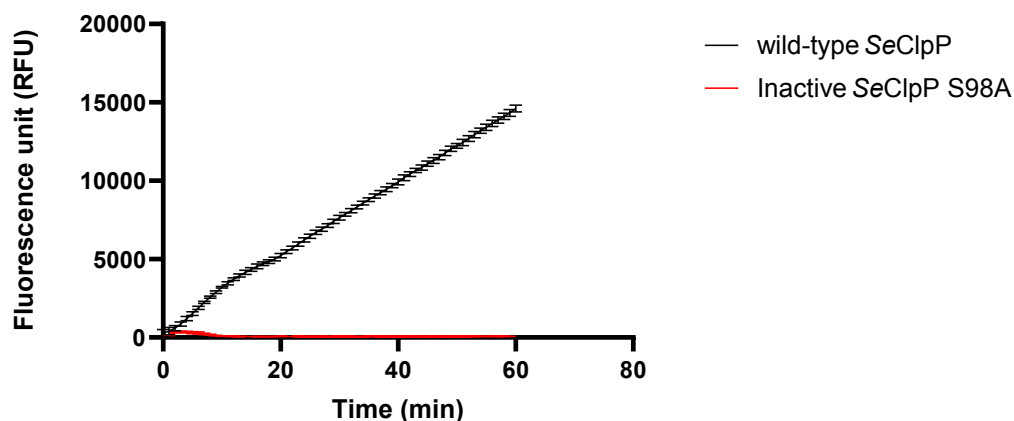
Figure 31 – Peptidolytic assays with the fluorogenic substrate Suc-LY-AMC, the inactive mutant *Se*ClpP S98A (red curve), and wild-type *Se*ClpP (black curve).

The wild-type *Se*ClpP and *Se*ClpP S98A mutant were expressed and purified by applying the same protocols. If there were contamination with *Ec*ClpP, assays with the mutant would necessarily display some peptidolytic activity, at least.

Following the initial analysis with the apo protein, biophysical and biochemical experiments were planned and performed to characterize the *Se*ClpP-ligand complex. The first part comprises data related to the protein complexed with the boron-based compound ixazomib. As DMSO is required to fully solubilize the drug used here, nanoDSF, SAXS, and DLS measurements assessed how this organic solvent affects the structure and stability of the *Se*ClpP, avoiding any eventual issues that may come from the use of this solvent. From nanoDSF, considering the range of DMSO concentration between 1% v/v and 14% v/v, the variation of melting temperature (T_M) is not so pronounced. But certainly, an amount up to 2% v/v DMSO would assure a condition closer to the sample free from that solvent, in line with the graph in Figure 32.
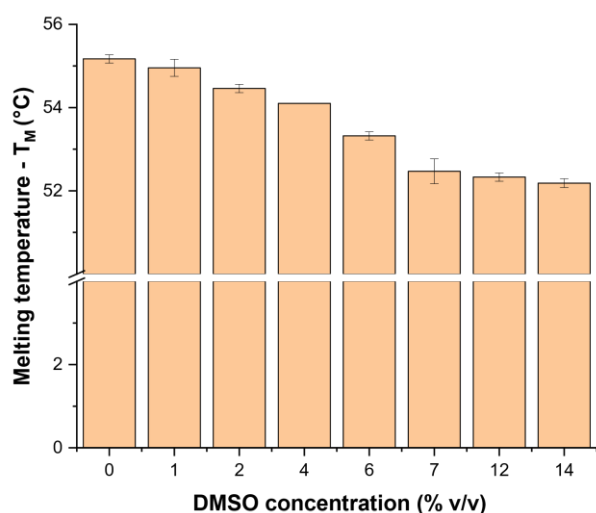
Figure 32 – Effect of DMSO on melting temperature (T_M) obtained from nanoDSF measurements.

Nevertheless, there was an attempt to reduce the solvent amount as much as possible, mainly because of the sensitivity of SAXS measurements. After preparing different dilutions with the ligands of interest, it was noticeable that they were stable in solution with 1% v/v DMSO.

In the same way, SAXS data proves whether 1% v/v DMSO induces structural changes that could be detected. The Porod-Debye, Kratky-Debye, and SIBLYS plots do not display any significant conformational alteration promoted by DMSO (Figure 33).

The Kratky-Debye, Porod-Debye, and SYBILS plots are relevant for qualitatively evaluating protein flexibility and conformation (Brosey and Tainer 2019). The Kratky-Debye presents the variation of the scattering intensity (I(q)) with the scattering vector (q), displaying $q^2.(q)$ on the y-axis versus q on the x-axis. In addition, the Porod-Debye ($I(q).q^4$ *vs* q^4) indicates alterations in the surface-to-volume ratio (Rambo and Tainer 2011), and SIBLYS ($I(q).q^3$ *vs* q^3) is sensitive to overall shape and flexibility (Hura et al. 2009). In all three graph variants, the mathematical transformation makes it possible to recover structural features inaccessible directly from the raw scattering curve. They are also dimensionless, allowing the comparative analysis of proteins regardless of concentration (Receveur-Brechot and Durand 2012).
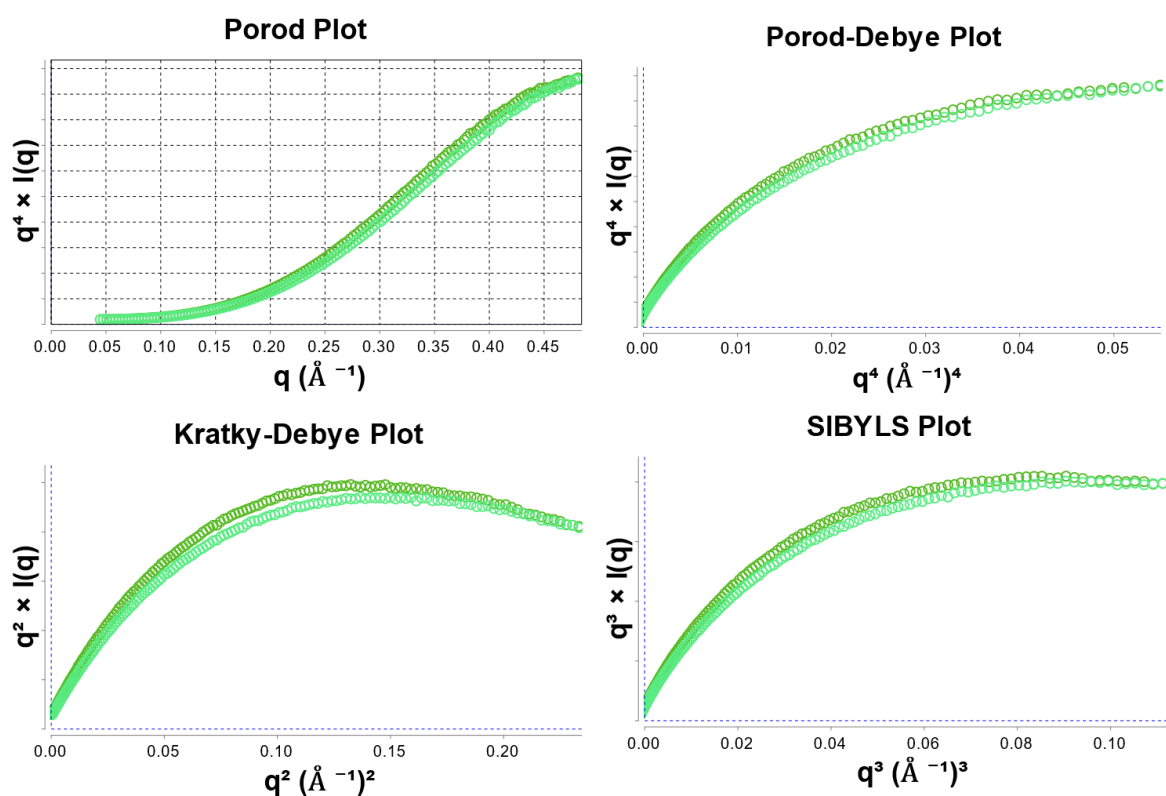
Figure 33 – Dimensionless plots built from scattering intensities measured with samples containing apo *Se*ClpP free from DMSO (dark green curve) and apo *Se*ClpP supplemented with 1% v/v DMSO (light green curve).

## 4.3. Structural aspects of *Se*ClpP-peptidomimetic boronate complex at low resolution

Peptidomimetic boronates are valuable tools for basic research and potential therapeutic development in multiple areas, as they incorporate suitable characteristics: besides the possibility of forming reversible covalent binding, they have a high cell permeability (Micale et al. 2013), great selectivity (Zhang et al. 2016), slow off-rate (Micale et al. 2014), versatility (Diaz and Yudin 2017), and synthetic accessibility (Kaldas et al. 2018).

Ixazomib (Figure 34), the first oral proteasome inhibitor (Gupta et al. 2019), has a safety profile of use because of very low rates of neuropathy, an issue commonly attributed to other drugs with the same mechanism of action (Kaplan et al. 2017). That compound also has improved pharmacokinetics and good oral bioavailability (Zanwar et al. 2018).

Coupled with its boronic acid moiety, the peptidomimetic portion of ixazomib plays an important role in the interactions with serine proteases. By mimicking a natural

peptide, leucine, the ligand can efficiently bind to the ClpP's active sites, minimizing off-target effects. The same part assists in cell penetration and admits optimization for better potency, selectivity, and pharmacological parameters, being a framework for medicinal chemistry.

The dichlorobenzoyl group on the ligand's sidechain improves the selectivity for chymotrypsin-like activity.
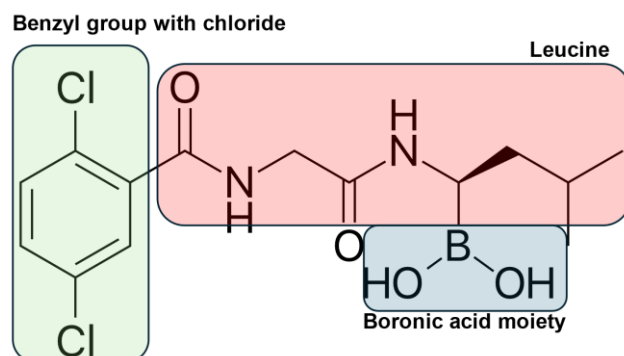
**Figure 34** – Ixazomib molecule with its elemental parts.

For comparison reasons, bortezomib is presented in Figure 35. This compound has a similar mechanism to ixazomib, incorporating the same therapeutical advantages. However, it is injected subcutaneously instead of administered orally (Bross et al. 2004), and its selectivity for proteolytic activity is intermediated by phenyl and pyrazine carbonyl groups. Bortezomib's dipeptide-like backbone is derived from 3-methyl-1-butyl (N-terminal) and phenylalanine (C-terminal). These parts also influence the pharmacokinetic properties.
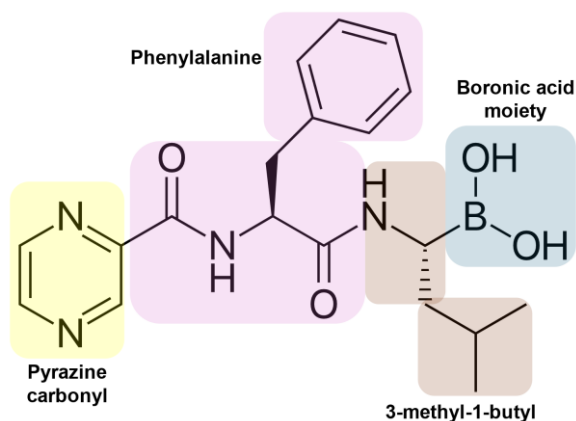
Figure 35 – Bortezomib with its elemental parts.

For studies on the structural biology of *Se*ClpP-ligand complex, ixazomib is initially used for low-resolution analysis by SAXS. Here, tetradecameric and heptameric samples are used to visualize whether changes in oligomerization and in the degree of extension of the protein occur. Once again, SEC-SAXS was performed to demonstrate any peak shift after the drug's incubation.

The first procedure was to mix P1 and P2 samples and use the resulting solution for the measurements. As seen in the chromatogram of the native protein, there are two main peaks, representing the different oligomeric states again (Figure 36). Afterward, the same procedure is performed with ixazomib addition (1:50 protein-to-ligand ratio). SEC-SAXS (Figure 36a) and the scattering intensity profiles (Figure 36b) show the complete depletion of P2 and a more prominent P1 peak. It is evidence that ixazomib, even a canonical inhibitor, is an actor in the induction of the assembly of the tetradecameric *Se*ClpP. This situation is intriguing, as for the first time, a canonical inhibitor is perceived in this oligomerization process. So far, in the scientific literature, ClpP inhibitor was uniquely related to structure stabilization (Ju et al. 2020), compactness (Pahl et al. 2015), or the disassembling of tetradecamer into its more minor constituents (Gersch et al. 2014a).
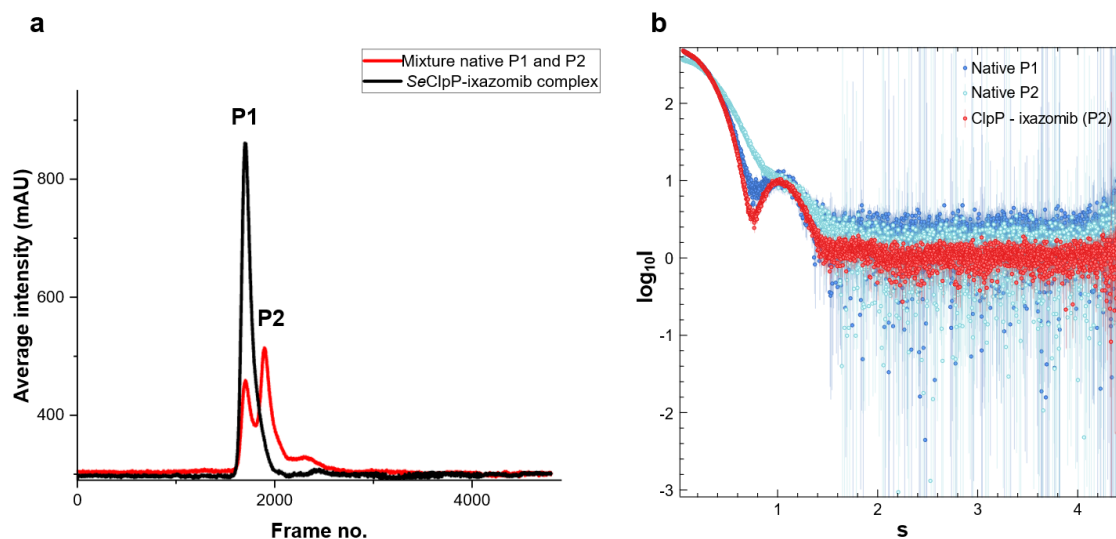

Figure 36 – (**a**) Chromatogram after SEC during SAXS measurements. The red graph represents the sample composed of native *Se*ClpP in P1 and P2 states. After incubation with ixazomib (1:50 protein-to-ligand ratio), the black graph shows the presence of tetradecamers only. (**b**) Intensity scattering profiles of Native P1, native P2, and *Se*ClpP-ixazomib complex. **s**, the scattering vector, as 1/nm.

About protein extension, an initial glance comes from the contrast between the Guinier plots of the apo P1 and the P1-ixazomib complex found in Figures 37a and 37b: the second one has higher R_G value, validating that it is more extended (Figure 37b). The Porod volume (V_P) of P1-ixazomib is also larger than the one determined for the apo SeClpP (Table 16). V_P describes the shape and size of protein in solution, and it is a function of the intensity of scattered radiation at zero scattering angle (I(0)) and the scattering vector s, following the equation below (**16**):

$$V_{P = 2\pi^2 . \frac{I(0)}{s}}$$ (**16**)

Essentially, V_P auxiliates in comprehending the spatial extent based on the intensity of the scattered radiation from biomolecules.
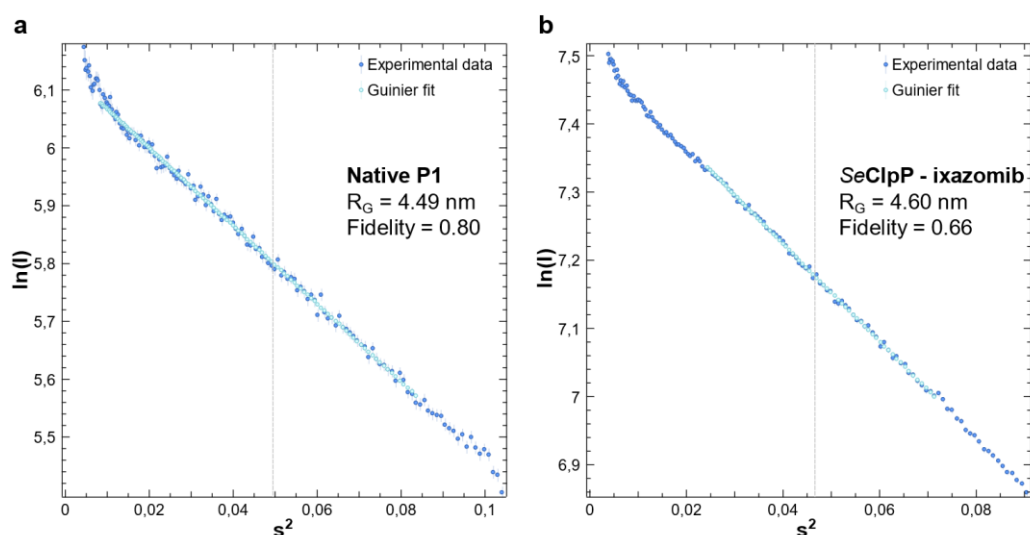
Figure 37 – Guinier plots of (**a**) native P1 and (**b**) SeClpP-ixazomib complex.

The dimensionless plots introduced in Figure 38 support the considerations here. The Porod-Debye plot demonstrates that the apo P1 (purple curve) is more compact than P1-ixazomib complex (green curve), as in the latter case, there is a slight decay through a certain range of q^4. The gap between the curves in Kratky-Debye and SIBYLS plots confirms that the ixazomib-free protein (higher curve) has a R_G value lower than the complex.

Table 16 – Experimental SAXS data and statistics.

	Native *Se*ClpP – P1	*Se*ClpP-ixazomib
Data collection parameters X-ray source Wavelength (nm) Detector distance (m) Temperature (K)	**PETRA III, EMBL'SP12 beamline**	
I(0) (P(r) function)	1011.00	1840.00 ± 0.93
I(0) (Guinier/AutoR_G)	1018.21±0.91	1840.00 ± 5.35
I(0) (SAXSMoW[1])	1015.57	1842.88
R_G (nm) (P(r) function)	4.38±0.002	4.50 ± 0.02
R_G (nm) (Guinier / AutoR_G)	4.49±0.006	4.60 ± 0.002
R_G (nm) (SAXSMoW[1])	4.46	4.57
qR_G limit (Guinier/AutoR_G)	1.30	1.33
qR_G limit (SAXSMoW[1])	1.29	1.30
D_{max} (nm) (P(r) function)	12.43	12.60
Estimated porod volume (Å^3)	392108	476010
χ^2 value [2]	1.00	1.00
CorMap P-value [3]	0.37	0.60
Anderson-Darling test's P-value [4]	0.88	0.61
Molecular mass (SAXSMoW[1])	288.53	318.00
Molecular mass (sequence)	299.15	299.15
Oligomeric state	Tetradecamer	Tetradecamer

[1] Values calculated on SAXSMoW server (Piiadov et al. 2019).

[2,3,4] Statistical parameters that define the quality of SAXS data.
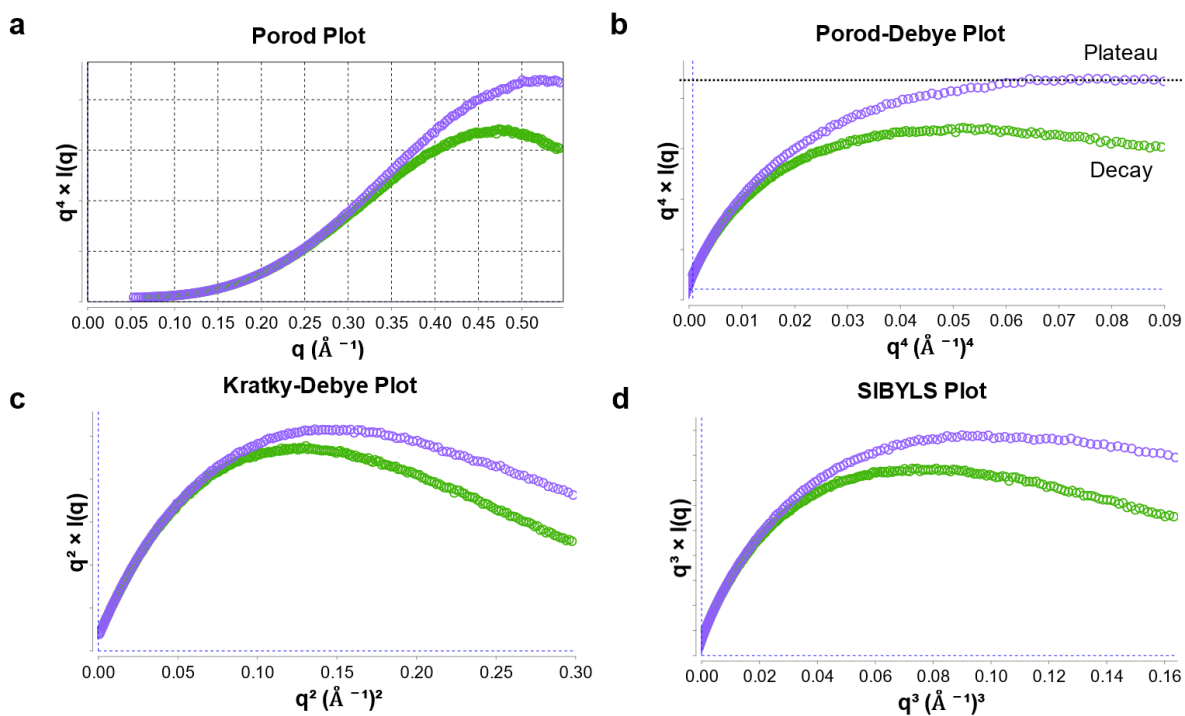
Figure 38 – Dimensionless plots with curves related to (**a**) apo protein with 1% v/v DMSO (purple color) and (**b**) *Se*ClpP-ixazomib complex (green color).

The absence of a plateau in the complex curve means a change in the protein structure, with more extended conformations contributing to the scattering. Instead of a sharp upturn associated with highly flexible or disordered regions, the smooth decay exhibits a gradual change in $q^4.I(q)$ with respect to q^4 (Figure 38b) The slope in the Porod-Debye plot also demonstrates that the extended complex keeps secondary and tertiary structures (helices and sheets), and the surface-to-volume ratio does not greatly increase as in completely disordered states, only suggesting moderate flexibility. The decreased slope is influenced by the cylindrical shape of the extended ClpP, once the scattering profile of this kind of structure is a consequence of its elongated but ordered nature.

Differences in curve height in Kratky-Debye and SIBYLS plots add more details to the previous considerations. As noticed in these graphs, the complex is represented by a curve lower than the one of the ligand-free protein, also demonstrating that the drug induces the protein to reach a more extended state. It comes to the fact that, in this state, there are less pronounced alterations in electron density over short distances and, consequently, in lower overall scattering intensity at the same q values. Moreover, the absence of a plateau in Figures 38c

and 38d means that the apo protein retains more compactness than the complex, but is not fully compacted.

Additionally, in Figure 39, the dimensionless Kratky plot shows that complex (black curve) and apo protein (red curve) are correctly folded. In the plot, two peaks for the multimeric architectures can be seen: the first one refers to the primary structure characteristics, appearing at around $qR_G = 1.73$ and indicating the initial order of the protein with well-defined secondary and tertiary structures. The second peak, on the other hand, informs about high-order structures resulting from the presence of regions of distinct structural features. The second peak related to the complex is slightly dislocated to the right, indicating extension without losing secondary structures.
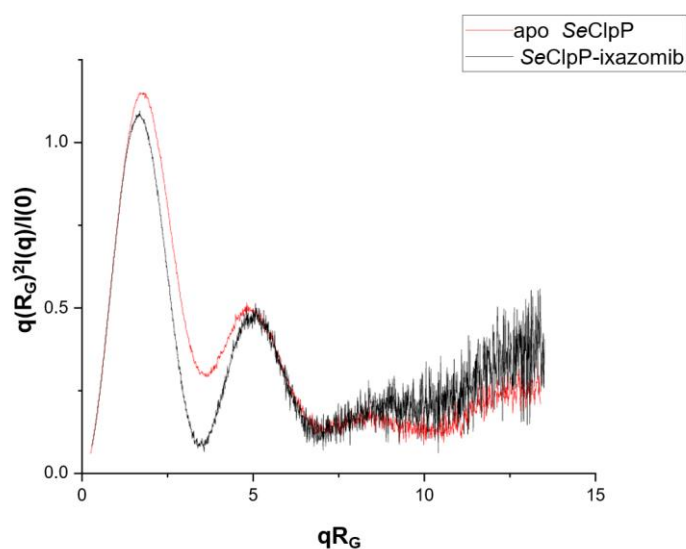

Figure 39 – Dimensionless Kratky plot showing that the second peak of the *Se*ClpP-ixazomib complex (black graph) is slightly shifted to the right.

To conclude this part of the discussion, it is important to consider that the changes observed for protein extension are also detected when the process of protein unfolding or the formation of partially disordered structure occurs. The difference here lies in how intense the modification is. The presence of unfolded species leads to a greater variation of R_G values, a more pronounced shift of the second peak in the dimensionless Kratky plot to higher qR_G values, and more significant deviations from the plateau behavior in Porod-Debye, Kratky-Debye, and SYBYLS plots.

In addition to the SAXS analysis, DLS measurements (Figure 40) show a discrepancy in the hydrodynamic radius of P2, before (Figure 40a, black bar) and

after (Figure 40a, gray bar) the incubation with ixazomib, confirming the oligomerization process. The same parameter attests that the complex (Figure 40b, gray bar) is more extended than apo P1 (Figure 40b, black bar).
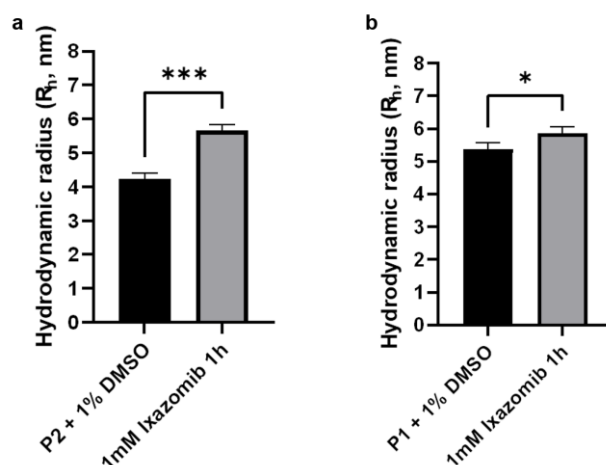
Figure 40 – (**a**) R_h variation calculated for the sample with native P2 before (black bar) and after incubation with the ligand (gray bar). (**b**) R_h variation calculated for the sample with native P1 before (black bar) and after incubation with the ligand (gray bar). t-test shows that the changes in both cases were significant: (**a**) p = 0.0363 (p < 0.05) and (**b**) p = 0.0004 (p < 0.05).

As noticeable above, the R_G and Rh values of the complex are, in fact, higher than those associated with the ligand-free protein. Once again, the presence of DMSO does not seem to affect the structure.

In a more compacted folded and globular protein, such as the apo ClpP, the atoms are tightly packed together, which makes the R_G smaller. Thus, the mass is distributed closer to the center of mass, making it more centralized. On the contrary, in more extended ClpP, the atoms are spread through a larger volume with a higher distance between them and a consequent larger R_G.

Studies with ClpP from *Staphylococcus aureus* (*Sa*ClpP) and ADEP demonstrated alterations in the R_G values after the complex formation with consequent activation of proteolysis (Gersch et al. 2015). Comparing the changes here with the ones from this publication is a way of perceiving how analogous the protein extension triggered by a canonical ClpP activator and peptidomimetic boronates is. In the cited publication, the activation of the enzyme is followed by its extension in the same way that it was noticeable here.

DSF results (Figure 41) were also considered to develop a complete explanation of what was observed until this point. Primarily applied to investigate protein stability under distinct conditions, it is sought to visualize variation in the melting temperature (T_M). In this context, the first derivative peaks calculated from the measurements are of great relevance. They represent the rate of change of fluorescence intensity while the temperature increases. It is an outcome of the unfolding process of ClpP, promoting the exposition of tyrosine and tryptophan, residues capable of absorbing UV light at 280 nm and emitting fluorescence at wavelengths typically around 305 – 310 nm (Khan et al. 2021).

The nanoDSF's output data is normally dependent on the protein-to-ligand ratios and, in terms of ixazomib, an unexpected characteristic is noted at low concentrations. Between 20 – 78 µM (1:2 to 1:7.8 protein-to-ligand ratios), a set of two peaks are seen: one with a melting temperature similar to the apo protein (51°C) and another one with T_M higher (60 – 68°C). As more ixazomib is added, the first peak starts shrinking until its complete disappearance. The remaining one shifts to the right (higher T_M), demonstrating increased protein's thermostability.
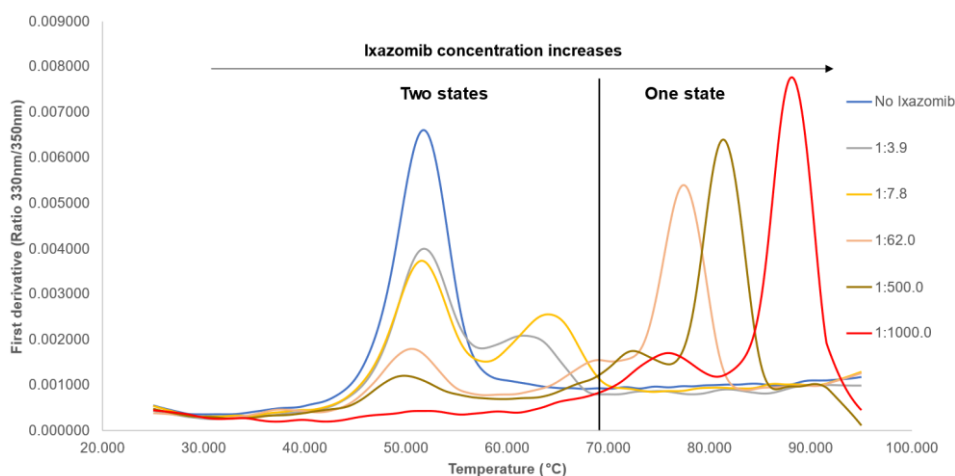
Figure 41 – First derivative peaks obtained from nanoDSF measurements. At low protein-to-ligand ratios, there are two peaks for two different states. At higher ixazomib concentrations, one predominant peak is observed at high T_M values.

At low protein-to-ligand ratios, the peak on the left corresponds to the unbound state, and the one on the right is the bound state, with their unfolding transition resulting from distinct stabilities. Published ITC studies with peptidomimetic boronates corroborate this interpretation. They are based on the customization of a mathematical model to describe the change from a tense ClpP (unbound) to a

relaxed ClpP structure (bound), at different drug concentrations (Felix et al. 2019). In the work, as more bortezomib was added, more relaxed and extended structures were present. Nevertheless, until they became predominant in the sample, another group composed of tense ClpP state was also detected.

4.4.   Preparation of studies on *Se*ClpP-ixazomib complex in solid-state

To obtain the complex and analyze it in detail, there are two fundamental techniques in protein crystallography known as soaking and cocrystallization. When displayed at high resolution, binding modes and non-covalent interactions give valuable insights into how protein-drug structures are relevant for pharmacology.

In the soaking process, a crystal of the apo protein is soaked in a solution composed by the reservoir solution and the ligand of interest at high concentration. In this case, a relevant aspect is the solvent content found in the protein crystal. This parameter refers to the volume occupied by the solvent molecules, in opposition to the protein molecules themselves, and this knowledge demonstrates if there are enough diffusion pathways for the drug to penetrate the crystal and access the binding sites. The speed of this penetration can also be estimated using this information. Besides that, a proper solvent content tends to maintain stability during soaking, avoiding cracking, dissolution, or distortions caused by conformational changes.

In mathematical terms, the solvent content is calculated from the following equation (**17**):

$$Solvent\ content\ (\%) = \left[1 - \left(\frac{1.23}{V_M}\right)\right] \tag{17}$$

where

V_M is the Matthews volume.

Nevertheless, V_M depends on V_c, which is the volume of the unit cell and therefore derived from its parameters: lengths of the edges (*a*, *b*, *c*) and the angles (α, β, γ). If the crystal system is monoclinic like in *Se*ClpP (P 2_1), then a = b = 90° and g ≠ 90° and the V_c calculation is as follows (**18**):

$$Vc = a.b.c \qquad\qquad\qquad\qquad\qquad\qquad\qquad\qquad\qquad\qquad\qquad (18)$$

Thus, V_M is given by (**19**):

$$V_{M=} \frac{V_c}{N.M}$$

(**19**)

where

 V_c is the volume of the unit cell.

        M is the molecular weight of the protein.

        N is the number of molecules in the asymmetric unit.

Since the solvent content is approx. 49%, *Se*ClpP crystal is in the class of moderate solvent content (40% - 60%), facilitating good diffraction properties and adequate space for interactions and flexibility.

Based on that, after growing and harvesting, some apo *Se*ClpP crystals were collected and submitted to soaking with 10 mM ixazomib, in the crystal's reservoir solution, hampering any crystal loss by alterations of solution composition and the physicochemical environment (mainly the pH value).

The soaked crystals were removed after 1 hour and immediately frozen for ulterior data collection. With X-ray diffraction data, the crystal structure of the *Se*ClpP-ixazomib complex, after molecular replacement (search model's PDB ID: 3V5E; homology 98.45 %)and refinement procedures, is depicted in Figure 42. Table 17 brings X-ray diffraction details and refinement statistics for the complex.
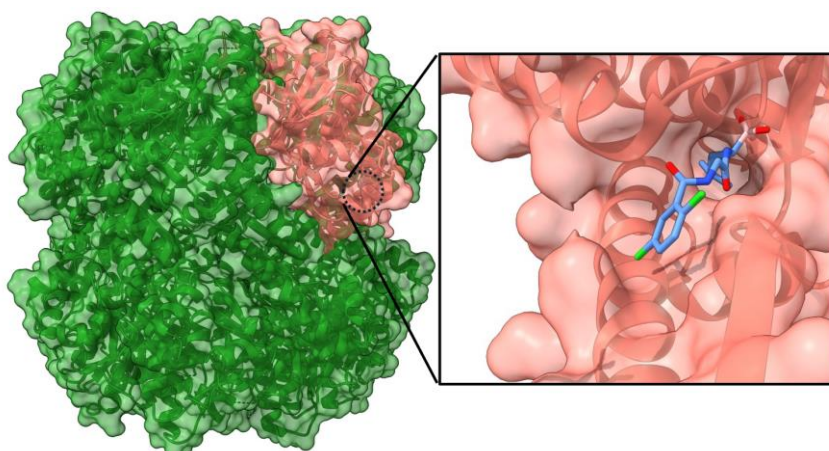
Figure 42 – Crystal structure of *Se*ClpP-ixazomib complex and a ligand molecule bound to one of the ClpP's catalytic sites.

Table 17 – X-ray diffraction data and refinement statistics (*Se*ClpP – ixazomib).

*Se*ClpP – ixazomib (soaking)	
Data collection	
X-ray source	P11, PETRA III, DESY
Detector	Pilatus 6M
Space group	P 2_1
Cell dimensions	
a, b, c (Å)	94.96, 123.16, 125.24
Wavelength (Å)	1.03
Resolution (Å)	47.94 – 2.33 (2.41 – 2.33)
Total reflections	856843 (85183)
Total unique reflections	123893 (12335)
Redundancy	6.9 (6.9)
Wilson B-factor (Å^2)	40.15
R_{meas}	0.14 (1.30)
$CC_{1/2}$	1.00 (0.61)
V_M (Å^3/Da)	2.37
I/σI	12.85 (1.56)
Completeness (%)	99.93 (99.96)
Refinement	
Reflections used	123871 (12336)
Reflections used for R_{free}	1768 (176)
R_{work}	0.21 (0.30)
R_{free}	0.22 (0.33)
No. of atoms	
protein	19005
ligands[1]	322
water	579
Average *B*-factor (Å^2)	45.98
macromolecules	45.75
ligands[1]	57.45
water	47.13
R.m.s deviations	
bond lengths (Å)	0.01
bond angles (°)	1.14
Ramachandran	
favored (%)	98.25
allowed (%)	1.75
outliers (%)	0.00
PDB ID	8QYF

Values from the last shell are presented between parentheses.

[1]Ligands: ixazomib molecules and acetate ions.

4.5.   *Se*ClpP function under ixazomib modulation

Once the *Se*ClpP-ixazomib complex was preliminarily explored at low and high resolutions, it is interesting to evaluate the impact of ixazomib on the *Se*ClpP function. Initially, various enzyme concentrations were evaluated through the fluorescence increase from the hydrolysis of Suc-LY-AMC over time (Figure 43a). Curves built in this procedure were submitted to linear fit, and the initial velocities (V_0) are the angular coefficients of the generated equations. V_0 is critical to determine the *Se*ClpP concentration for the assays, as at the very beginning, side reactions are scarce, and the levels of protein and substrate can be considered constant. Although linearity is seen in all curves, it was decided to proceed with 0.5 µM *Se*ClpP (Figure 43b).
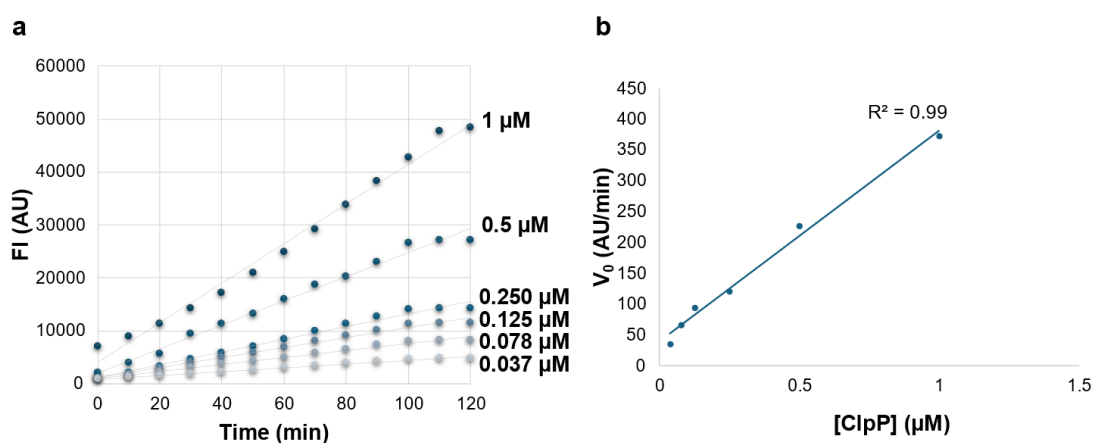
Figure 43 – (**a**) Fluorescence assays with different *Se*ClpP concentrations. (**b**) Linear fitting with the initial velocity (V_0) for each one of the *Se*ClpP concentrations in (**a**). FI means fluorescence intensity.

Michaelis-Menten equation describes how the reaction rate (V) is related to the substrate concentration ([S]). The mathematical model that establishes this relationship is as follows (20):

$$V = \frac{V_{\max}[S]}{K_m + [S]}$$
                                                                             (20)

where

   $V_{\max}$ represents the maximum reaction rate when the enzyme is fully saturated with the substrate.

   K_m is the Michaelis-Menten constant.

[S] is the substrate concentration.

The kinetic model of *Se*ClpP has a Michaelis-Menten behavior, yielding a hyperbolic curve with a correlation coefficient 0.99. K_m, the substrate concentration associated with the half of V_{max}, is 145.8 ± 15.9 μM. V_{max} is 603.5 ± 23.8. Based on K_m, the substrate concentration was defined for the assays: 150 μM.

After the operational concentrations of the enzyme and substrate were defined, reactions within a range of pH and temperature values were performed. According to Figure 44, the best conditions for *Se*ClpP are pH 7.5 (Figure 44a) and 36°C (Figure 44b), defining this protein as an alkaline peptidase and mesophilic.
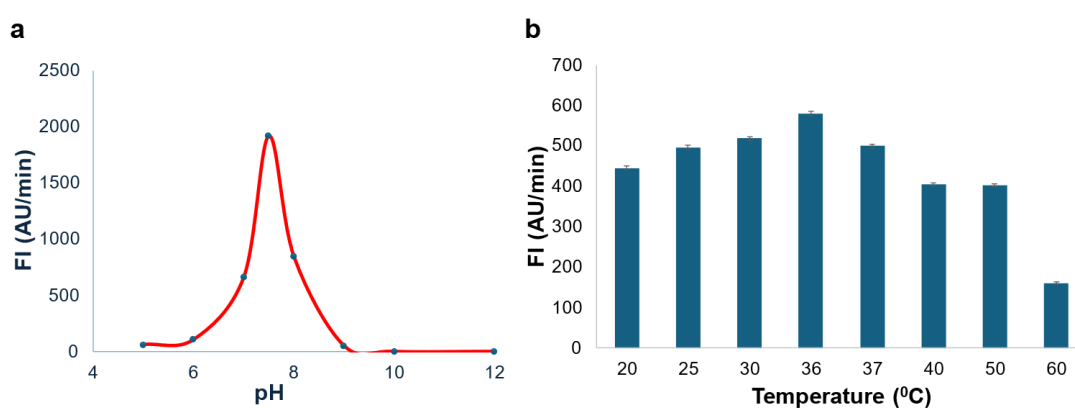

Figure 44 – Determination of optima pH and temperature values for assays with *Se*ClpP. FI is fluorescence intensity.

The biochemical study on *Se*ClpP modulation by ixazomib started with peptidolysis. It is particularly significant for checking activity alteration with shorter oligopeptides as substrates. Hence, the initial focus is not on the geometry of the axial pores, but on eventual changes promoted by the ligand at the level of the catalytic sites. In Figure 45a, starting from low protein-to-ligand ratios, paradoxically, the degradation of Suc-LY-AMC increases up to 1:3 (*Se*ClpP-to-ixazomib ratio). At higher ligand concentrations, the opposite happens, and the inhibitory effect becomes predominant. Along these lines, ITC measurements with *Se*ClpP and ixazomib were performed, and its interpretation is analogous to the one based on nanoDSF, indicating the transition to a more extended biomacromolecule with the existence of two states at low protein-to-ligand ratios. In Figure 45b, the fitted curve can be divided into two portions where distinct regions of enthalpy variation (ΔH) are noticed. This characteristic results from a

cooperative mechanism that alters the binding affinity, and it is a consequence of geometrical modifications of the catalytic region. The ΔH, when the measurements started (step 1), shows an intense exothermic process associated with protein stabilization and conformational modifications leading to an extended state with the formation of new interactions between protein and ligand. Furthermore, the second enthalpy variation (step 2), also with heat release, brings information about a complex binding process, where protein extension accompanies the protein-ligand interactions, generating multiple phases of binding events, each one with particular enthalpy contributions.
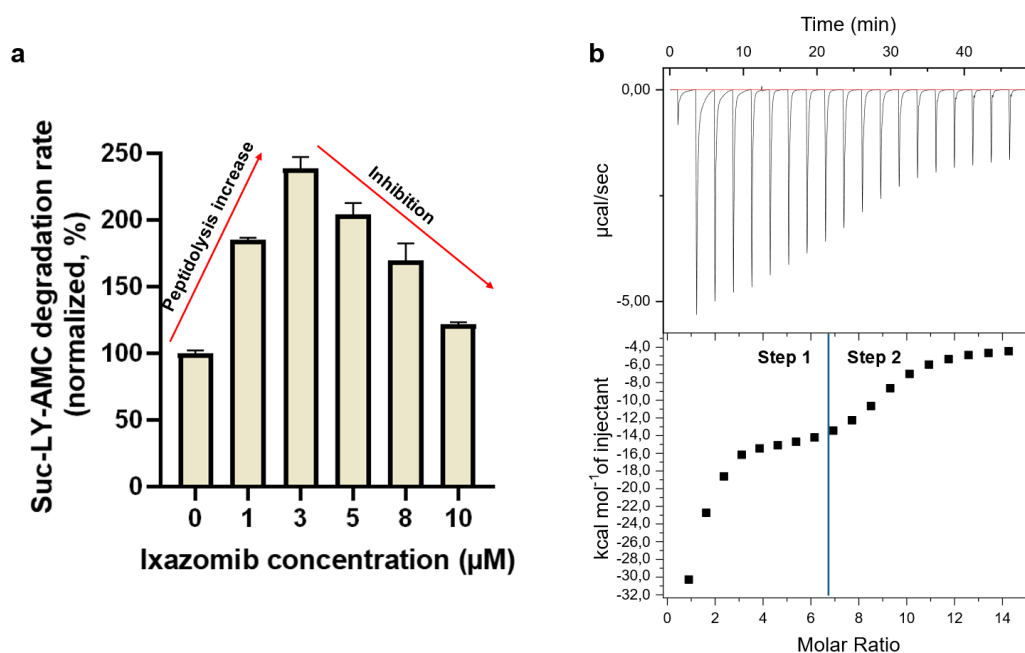

Figure 45 – (**a**) Degradation of Suc-LY-AMC in the presence of different ixazomib concentrations. Lower protein-to-ligand ratios result in the enhancement of peptidolysis up to 1:3. In sequence, as more ligand is added, only inhibition is observed. This dual modulation is justified by (**b**) ITC measurements: when the drug starts populating the protein, a cooperative effect happens with heat release. At this stage, the peptidolytic activity increases until a second process of heat release is noted, and then the inhibitory effect becomes predominant.

As demonstrated in Figure 46, the peptidomimetic portion of ixazomib interacts, via hydrogen bonds, with important residues (His123, Met99, Gly69, Val71, and Leu126), promoting an optimized conformation for the access and hydrolysis of the

substrate. Considering the reversible covalent bond between the ligand and Ser98, the catalytic triad becomes free for catalysis.

In the Appendix, section A7, ixazomib is shown in each one of the 14 catalytic sites of *Se*ClpP.
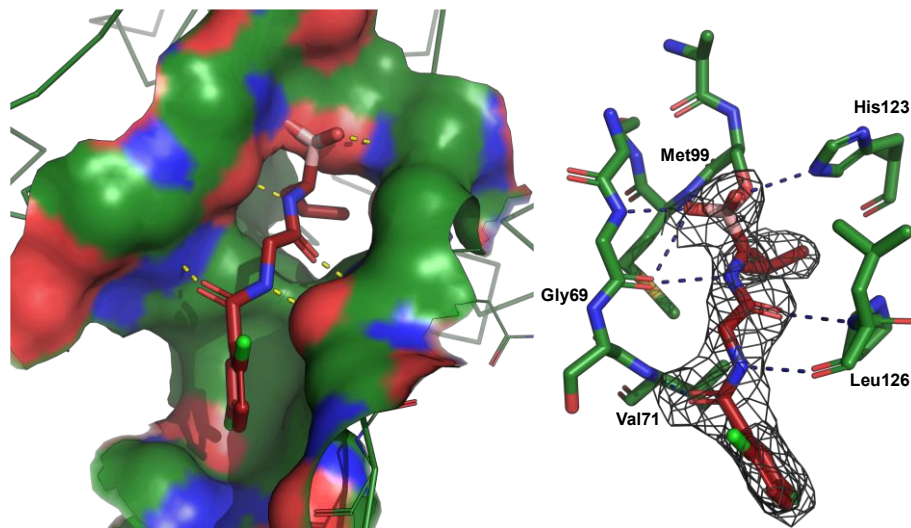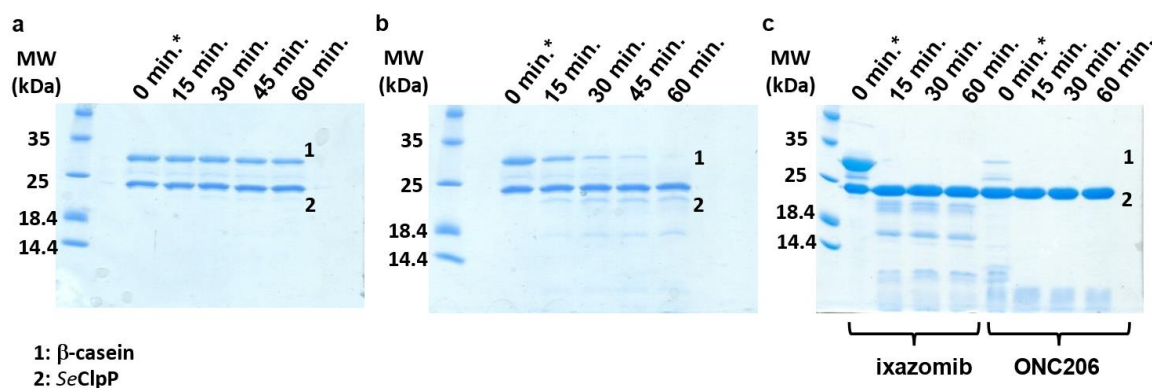

Figure 46 – Interaction between ixazomib and SeClpP: While the boronic acid moiety is covalently bound to Ser98, the peptidomimetic portion forms hydrogen bonds with important amino acid residues in the vicinity of the catalytic triad, making the entire protein structure more stable and optimizing its function. Ixazomib is shown with the 2Fo-Fc electron density at 1.5σ.

Assays with β–casein have shown that ixazomib dysregulates the proteolysis as well. In Figure 47, the proteolytic function is only perceived at 500µM ixazomib (Figure 47b) (1:50 protein-to-ligand ratio) and 1000 µM (Figure 47c) (1:100 protein-to-ligand ratio), and not with 200 µM ixazomib (Figure 47a). To contrast with the modulation triggered by an activator bound to the "hydrophobic pockets", the reaction with SeClpP and ONC206, an imipridone compound (Jacques et al. 2020), was performed at a 1:1 protein-to-ligand ratio, and the substrate was completely degraded as soon as this ligand was added.

In this comparison, another conclusion appears: reactions with ONC206 and ixazomib generate different profiles of degradation products. The imipridone modulation results in products with molecular weights lower than the compounds produced by ixazomib activation. It is hypothesized that the presence of the boron-based compound in the catalytic sites, although it dysregulates ClpP activity, has

the potential to cause some steric hindrance, influencing the processive hydrolysis of the products to shorter oligopeptides.


Figure 47 – 15% SDS-PAGE after reactions with β-casein monitored for a period of 60 minutes. (**a**) ixazomib and SeClpP concentrations: 200 μM and 10 μM, respectively; (**b**) ixazomib and SeClpP concentrations: 500 μM and 10 μM, respectively; (**c**) Comparative experiment with ixazomib (1 mM) and ONC206 (10 μM), where it is noticeable that the MWs of product fragments vary, in accordance with the ligand used. A possible explanation for this difference is that ixazomib occupies the catalytic sites, affecting the processive degradation of the substrate. ONC206 only binds to the allosteric regions. Degradation products of low molecular weight can be clearly seen in (**b**) and (**c**). *t= 0 min corresponds to the time point with no incubation, but until the complete denaturation of the protein prior to the SDS-PAGE, β-casein degradation happened in the quick reaction with ONC206.

4.6. Comparative analysis of two mechanisms of ClpP activation: peptidomimetic boronate and the mutant SaClpP Y63A.

The orientation of the Asn42 residue is one of the indicators of the opening of the gating mechanism of the ClpP's axial pores and the proteolysis activation, subsequently. In a general manner, ADEP molecules bound to the "hydrophobic pockets" induce the shift of the Asn42 sidechain from an "up" to a "down" position. This process is also pivotal in assuring an adequate configuration of the proteolytic chamber.

The inspection of the open ClpP proves that the orientation shift of Asn42 proceeds the same way. Besides that, in the "down" position, Asn42 is farther away from Tyr21, indicating another feature involved with the dysregulation of ClpP function. Apart from the previous context, there is a difference between ClpP-ADEP and ClpP-peptidomimetic boronate complexes: in the first structure, the Asn42 residue is in "down" position in all the subunits. In the second case, the same setup is seen

in some of the subunits. A publication based on experiments made with a *S. aureus* ClpP mutant, *Sa*ClpPY63A (Ni et al. 2016), is another example proving that the activation occurs, even if the change is not propagated through every monomer. The residue Y63 is involved in hydrogen bonding within the tetradecameric ClpP, being essential for the allosteric network connected to protein activation. Then, interactions between Y63 and ATPases or compounds like ADEP play a major role in the orientation of the N-terminal loops for the translocation of globular proteins to the catalytic chamber. However, the replacement of Y63 by an alanine (A63) propagates a "domino effect" until Asn42 residues, leading them to "down" position in some ClpP subunits. Like in *Se*ClpP-ligand complex, this is enough to initiate proteolysis. A ClpP subunit from *Sa*ClpPY63A and one from *Se*ClpP-ixazomib complex are depicted in Figure 48.
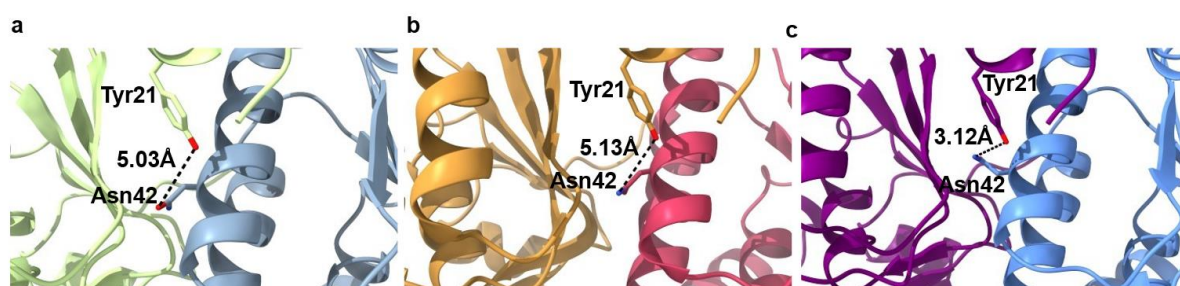
Figure 48 – (**a**) *Se*ClpP-ixazomib complex, (**b**) *Sa*ClpPY63A mutant, and (**c**) native SeClpP. In (**a**) and (**b**), the Asn42 residue is in "down" position, indicating that the structure is active for proteolysis and open for the access of globular proteins, and explaining the observations in Figure 47. Conversely, the "up" Asn42 in apo *Se*ClpP reflects the closed nature of (**c**).

## 4.7. Effects of chemical chaperones on *Se*ClpP function

Although there are many similarities in amino acid sequences and tridimensional conformations among ClpPs from various source organisms, minor distinctions may antagonistically influence the affinity for ligands and the oligomeric state. In order to illustrate this context, there are some empirical discoveries to be considered: experiments with ClpP from human mitochondria (*Hs*ClpP), one unique variation of an amino acid residue in the hydrophobic pockets was crucial for the discovery of an organism-specific activator (Stahl et al. 2018). Apart from that, mutations of key residues determine the dismantlement of the active state of ClpP into their constituent parts. Experiments with *Sa*ClpP, where the Asp142 from the catalytic triad was substituted by an Asn, led to a compact tetradecamer.

Asp142 is involved in a network of interactions that affects the connection between opposing subunits. Nonetheless, after the protein is complexed with the compound ADEP, the structural change is revoked, and *Sa*ClpP extends again (Gersch et al. 2015). This single example reveals how complex the mechanisms behind the ClpP dynamics are.

In this regard, secondary compounds like buffer constituents and precipitant agents can also exert a similar influence. MPD was perceived to form hydrogen bonds to His123 from the ClpP's catalytic triad. Even if that chemical may not be considered relevant for discovering and synthesizing novel antibiotics, its interaction with the enzyme can bring helpful information for structural biology. However, in many PDB entries, for example, the electron density characteristic of MPD is noticeable, but it is kept empty in the depositions.

At low pHs, the imidazole group in the side chain of His123 is flipped away from Ser98, and the overall structure gets compressed and inactive (Ripstein et al. 2020b). When this observation is linked to the fact that ClpP is inactive under acidic conditions, a question arises: could MPD avoid conformational changes under low pHs, keeping the protein extended? Information extracted from other crystal structures is significant for this discussion. In a publication with two crystal structures of *Sa*ClpP obtained in a crystallization condition without MPD, results demonstrated that, at pH 3.5, the macromolecule is in a compressed state. Moreover, cryo-EM structures of ClpP from *Neisseria meningitidis* (*Nm*ClpP) have structural differences when the pH changes slightly from 8.5 to 7.0 (Ripstein et al. 2020b). Similarly, in cryo-EM experiments with ClpP from *Bacillus subtilis* (*Bs*ClpP), structures at pH 4.2 and 6.5 were compressed and extended, respectively. In Figure 49, there is the multiple sequence alignment (MSA) with *Se*ClpP, *Sa*ClpP, *Nm*ClpP, and *Bs*ClpP.
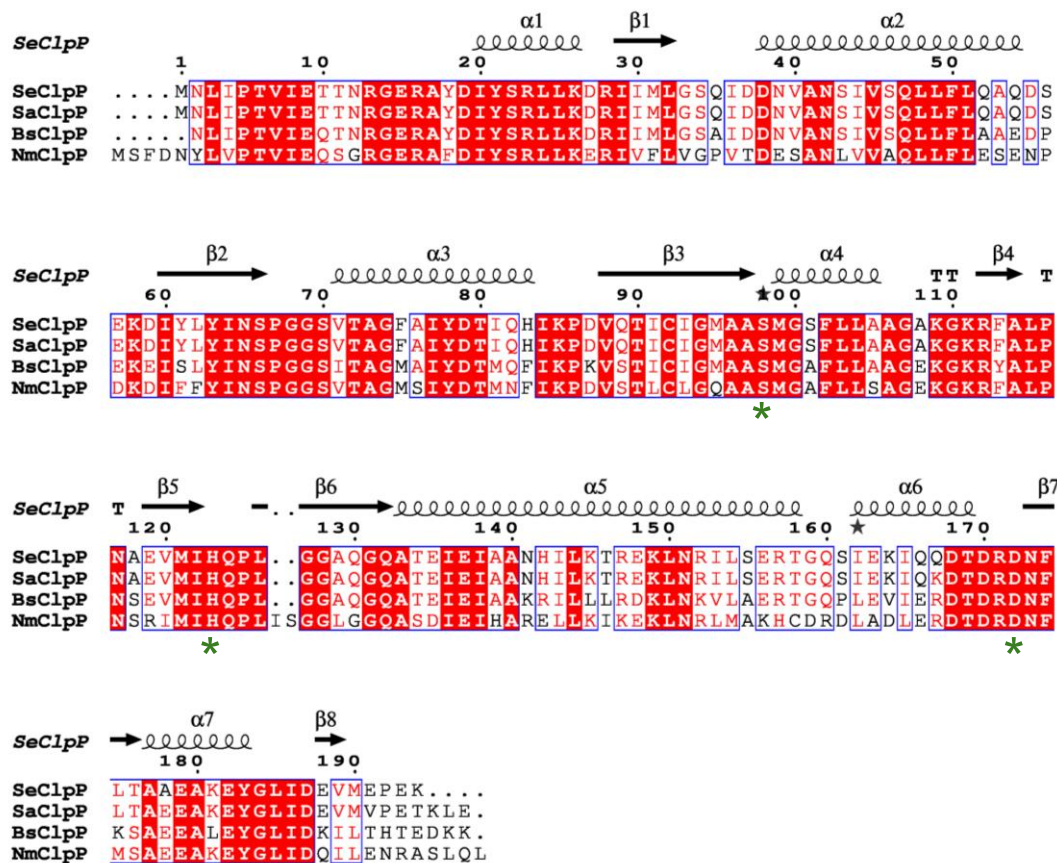
Figure 49 – MSA with assigned secondary structures of *Se*ClpP and its homologs: *Sa*ClpP (PDB: 3QWD), *Bs*ClpP (PDB: 3TT6), and *Nm*ClpP (PDB: 7KR2). Identical, similar and non-conserved regions are highlighted in red boxes, red letters, and black letters respectively. There are no considerable variations in the E-helix (α5) and gly-rich portion (β7), regions involved in the heptamer-heptamer interactions. The residues of the catalytic triad, Ser98-His123-Asp172, are indicated by green asterisks. Sequence alignment was performed by EsPript3 server (Robert and Gouet 2014).

MPD may have a role in the stabilization process, as it keeps the "active" position locked, where the distances between the atoms His123-Nϵ1 and Ser98-OD1 are typical of a hydrogen bond (Figure 50a). It also plays a role in the extension of the E-helices, and this mechanism promotes a favorable situation for the formation of hydrogen bonds in the gly-rich region of the opposing subunits. The same region, when in compact and compressed states, is not a beta-sheet anymore, and the E-helix gets kinked (Figure 50d). Because of this characteristic, Ser98 and His123 are approx. 8 Å apart, and therefore the protein is inactive (Figure 50b).
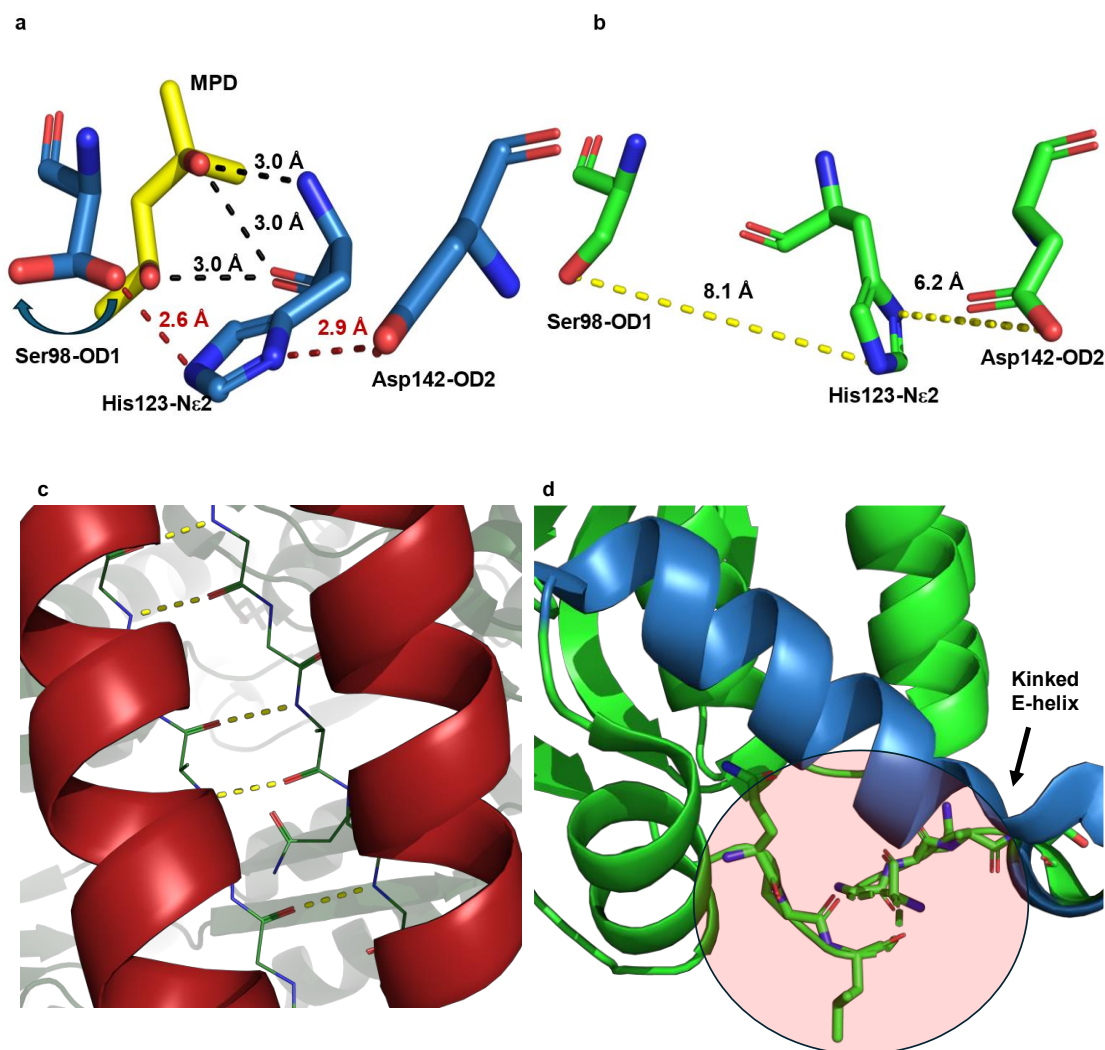
106

Figure 50 – (**a**) Catalytic triad of *Se*ClpP where the amino acid residues Ser98-His123-Asp172 interact via hydrogen bonds (active and extended conformation). On the other hand, in (**b**), His123 is flipped and far away from Ser98 (inactive and compressed conformation) in *Sa*ClpP (PDB: 3QWD). (**c**) shows that the gly-rich region and E-helix are organized in the extended *Se*ClpP. Stabilizing hydrogen bonds are in yellow (**c**), and the disordered gly-rich region and kinked E-helix in the compressed state are highlighted in (**d**).

In the same direction, another common compound was found to be significant for characterizing *Se*ClpP: glycerol. The initial motivation for selecting this triol was its effect on the purification of the ClpP from *Bacillus subtilis* (*Bs*ClpP) (Gersch et al. 2015). As ventilated previously, the modification of the sample environment has the potential to modify the protein's state, not only the extension or compactness degree of the structure of the two-stacked heptameric rings, but also how many oligomers are in equilibrium. Then, in the case of *Bs*ClpP, it turned out that glycerol

caused the isolation of the enzyme as 14-mers, while in the absence of this chemical, monomer species could be detected as well.

When *Se*ClpP was solubilized and purified with a buffer containing 20% v/v glycerol, a similar result was obtained: in SEC chromatogram (Figure 51a), the curves representing samples with and without the triol can be compared. In the first configuration (black chromatogram), there are the peaks P1 (tetradecamer) and P2 (heptamer) as beforehand. Conversely, in the latter one (red chromatogram), the P1 was the major peak, and only a small amount of monomers was present (represented with an *).

Another aspect is that the P1 with glycerol was eluted slightly earlier than the P1 free from it. This could be linked to an eventual protein extension, which would alter its hydrodynamic volume. Then, DLS measurements were performed on both samples, and the one with the chemical chaperone is associated with a R_H = 6.2 nm, while the other value for the glycerol-free *Se*ClpP was R_H = 5.3 nm, approximately (Figure 51b), confirming the aforementioned hypothesis.
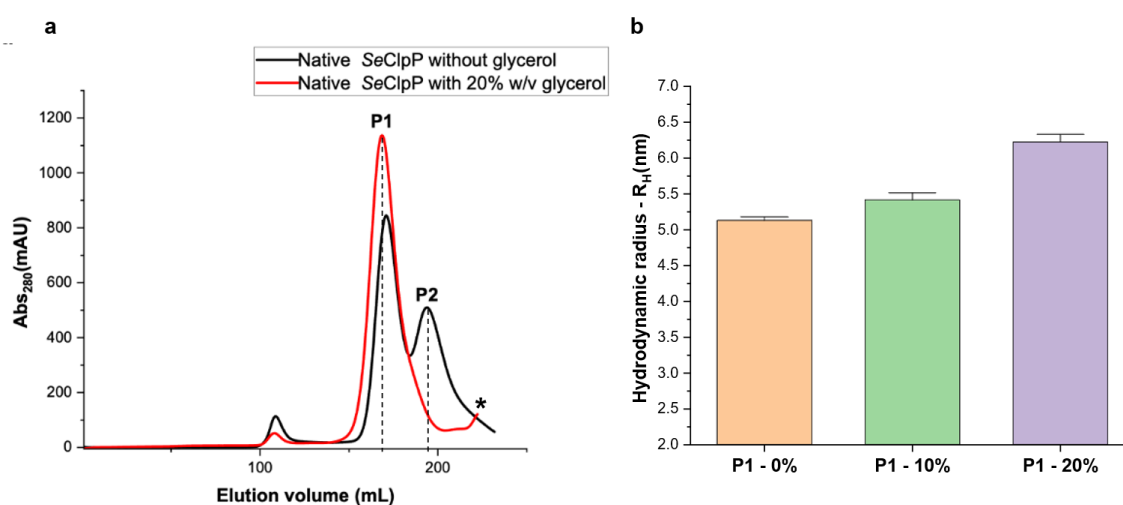

Figure 51 – Impact of glycerol, a common chemical chaperone, on the *Se*ClpP state and hydrodynamic radius (R_H). (**a**) SEC chromatograms represent the samples free from glycerol (black curve) and containing it (red curve). In the second case, P1 starts being eluted earlier, and DLS measurements in (**b**) demonstrate that its R_H is approx. 17% higher.

The logic behind glycerol's effect is linked to its role as a chemical chaperone, stabilizing proteins in their native structure. T-ramp studies with DLS indicate that *Se*ClpP becomes more thermostable in the presence of that agent, and this feature can be demonstrated in the magnitude of the onset temperature (T_{onset}). T_{onset} is

related to the beginning of protein aggregation, during the system's heating. Therefore, at T_{onset} onwards, the hydrodynamic radius drastically increases, depending on the protein's characteristics. In Figure 52, the curve representing the ClpP with glycerol shows that T_{onset} is 4°C higher in this case.
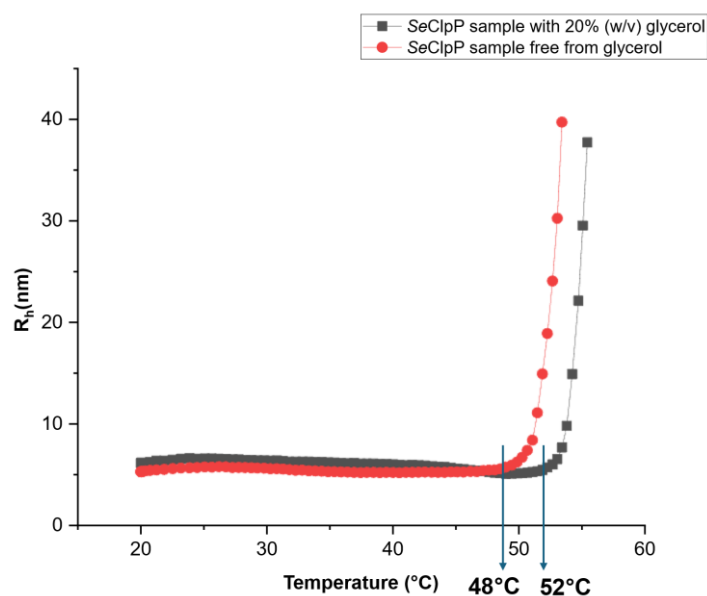
**Figure 52** – T-ramp experiments with (**a**) *Se*ClpP P1 free from glycerol (red curve) and (**b**) with 20% w/v glycerol (black curve). The T_{onset} for each set of measurements is presented here. R_h is the hydrodynamic radius in nanometers.

An additional question is how or if the structural modifications impact the enzyme's function. Then, assays with Suc-LY-AMC were performed (Figure 53). In addition to the control without the triol in question, 0% w/v, reaction mixtures with four different concentrations were prepared: 2% (w/v), 5% (w/v), 10% (w/v), and 20% (w/v). At the lowest concentration, there was already a considerable increase in substrate degradation: more than 30%. Increases in activity were observed up to 10% (w/v) and a small decrease at 20% (w/v). Although the latter concentration has a more prominent effect in terms of structural alteration, a large amount of glycerol can hinder the interaction between protein and substrate.
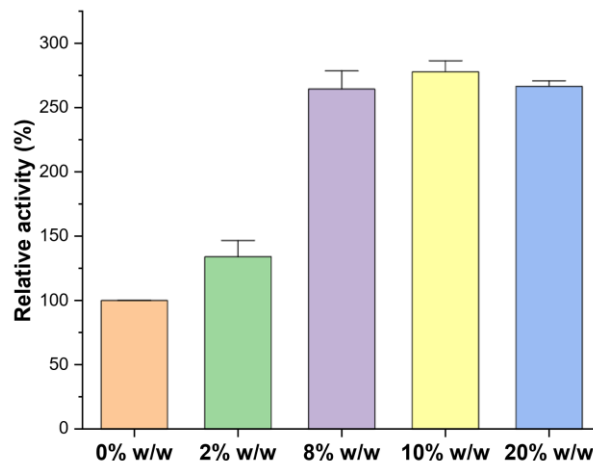
Figure 53 – Enzymatic assays with different glycerol concentrations.

From this graph, an approach based on X-ray crystallography showed something not yet seen in a high-resolution model: a glycerol molecule interacting via hydrogen bonds with the His123 side chain, particularly with the Nε2 nitrogen, inducing the proper orientation for the substrate's hydrolysis. Other hydrogen bonds are formed with the residues Gly69 and Leu126, which are essential to maintain the proper geometry of the catalytic sites and the macromolecule's oligomerization. Any interference in the structural network involving both residues and His123 (Figure 54) is expected to affect the modulation of the enzymatic activity.
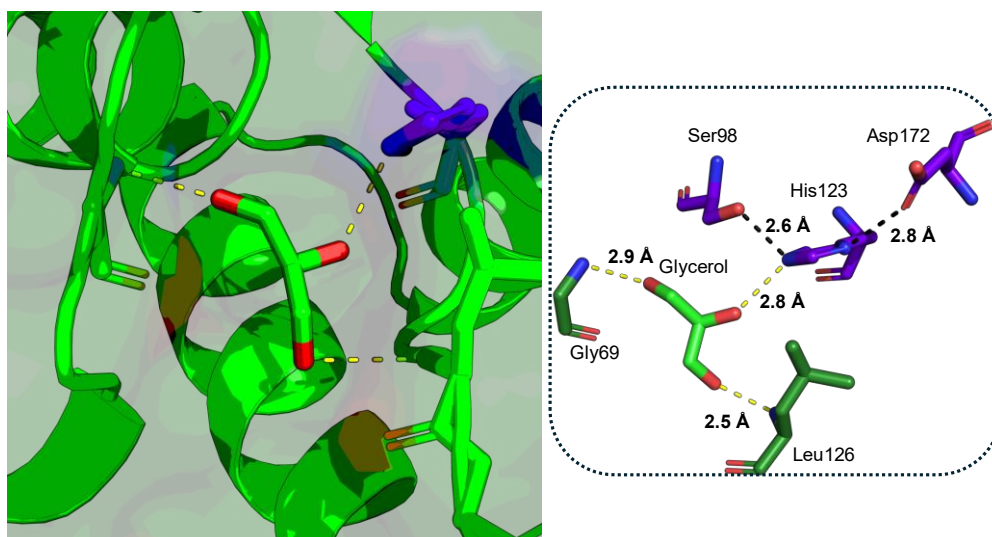
Figure 54 – Details of the ClpP's catalytic site with glycerol and details of the network of hydrogen bonds with His123, Gly69, and Leu126 (yellow dashed lines). The hydrogen bonds in the catalytic triad are depicted as black dashed lines.

Like in the native ClpP without glycerol, hydrogen bonds stabilize the stacking of the two heptameric rings. In this regard, only one difference is noted: instead of having six bonds, there are seven now, resulting in more stability to the tetradecameric and extended conformation (Figure 55).
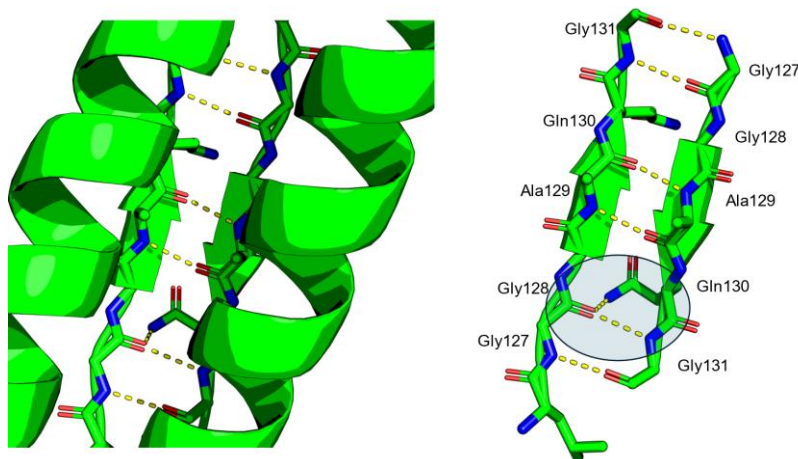
Figure 55 – Visualization of the network of hydrogen bonds (yellow dashes) connecting two opposing SeClpP subunits and the two heptameric rings, consequently. On the right side, the location of the extra bond is located within the ellipsis: it is the result of the interaction between the side chain of Gln130 and the backbone of Gly128.

Table 18 shows X-ray diffraction data and refinement statistics for *Se*ClpP bound to glycerol. The phase problem was solved my molecular replacement, using the tetradecameric *Sa*ClpP (PDB ID: 3V5E; homology: 98.45%) as search model.

From this point, other questions arise: could this chemical chaperone somehow alter how peptidomimetic boronates modulate ClpP? Would there be any synergism between them, or would one cancel out the impact of the other? The enzymatic assays with Suc-LY-AMC (Figure 56) shed some light on those queries. Prior to the assays, ixazomib was added to the sample supplemented with 10% (w/v) glycerol, and the resulting solutions were incubated in the plate reader at 36°C, for 30 minutes. Control without ixazomib was also used, following the same protocol as the previous incubation. Subsequently, the fluorogenic substrate was added as well, and then the reading of the fluorescence intensity was collected for 60 minutes. At the end of it, preliminary graphs indicated an interesting profile: the initial velocity in samples with glycerol was slower than in control. Regardless of the ligand concentration, the increase in peptidolysis was no longer observed at lower protein-to-ligand ratios.

Table 18 – X-ray diffraction data and refinement statistics (glycerol supplementation).

| Native *Se*ClpP – 20% (w/v) glycerol	
Data collection	
X-ray source	P13, EMBL, PETRA III, DESY
Detector	EIGER 16M
Space group	$P\,2_1$
Cell dimensions	
a, b, c (Å)	93.61, 123.99, 126.69
Wavelength (Å)	0.83
Resolution (Å)	55.68 – 2.39 (2.47 – 2.39)
Total reflections	717210 (65430)
Total unique reflections	114288 (11339)
Redundancy	6.3 (5.8)
Wilson B-factor (Å^2)	44.96
R_{meas}	0.10 (0.79)
$CC_{1/2}$	1.00 (0.82)
V_M (Å^3/Da)	2.37
I/σI	13.18 (2.46)
Completeness (%)	99.90 (99.94)
Refinement	
Reflections used	114252 (11338)
Reflections used for R_{free}	5701 (582)
R_{work}	0.20 (0.26)
R_{free}	0.23 (0.33)
No. of atoms	
protein	19327
ligands[1]	172
water	562
Average *B*-factor (Å^2)	48.34
macromolecules	48.27
ligands[1]	55.36
water	48.46
R.m.s deviations	
bond lengths (Å)	0.005
bond angles (°)	0.77
Ramachandran	
favored (%)	98.09
allowed (%)	1.87
outliers (%)	0.04
PDB ID	9FSW

Values in parentheses refer to the last shell.

[1]Ligands: glycerol and MPD molecules.
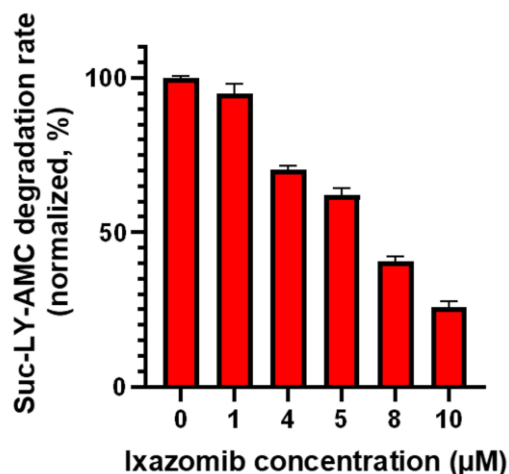
Figure 56 – Enzymatic assays with Suc-LY-AMC, ixazomib, and 10% (w/v) glycerol. Control (0) is a sample free from ixazomib.

For better elucidation, ITC measurements (Figure 57) added a complementary perspective. In this case, the curve has a traditional "S" shape, and a second region of enthalpy variation could not be observed. This antagonist behavior can be explained because glycerol optimizes already the geometry of the catalytic region. Then, the same positive contribution exerted by ixazomib in ClpP without that compound does not exist anymore.
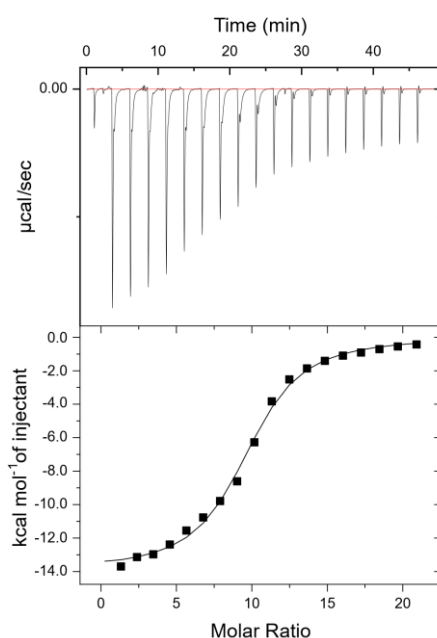
Figure 57 – ITC measurements with different ixazomib concentrations added to a ClpP sample supplemented by 10% (w/v) glycerol. After curve fitting, the following parameters were calculated: N = 9.53 ±0.0993 sites, K = 1.86E5 ±1.99E4 M^{-1}, ΔH= -1.390E4 ±198.0 cal/mol, and ΔS= -20.8 cal/mol/deg.

5. Conclusions

The present work contributes to the understanding of the ClpP modulation by boron-based compounds. Given the chemical properties of boron, boron-containing drugs have an intense appeal in healthcare research, especially when it comes to controlling undesirable enzymatic activities. This kind of ligand has arisen as efficient inhibitors capable of promiscuously binding to different proteases.

Since 2019, it has been known that peptidomimetic boronates cause an unexpected modulation of ClpP activity. At that point, data was demonstrated to elaborate answers to the observations, but no explanation, at atomic level, was provided in a sufficient manner. Now, with *Se*ClpP-ixazomib complex, it was possible to visualize not only the interaction restricted to the catalytic sites, but also how the orientation of a key and remote amino acid residue, Asn42, varies, signalizing the activation of proteolysis. At the first time, *Se*ClpP-peptidomimetic boronate and the active mutant *Sa*ClpP Y63A were compared, and the similarity of two distinct activation pathways could be attested.

The present study also shows how important the peptidomimetic portion is for triggering the modulation process. This part is essential for the geometric organization of the catalytic site.

Apart from the ClpP function, an oligomerization shift induced by ixazomib was identified. This ligand interacts with amino acid residues crucial for the protein oligomerization and function. In this scenario, SEC-SAXS data showed the predominance of the 14-mer structure in samples with the drug because of the assembly of the barrel-like structure from its tetradecamers. Besides that, the dimensionless plots based on this low-resolution approach unveiled an orchestrated structural extension characteristic of open ClpPs capable of degrading globular proteins in a dysregulated fashion. The stabilization of this state bound to ixazomib explains why, in experiments with SDS-PAGE, it was possible to see the decomposition of β-casein.

The part referring to the use of glycerol also brings important conclusions to studies on ClpP. The use of this triol indicates that the sample environment can influence the interpretation about the interaction between the protein and drug. The addition of a simple compound, such as a precipitant agent like MPD, results in

interferences in the enzyme's geometry and, consequently, the outcomes obtained from ClpP-ligand complexes. According to this perspective, it is recommended to use buffer with chemical chaperones, or even with different physicochemical conditions, to make better conclusions related to structure and functional features of ClpP modulated by drugs of interest.

The available results have raised some relevant queries, too. Is it possible to observe a synergy between canonical activators and peptidomimetic boronate? Assays with ONC206 and ixazomib, or bortezomib, could give some insights into any cooperation between those two types of activators, maybe proving the existence of a new pathway for the dysregulation of ClpP proteolytic activity.

Finally, adopting ClpP microcrystals (Figure 58) in time-resolved serial crystallography is a possible strategy to analyze the kinetics behind the binding process with peptidomimetic boronates and ClpP. This way, the dynamics of structural changes could be more explicit, providing valuable information for the development of novel scaffolds for the design of drugs capable of treating microbial infections, no matter if the responsible strain is multi-drug resistant or protected by biofilms.
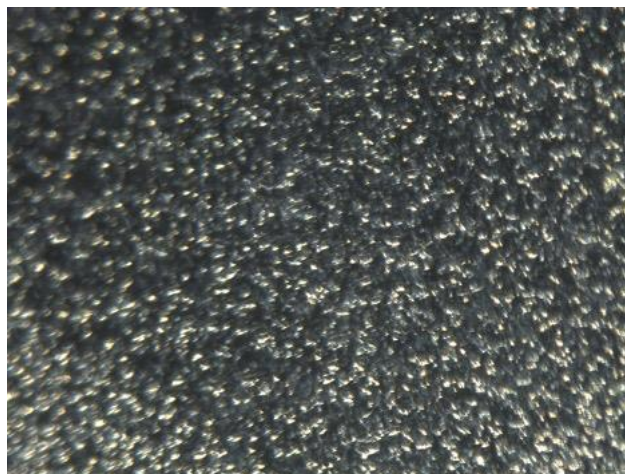
Figure 58 – Microcrystals of native *Se*ClpP suitable for time-resolved serial crystallography.

6. References

Abramson, Josh; Adler, Jonas; Dunger, Jack; Evans, Richard; Green, Tim; Pritzel, Alexander et al. (2024): Accurate structure prediction of biomolecular interactions with AlphaFold 3. In *Nature* 630 (8016), pp. 493–500. DOI: 10.1038/s41586-024-07487-w.

Adams, Paul D.; Afonine, Pavel V.; Bunkóczi, Gábor; Chen, Vincent B.; Davis, Ian W.; Echols, Nathaniel et al. (2010): PHENIX: a comprehensive Python-based system for macromolecular structure solution. In *Acta crystallographica. Section D, Biological crystallography* 66 (Pt 2), pp. 213–221. DOI: 10.1107/S0907444909052925.

Adnan, Mohd; Morton, Glyn; Singh, Jaipaul; Hadi, Sibte (2010): Contribution of rpoS and bolA genes in biofilm formation in Escherichia coli K-12 MG1655. In *Molecular and cellular biochemistry* 342 (1-2), pp. 207–213. DOI: 10.1007/s11010-010-0485-7.

Afonine, Pavel V.; Grosse-Kunstleve, Ralf W.; Echols, Nathaniel; Headd, Jeffrey J.; Moriarty, Nigel W.; Mustyakimov, Marat et al. (2012): Towards automated crystallographic structure refinement with phenix.refine. In *Acta crystallographica. Section D, Biological crystallography* 68 (Pt 4), pp. 352–367. DOI: 10.1107/S0907444912001308.

Akopian, Tatos; Kandror, Olga; Raju, Ravikiran M.; Unnikrishnan, Meera; Rubin, Eric J.; Goldberg, Alfred L. (2012): The active ClpP protease from M. tuberculosis is a complex composed of a heptameric ClpP1 and a ClpP2 ring. In *The EMBO Journal* 31 (6), pp. 1529–1541. DOI: 10.1038/emboj.2012.5.

Alexopoulos, John A.; Guarné, Alba; Ortega, Joaquin (2012): ClpP: a structurally dynamic protease regulated by AAA+ proteins. In *Journal of structural biology* 179 (2), pp. 202–210. DOI: 10.1016/j.jsb.2012.05.003.

Aljghami, Mazen E.; Barghash, Marim M.; Majaesic, Emily; Bhandari, Vaibhav; Houry, Walid A. (2022): Cellular functions of the ClpP protease impacting bacterial virulence. In *Frontiers in Molecular Biosciences* 9. DOI: 10.3389/fmolb.2022.1054408.

Alves França, Bruno; Falke, Sven; Rohde, Holger; Betzel, Christian (2024): Molecular insights into the dynamic modulation of bacterial ClpP function and oligomerization by peptidomimetic boronate compounds. In *Scientific Reports* 14. DOI: 10.1038/s41598-024-51787-0.

Anderson, Michael; Panteli, Dimitra; van Kessel, Robin; Ljungqvist, Gunnar; Colombo, Francesca; Mossialos, Elias (2023): Challenges and opportunities for incentivising antibiotic research and development in Europe. In *The Lancet regional health. Europe* 33, p. 100705. DOI: 10.1016/j.lanepe.2023.100705.

Antoñanzas, F.; Goossens, H. (2019): The economics of antibiotic resistance: a claim for personalised treatments. In *The European journal of health economics : HEPAC : health economics in prevention and care* 20 (4), pp. 483–485. DOI: 10.1007/s10198-018-1021-z.

Appelbaum, P. C. (2006): The emergence of vancomycin-intermediate and vancomycin-resistant Staphylococcus aureus. In *Clinical microbiology and infection : the official publication of the European Society of Clinical Microbiology and Infectious Diseases* 12 Suppl 1, pp. 16–23. DOI: 10.1111/j.1469-0691.2006.01344.x.

Arvanitis, Marios; Li, Gang; Li, De-Dong; Cotnoir, Daniel; Ganley-Leal, Lisa; Carney, Daniel W. et al. (2016): A Conformationally Constrained Cyclic Acyldepsipeptide Is Highly Effective in Mice Infected with Methicillin-Susceptible and -Resistant

Staphylococcus aureus. In *PloS one* 11 (4), e0153912. DOI: 10.1371/journal.pone.0153912.

Baird-Parker, A. C. (1990): The staphylococci: an introduction. In *Society for Applied Bacteriology symposium series* 19, 1S-8S. DOI: 10.1111/j.1365-2672.1990.tb01793.x.

Baran, Aleksandra; Kwiatkowska, Aleksandra; Potocki, Leszek (2023): Antibiotics and Bacterial Resistance-A Short Story of an Endless Arms Race. In *International journal of molecular sciences* 24 (6). DOI: 10.3390/ijms24065777.

Basso, Fernanda G.; Oliveira, Camila F.; Fontana, Amanda; Kurachi, Cristina; Bagnato, Vanderlei S.; Spolidório, Denise M. P. et al. (2011): In Vitro effect of low-level laser therapy on typical oral microbial biofilms. In *Brazilian dental journal* 22 (6), pp. 502–510. DOI: 10.1590/s0103-64402011000600011.

Baumann, Adam R.; Martin, Scott E.; Feng, Hao (2009): Removal of Listeria monocytogenes biofilms from stainless steel by use of ultrasound and ozone. In *Journal of food protection* 72 (6), pp. 1306–1309. DOI: 10.4315/0362-028x-72.6.1306.

Bazire, Alexis; Shioya, Kouki; Soum-Soutéra, Emmanuelle; Bouffartigues, Emeline; Ryder, Cynthia; Guentas-Dombrowsky, Linda et al. (2010): The Sigma Factor AlgU Plays a Key Role in Formation of Robust Biofilms by Nonmucoid Pseudomonas aeruginosa▿. In *Journal of Bacteriology* 192 (12), pp. 3001–3010. DOI: 10.1128/JB.01633-09.

Bhandari, Vaibhav; Wong, Keith S.; Zhou, Jin Lin; Mabanglo, Mark F.; Batey, Robert A.; Houry, Walid A. (2018): The Role of ClpP Protease in Bacterial Pathogenesis and Human Diseases. In *ACS chemical biology* 13 (6), pp. 1413–1425. DOI: 10.1021/acschembio.8b00124.

Bittrich, Sebastian; Segura, Joan; Duarte, Jose M.; Burley, Stephen K.; Rose, Yana (2024): RCSB protein Data Bank: exploring protein 3D similarities via comprehensive structural alignments. In *Bioinformatics (Oxford, England)* 40 (6). DOI: 10.1093/bioinformatics/btae370.

Blanchet, Clement E.; Svergun, Dmitri I. (2013): Small-angle X-ray scattering on biological macromolecules and nanocomposites in solution. In *Annual review of physical chemistry* 64, pp. 37–54. DOI: 10.1146/annurev-physchem-040412-110132.

Bonvini, P.; Zorzi, E.; Basso, G.; Rosolen, A. (2007): Bortezomib-mediated 26S proteasome inhibition causes cell-cycle arrest and induces apoptosis in CD-30+ anaplastic large cell lymphoma. In *Leukemia* 21 (4), pp. 838–842. DOI: 10.1038/sj.leu.2404528.

Bras, Wim; Koizumi, Satoshi; Terrill, Nicholas J. (2014): Beyond simple small-angle X-ray scattering: developments in online complementary techniques and sample environments. In *IUCrJ* 1 (Pt 6), pp. 478–491. DOI: 10.1107/S2052252514019198.

Brosey, Chris A.; Tainer, John A. (2019): Evolving SAXS versatility: solution X-ray scattering for macromolecular architecture, functional landscapes, and integrative structural biology. In *Current opinion in structural biology* 58, pp. 197–213. DOI: 10.1016/j.sbi.2019.04.004.

Bross, Peter F.; Kane, Robert; Farrell, Ann T.; Abraham, Sophia; Benson, Kimberly; Brower, Margaret E. et al. (2004): Approval summary for bortezomib for injection in the treatment of multiple myeloma. In *Clinical cancer research : an official journal of the American Association for Cancer Research* 10 (12 Pt 1), pp. 3954–3964. DOI: 10.1158/1078-0432.CCR-03-0781.

Brown Gandt, Autumn; Griffith, Elizabeth C.; Lister, Ida M.; Billings, Lisa L.; Han, Angel; Tangallapally, Rajendra et al. (2018): In Vivo and In Vitro Effects of a ClpP-Activating Antibiotic against Vancomycin-Resistant Enterococci. In *Antimicrobial agents and chemotherapy* 62 (8). DOI: 10.1128/AAC.00424-18.

Brunelle, Julie L.; Green, Rachel (2014): One-dimensional SDS-polyacrylamide gel electrophoresis (1D SDS-PAGE). In *Methods in enzymology* 541, pp. 151–159. DOI: 10.1016/B978-0-12-420119-4.00012-4.

Burley, Stephen K.; Wu-Wu, Amy; Dutta, Shuchismita; Ganesan, Shridar; Zheng, Steven X. F. (2024): Impact of structural biology and the protein data bank on us fda new drug approvals of low molecular weight antineoplastic agents 2019–2023. In *Oncogene* 43 (29), pp. 2229–2243. DOI: 10.1038/s41388-024-03077-2.

Bushby, S. R.; Hitchings, G. H. (1968): Trimethoprim, a sulphonamide potentiator. In *British Journal of Pharmacology and Chemotherapy* 33 (1), pp. 72–90.

Carugo, Oliviero; Djinovic-Carugo, Kristina (2013): Half a century of Ramachandran plots. In *Acta crystallographica. Section D, Biological crystallography* 69 (Pt 8), pp. 1333–1341. DOI: 10.1107/S090744491301158X.

Center for Disease Control and Prevention (2024): About antimicrobial resistance. https://www.cdc.gov/antimicrobial-resistance/about/

Chambers, H. F. (1997): Methicillin resistance in staphylococci: molecular and biochemical basis and clinical implications. In *Clinical microbiology reviews* 10 (4), pp. 781–791. DOI: 10.1128/CMR.10.4.781.

Chambers, H. F. (2001): The changing epidemiology of Staphylococcus aureus? In *Emerging Infectious Diseases* 7 (2), pp. 178–182.

Charzewski, Łukasz; Krzyśko, Krystiana A.; Lesyng, Bogdan (2021): Exploring Covalent Docking Mechanisms of Boron-Based Inhibitors to Class A, C and D β-Lactamases Using Time-dependent Hybrid QM/MM Simulations. In *Frontiers in Molecular Biosciences* 8, p. 633181. DOI: 10.3389/fmolb.2021.633181.

Chen, Vincent B.; Arendall, W. Bryan; Headd, Jeffrey J.; Keedy, Daniel A.; Immormino, Robert M.; Kapral, Gary J. et al. (2010): MolProbity: all-atom structure validation for macromolecular crystallography. In *Acta crystallographica. Section D, Biological crystallography* 66 (Pt 1), pp. 12–21. DOI: 10.1107/S0907444909042073.

Chin, Kah Wei; Michelle Tiong, Hui Ling; Luang-In, Vijitra; Ma, Nyuk Ling (2023): An overview of antibiotic and antibiotic resistance. In *Environmental Advances* 11, p. 100331. DOI: 10.1016/j.envadv.2022.100331.

Clancy, Megan; Graepler, Amy; Wilson, Michael; Douglas, Ivor; Johnson, Jeff; Price, Connie Savor (2006): Active screening in high-risk units is an effective and cost-avoidant method to reduce the rate of methicillin-resistant Staphylococcus aureus infection in the hospital. In *Infection control and hospital epidemiology* 27 (10), pp. 1009–1017. DOI: 10.1086/507915.

Coates, Anthony R. M.; Halls, Gerry; Hu, Yanmin (2011): Novel classes of antibiotics or more of the same? In *British journal of pharmacology* 163 (1), pp. 184–194. DOI: 10.1111/j.1476-5381.2011.01250.x.

Cobb, Leah H.; Park, JooYoun; Swanson, Elizabeth A.; Beard, Mary Catherine; McCabe, Emily M.; Rourke, Anna S. et al. (2019): CRISPR-Cas9 modified bacteriophage for treatment of Staphylococcus aureus induced osteomyelitis and soft tissue infection. In *PloS one* 14 (11), e0220421. DOI: 10.1371/journal.pone.0220421.

Cohen, M. L. (1986): Staphylococcus aureus: biology, mechanisms of virulence, epidemiology. In *The Journal of pediatrics* 108 (5 Pt 2), pp. 796–799. DOI: 10.1016/s0022-3476(86)80747-8.

Conlon, B. P.; Nakayasu, E. S.; Fleck, L. E.; LaFleur, M. D.; Isabella, V. M.; Coleman, K. et al. (2013): Activated ClpP kills persisters and eradicates a chronic biofilm infection. In *Nature* 503 (7476), pp. 365–370. DOI: 10.1038/nature12790.

Crowe, J.; Masone, B. S.; Ribbe, J. (1996): One-step purification of recombinant proteins with the 6xHis tag and Ni-NTA resin. In *Methods in molecular biology (Clifton, N.J.)* 58, pp. 491–510. DOI: 10.1385/0-89603-402-X:491.

Culp, Elizabeth; Wright, Gerard D. (2017): Bacterial proteases, untapped antimicrobial drug targets. In *The Journal of antibiotics* 70 (4), pp. 366–377. DOI: 10.1038/ja.2016.138.

Da Re, Sandra; Ghigo, Jean-Marc (2006): A CsgD-independent pathway for cellulose production and biofilm formation in Escherichia coli. In *Journal of Bacteriology* 188 (8), pp. 3073–3087. DOI: 10.1128/JB.188.8.3073-3087.2006.

D'Agata, Erika M. C.; Magal, Pierre; Olivier, Damien; Ruan, Shigui; Webb, Glenn F. (2007): Modeling antibiotic resistance in hospitals: the impact of minimizing treatment duration. In *Journal of theoretical biology* 249 (3), pp. 487–499. DOI: 10.1016/j.jtbi.2007.08.011.

Di Domenico, Enea Gino; Oliva, Alessandra; Guembe, María (2022): The Current Knowledge on the Pathogenesis of Tissue and Medical Device-Related Biofilm Infections. In *Microorganisms* 10 (7). DOI: 10.3390/microorganisms10071259.

Di Franco, Sveva; Alfieri, Aniello; Pace, Maria Caterina; Sansone, Pasquale; Pota, Vincenzo; Fittipaldi, Ciro et al. (2021): Blood Stream Infections from MDR Bacteria. In *Life* 11 (6). DOI: 10.3390/life11060575.

Diaz, Diego B.; Yudin, Andrei K. (2017): The versatility of boron in biological target engagement. In *Nature chemistry* 9 (8), pp. 731–742. DOI: 10.1038/nchem.2814.

Diedrich, Konrad; Ehrt, Christiane; Graef, Joel; Poppinga, Martin; Ritter, Norbert; Rarey, Matthias (2024): User-centric design of a 3D search interface for protein-ligand complexes. In *Journal of computer-aided molecular design* 38 (1), p. 23. DOI: 10.1007/s10822-024-00563-3.

Donlan, Rodney M. (2002): Biofilms: microbial life on surfaces. In *Emerging Infectious Diseases* 8 (9), pp. 881–890. DOI: 10.3201/eid0809.020063.

Edwards, Suzanne E.; Morel, Chantal M.; Busse, Reinhard; Harbarth, Stephan (2018): Combatting Antibiotic Resistance Together: How Can We Enlist the Help of Industry? In *Antibiotics (Basel, Switzerland)* 7 (4). DOI: 10.3390/antibiotics7040111.

Eiff, Christof von; Peters, Georg; Heilmann, Christine (2002): Pathogenesis of infections due to coagulase-negative staphylococci. In *The Lancet. Infectious diseases* 2 (11), pp. 677–685. DOI: 10.1016/s1473-3099(02)00438-3.

EMBL (2024): P12 beamline. https://www.embl-hamburg.de/biosaxs/p12/

EMBL-BIOSAXS (2024): Technical characteristics of beamline P12. https://www.embl-hamburg.de/biosaxs/p12/characteristics.html

Emsley, Paul; Cowtan, Kevin (2004): Coot: model-building tools for molecular graphics. In *Acta crystallographica. Section D, Biological crystallography* 60, pp. 2126–2132. DOI: 10.1107/S0907444904019158.

European Centre for Disease Prevention and Control and World Health Organization (2023): Antimicrobial resistance surveillance in Europe 2023 - 2021 data. https://www.ecdc.europa.eu/en/publications-data/

Falke, Sven; Betzel, Christian (2019): Dynamic Light Scattering (DLS). In Alice S. Pereira, Pedro Tavares, Paulo Limão-Vieira (Eds.): Radiation in bioanalysis. Spectroscopic techniques and theoretical methods, vol. 8. Cham: Springer (Bioanalysis : advanced materials, methods, and devices, volume 8), pp. 173–193.

Fei, Xue; Bell, Tristan A.; Jenni, Simon; Stinson, Benjamin M.; Baker, Tania A.; Harrison, Stephen C.; Sauer, Robert T. (2020): Structures of the ATP-fueled ClpXP proteolytic machine bound to protein substrate. In *eLife* 9. DOI: 10.7554/eLife.52774.

Felix, Jan; Weinhäupl, Katharina; Chipot, Christophe; Dehez, François; Hessel, Audrey; Gauto, Diego F. et al. (2019): Mechanism of the allosteric activation of the ClpP protease machinery by substrates and active-site inhibitors. In *Science advances* 5 (9), eaaw3818. DOI: 10.1126/sciadv.aaw3818.

Feng, Ying; Wang, Hongyuan; Lu, H. E.; Yi, Liu; Hong, L. I. (2021): Effects of ClpP protease on biofilm formation of Enterococcus faecalis. In *Journal of applied oral science : revista FOB* 29, e20200733. DOI: 10.1590/1678-7757-2020-0733.

Fernandes, Guilherme Felipe Santos; Denny, William Alexander; Dos Santos, Jean Leandro (2019): Boron in drug design: Recent advances in the development of new therapeutic agents. In *European journal of medicinal chemistry* 179, pp. 791–804. DOI: 10.1016/j.ejmech.2019.06.092.

Foster, Timothy J. (2017): Antibiotic resistance in Staphylococcus aureus. Current status and future prospects. In *FEMS microbiology reviews* 41 (3), pp. 430–449. DOI: 10.1093/femsre/fux007.

Fournière, Mathilde; Latire, Thomas; Souak, Djouhar; Feuilloley, Marc G. J.; Bedoux, Gilles (2020): Staphylococcus epidermidis and Cutibacterium acnes: Two Major Sentinels of Skin Microbiota and the Influence of Cosmetics. In *Microorganisms* 8 (11). DOI: 10.3390/microorganisms8111752.

Franke, Daniel; Jeffries, Cy M.; Svergun, Dmitri I. (2015): Correlation Map, a goodness-of-fit test for one-dimensional X-ray scattering spectra. In *Nature methods* 12 (5), pp. 419–422. DOI: 10.1038/nmeth.3358.

Franke, Daniel; Svergun, Dmitri I. (2009): DAMMIF, a program for rapid ab-initio shape determination in small-angle scattering. In *Journal of applied crystallography* 42 (Pt 2), pp. 342–346. DOI: 10.1107/S0021889809000338.

Frees, D.; Ingmer, H. (1999): ClpP participates in the degradation of misfolded protein in Lactococcus lactis. In *Molecular microbiology* 31 (1), pp. 79–87. DOI: 10.1046/j.1365-2958.1999.01149.x.

Frees, Dorte; Brøndsted, Lone; Ingmer, Hanne (2013): Bacterial proteases and virulence. In *Sub-cellular biochemistry* 66, pp. 161–192. DOI: 10.1007/978-94-007-5940-4_7.

Frees, Dorte; Sørensen, Karen; Ingmer, Hanne (2005): Global virulence regulation in Staphylococcus aureus: pinpointing the roles of ClpP and ClpX in the sar/agr regulatory network. In *Infection and immunity* 73 (12), pp. 8100–8108. DOI: 10.1128/IAI.73.12.8100-8108.2005.

Gaillot, O.; Pellegrini, E.; Bregenholt, S.; Nair, S.; Berche, P. (2000): The ClpP serine protease is essential for the intracellular parasitism and virulence of Listeria monocytogenes. In *Molecular microbiology* 35 (6), pp. 1286–1294. DOI: 10.1046/j.1365-2958.2000.01773.x.

Garcia, Dioscaris R.; Deckey, David; Haglin, Jack M.; Emanuel, Toby; Mayfield, Cory; Eltorai, Adam E. M. et al. (2019): Commonly Encountered Skin Biome-Derived Pathogens after Orthopedic Surgery. In *Surgical infections* 20 (5), pp. 341–350. DOI: 10.1089/sur.2018.161.

Gersch, Malte; Famulla, Kirsten; Dahmen, Maria; Göbl, Christoph; Malik, Imran; Richter, Klaus et al. (2015): AAA+ chaperones and acyldepsipeptides activate the ClpP protease via conformational control. In *Nature communications* 6, p. 6320. DOI: 10.1038/ncomms7320.

Gersch, Malte; Kolb, Roman; Alte, Ferdinand; Groll, Michael; Sieber, Stephan A. (2014a): Disruption of oligomerization and dehydroalanine formation as mechanisms for ClpP protease inhibition. In *Journal of the American Chemical Society* 136 (4), pp. 1360–1366. DOI: 10.1021/ja4082793.

Gersch, Malte; Kolb, Roman; Alte, Ferdinand; Groll, Michael; Sieber, Stephan A. (2014b): Disruption of oligomerization and dehydroalanine formation as mechanisms for ClpP protease inhibition. In *Journal of the American Chemical Society* 136 (4), pp. 1360–1366. DOI: 10.1021/ja4082793.

Gersch, Malte; List, Anja; Groll, Michael; Sieber, Stephan A. (2012): Insights into structural network responsible for oligomerization and activity of bacterial virulence regulator caseinolytic protease P (ClpP) protein. In *The Journal of biological chemistry* 287 (12), pp. 9484–9494. DOI: 10.1074/jbc.M111.336222.

Ghooi, R. B.; Thatte, S. M. (1995): Inhibition of cell wall synthesis--is this the mechanism of action of penicillins? In *Medical hypotheses* 44 (2), pp. 127–131. DOI: 10.1016/0306-9877(95)90085-3.

Goodreid, Jordan D.; Wong, Keith; Leung, Elisa; McCaw, Shannon E.; Gray-Owen, Scott D.; Lough, Alan et al. (2014): Total synthesis and antibacterial testing of the A54556 cyclic acyldepsipeptides isolated from Streptomyces hawaiiensis. In *Journal of natural products* 77 (10), pp. 2170–2181. DOI: 10.1021/np500158q.

Grams, R. Justin; Santos, Webster L.; Scorei, Ion Romulus; Abad-García, Antonio; Rosenblum, Carol Ann; Bita, Andrei et al. (2024): The Rise of Boron-Containing Compounds: Advancements in Synthesis, Medicinal Chemistry, and Emerging Pharmacology. In *Chemical reviews* 124 (5), pp. 2441–2511. DOI: 10.1021/acs.chemrev.3c00663.

Gräwert, Tobias W.; Svergun, Dmitri I. (2020): Structural Modeling Using Solution Small-Angle X-ray Scattering (SAXS). In *Journal of molecular biology* 432 (9), pp. 3078–3092. DOI: 10.1016/j.jmb.2020.01.030.

Griffith, Elizabeth C.; Zhao, Ying; Singh, Aman P.; Conlon, Brian P.; Tangallapally, Rajendra; Shadrick, William R. et al. (2019): Ureadepsipeptides as ClpP Activators. In *ACS infectious diseases* 5 (11), pp. 1915–1925. DOI: 10.1021/acsinfecdis.9b00245.

Guo, Qiao; Kong, Weina; Jin, Sheng; Chen, Lin; Xu, Yangyang; Duan, Kangmin (2014): PqsR-dependent and PqsR-independent regulation of motility and biofilm formation by PQS in Pseudomonas aeruginosa PAO1. In *Journal of basic microbiology* 54 (7), pp. 633–643. DOI: 10.1002/jobm.201300091.

Guo, Xinyan; Xiaojun, Lv; Zhang, Aiguo; Yan, Zheng; Chen, Siyi; Wang, Na (2020): Antibiotic contamination in a typical water-rich city in southeast China: a concern for drinking water resource safety. In *Journal of environmental science and health. Part. B, Pesticides, food contaminants, and agricultural wastes* 55 (3), pp. 193–209. DOI: 10.1080/03601234.2019.1679563.

Gupta, Neeraj; Hanley, Michael J.; Xia, Cindy; Labotka, Richard; Harvey, R. Donald; Venkatakrishnan, Karthik (2019): Clinical Pharmacology of Ixazomib: The First Oral Proteasome Inhibitor. In *Clinical pharmacokinetics* 58 (4), pp. 431–449. DOI: 10.1007/s40262-018-0702-1.

Halawa, Esraa M.; Fadel, Mohamed; Al-Rabia, Mohammed W.; Behairy, Ali; Nouh, Nehal A.; Abdo, Mohamed et al. (2023): Antibiotic action and resistance: updated review of mechanisms, spread, influencing factors, and alternative approaches for combating resistance. In *Frontiers in pharmacology* 14, p. 1305294. DOI: 10.3389/fphar.2023.1305294.

Hassan, Puthusserickal A.; Rana, Suman; Verma, Gunjan (2015): Making sense of Brownian motion: colloid characterization by dynamic light scattering. In *Langmuir : the ACS journal of surfaces and colloids* 31 (1), pp. 3–12. DOI: 10.1021/la501789z.

Hiramatsu, K. (2001): Vancomycin-resistant Staphylococcus aureus: a new model of antibiotic resistance. In *The Lancet. Infectious diseases* 1 (3), pp. 147–155. DOI: 10.1016/S1473-3099(01)00091-3.

Hoffman, Steven J.; Caleo, Grazia M.; Daulaire, Nils; Elbe, Stefan; Matsoso, Precious; Mossialos, Elias et al. (2015): Strategies for achieving global collective action on antimicrobial resistance. In *Bulletin of the World Health Organization* 93 (12), pp. 867–876. DOI: 10.2471/BLT.15.153171.

Høiby, Niels; Bjarnsholt, Thomas; Givskov, Michael; Molin, Søren; Ciofu, Oana (2010): Antibiotic resistance of bacterial biofilms. In *International Journal of Antimicrobial Agents* 35 (4), pp. 322–332. DOI: 10.1016/j.ijantimicag.2009.12.011.

Hooper, D. C. (2000): Mechanisms of action and resistance of older and newer fluoroquinolones. In *Clinical Infectious Diseases* 31 (Supplement_2), S24-S28.

Hoskins, J. R.; Kim, S. Y.; Wickner, S. (2000): Substrate recognition by the ClpA chaperone component of ClpAP protease. In *The Journal of biological chemistry* 275 (45), pp. 35361–35367. DOI: 10.1074/jbc.M006288200.

Humphreys, C. J. (2013): The significance of Bragg's law in electron diffraction and microscopy, and Bragg's second law. In *Acta crystallographica. Section A, Foundations of crystallography* 69 (Pt 1), pp. 45–50. DOI: 10.1107/S0108767312047587.

Hura, Greg L.; Menon, Angeli L.; Hammel, Michal; Rambo, Robert P.; Poole, Farris L.; Tsutakawa, Susan E. et al. (2009): Robust, high-throughput solution structural analyses by small angle X-ray scattering (SAXS). In *Nature methods* 6 (8), pp. 606–612. DOI: 10.1038/nmeth.1353.

Hwang, Seung-Ho; Im, Hanhyeok; Choi, Sang Ho (2021): A Master Regulator BrpR Coordinates the Expression of Multiple Loci for Robust Biofilm and Rugose Colony Development in Vibrio vulnificus. In *Frontiers in Microbiology* 12. DOI: 10.3389/fmicb.2021.679854.

Jackson, David G.; Cardwell, Leah A.; Oussedik, Elias; Feldman, Steven R. (2020): Utility of boron in dermatology. In *The Journal of dermatological treatment* 31 (1), pp. 2–12. DOI: 10.1080/09546634.2017.1363850.

Jacques, Samuel; van der Sloot, Almer M.; C. Huard, Caroline; Coulombe-Huntington, Jasmin; Tsao, Sarah; Tollis, Sylvain et al. (2020): Imipridone Anticancer Compounds Ectopically Activate the ClpP Protease and Represent a New Scaffold for Antibiotic Development. In *Genetics* 214 (4), pp. 1103–1120. DOI: 10.1534/genetics.119.302851.

Jin, Lin; Jarand, Curtis W.; Brader, Mark L.; Reed, Wayne F. (2022): Angle-dependent effects in DLS measurements of polydisperse particles. In *Meas. Sci. Technol.* 33 (4), p. 45202. DOI: 10.1088/1361-6501/ac42b2.

Joshi, Shilpa A.; Hersch, Greg L.; Baker, Tania A.; Sauer, Robert T. (2004): Communication between ClpX and ClpP during substrate processing and degradation. In *Nature structural & molecular biology* 11 (5), pp. 404–411. DOI: 10.1038/nsmb752.

Ju, Yuan; He, Lihui; Zhou, Yuanzheng; Yang, Tao; Sun, Ke; Song, Rao et al. (2020): Discovery of Novel Peptidomimetic Boronate ClpP Inhibitors with Noncanonical Enzyme Mechanism as Potent Virulence Blockers in Vitro and in Vivo. In *Journal of medicinal chemistry* 63 (6), pp. 3104–3119. DOI: 10.1021/acs.jmedchem.9b01746.

Kaldas, Sherif J.; Rogova, Tatiana; Nenajdenko, Valentine G.; Yudin, Andrei K. (2018): Modular Synthesis of β-Amino Boronate Peptidomimetics. In *The Journal of organic chemistry* 83 (13), pp. 7296–7302. DOI: 10.1021/acs.joc.8b00325.

Kang, Sung Gyun; Dimitrova, Mariana N.; Ortega, Joaquin; Ginsburg, Ann; Maurizi, Michael R. (2005): Human mitochondrial ClpP is a stable heptamer that assembles into a tetradecamer in the presence of ClpX. In *The Journal of biological chemistry* 280 (42), pp. 35424–35432. DOI: 10.1074/jbc.M507240200.

Kang, Sung Gyun; Maurizi, Michael R.; Thompson, Mark; Mueser, Timothy; Ahvazi, Bijan (2004): Crystallography and mutagenesis point to an essential role for the N-terminus of human mitochondrial ClpP. In *Journal of structural biology* 148 (3), pp. 338–352. DOI: 10.1016/j.jsb.2004.07.004.

Kaplan, Gulce Sari; Torcun, Ceyda Corek; Grune, Tilman; Ozer, Nesrin Kartal; Karademir, Betul (2017): Proteasome inhibitors in cancer therapy: Treatment regimen and peripheral neuropathy as a side effect. In *Free radical biology & medicine* 103, pp. 1–13. DOI: 10.1016/j.freeradbiomed.2016.12.007.

Kaplan, J. B. (2010): Biofilm dispersal: mechanisms, clinical implications, and potential therapeutic uses. In *Journal of dental research* 89 (3), pp. 205–218. DOI: 10.1111/j.1365-2958.2009.06793.x.

Katikaridis, Panagiotis; Bohl, Valentin; Mogk, Axel (2021): Resisting the Heat: Bacterial Disaggregases Rescue Cells From Devastating Protein Aggregation. In *Frontiers in Molecular Biosciences* 8, p. 681439. DOI: 10.3389/fmolb.2021.681439.

Khan, Muhammad Farooq Saleem; Akbar, Mona; Wu, Jing; Xu, Zhou (2021): A review on fluorescence spectroscopic analysis of water and wastewater. In *Methods and applications in fluorescence* 10 (1). DOI: 10.1088/2050-6120/ac3d79.

Khan, Saiqa I.; Blumrosen, Gaddi; Vecchio, Daniela; Golberg, Alexander; McCormack, Michael C.; Yarmush, Martin L. et al. (2016): Eradication of multidrug-resistant pseudomonas biofilm with pulsed electric fields. In *Biotechnology and bioengineering* 113 (3), pp. 643–650. DOI: 10.1002/bit.25818.

Khardori, Nancy; Stevaux, Cecilia; Ripley, Kathryn (2020): Antibiotics: From the Beginning to the Future: Part 2. In *Indian journal of pediatrics* 87 (1), pp. 43–47. DOI: 10.1007/s12098-019-03113-0.

Kim, Dong Young; Kim, Kyeong Kyu (2008): The structural basis for the activation and peptide recognition of bacterial ClpP. In *Journal of molecular biology* 379 (4), pp. 760–771. DOI: 10.1016/j.jmb.2008.04.036.

Kirstein, Janine; Molière, Noël; Dougan, David A.; Turgay, Kürşad (2009): Adapting the machine: adaptor proteins for Hsp100/Clp and AAA+ proteases. In *Nature reviews. Microbiology* 7 (8), pp. 589–599. DOI: 10.1038/nrmicro2185.

Kirstein, Janine; Schlothauer, Tilman; Dougan, David A.; Lilie, Hauke; Tischendorf, Gilbert; Mogk, Axel et al. (2006): Adaptor protein controlled oligomerization activates the AAA+ protein ClpC. In *The EMBO Journal* 25 (7), pp. 1481–1491. DOI: 10.1038/sj.emboj.7601042.

Kolár, M.; Urbánek, K.; Látal, T. (2001): Antibiotic selective pressure and development of bacterial resistance. In *International Journal of Antimicrobial Agents* 17 (5), pp. 357–363. DOI: 10.1016/s0924-8579(01)00317-x.

Kotov, Vadim; Mlynek, Georg; Vesper, Oliver; Pletzer, Marina; Wald, Jiri; Teixeira-Duarte, Celso M. et al. (2021): In-depth interrogation of protein thermal unfolding data with MoltenProt. In *Protein science : a publication of the Protein Society* 30 (1), pp. 201–217. DOI: 10.1002/pro.3986.

Kovach, Ildiko M. (2021): Proton Bridging in Catalysis by and Inhibition of Serine Proteases of the Blood Cascade System. In *Life* 11 (5). DOI: 10.3390/life11050396.

Krug, Michael; Weiss, Manfred S.; Heinemann, Udo; Mueller, Uwe (2012): XDSAPP : a graphical user interface for the convenient processing of diffraction data using XDS. In *J Appl Crystallogr* 45 (3), pp. 568–572. DOI: 10.1107/S0021889812011715.

Kwon, Jennie H.; Powderly, William G. (2021): The post-antibiotic era is here. In *Science (New York, N.Y.)* 373 (6554), p. 471. DOI: 10.1126/science.abl5997.

Lamret, Fabien; Colin, Marius; Mongaret, Céline; Gangloff, Sophie C.; Reffuveille, Fany (2020): Antibiotic Tolerance of Staphylococcus aureus Biofilm in Periprosthetic Joint Infections and Antibiofilm Strategies. In *Antibiotics (Basel, Switzerland)* 9 (9). DOI: 10.3390/antibiotics9090547.

Landecker, Hannah (2016): Antibiotic Resistance and the Biology of History. In *Body & society* 22 (4), pp. 19–52. DOI: 10.1177/1357034X14561341.

Larsen, Olaf F. A.; van der Grint, Maike; Wiegers, Cato; van de Burgwal, Linda H. M. (2022): The Gut Microbiota: Master of Puppets Connecting the Epidemiology of Infectious, Autoimmune, and Metabolic Disease. In *Frontiers in Microbiology* 13, p. 902106. DOI: 10.3389/fmicb.2022.902106.

Lavey, Nathan P.; Shadid, Tyler; Ballard, Jimmy D.; Duerfeldt, Adam S. (2018): Clostridium difficile ClpP Homologues are Capable of Uncoupled Activity and Exhibit Different Levels of Susceptibility to Acyldepsipeptide Modulation. In *ACS infectious diseases* 5 (1), pp. 79–89. DOI: 10.1021/acsinfecdis.8b00199.

Leclercq, Roland (2002): Mechanisms of resistance to macrolides and lincosamides: nature of the resistance elements and their clinical implications. In *Clinical infectious diseases : an official publication of the Infectious Diseases Society of America* 34 (4), pp. 482–492. DOI: 10.1086/324626.

Lee, Byung-Gil; Kim, Min Kyung; Song, Hyun Kyu (2011): Structural insights into the conformational diversity of ClpP from Bacillus subtilis. In *Molecules and cells* 32 (6), pp. 589–595. DOI: 10.1007/s10059-011-0197-1.

Lee, Byung-Gil; Park, Eun Young; Lee, Kyung-Eun; Jeon, Hyesung; Sung, Kwang Hoon; Paulsen, Holger et al. (2010a): Structures of ClpP in complex with acyldepsipeptide antibiotics reveal its activation mechanism. In *Nature structural & molecular biology* 17 (4), pp. 471–478. DOI: 10.1038/nsmb.1787.

Lee, Mary E.; Baker, Tania A.; Sauer, Robert T. (2010b): Control of substrate gating and translocation into ClpP by channel residues and ClpX binding. In *Journal of molecular biology* 399 (5), pp. 707–718. DOI: 10.1016/j.jmb.2010.04.027.

Levy, Stuart B.; Marshall, Bonnie (2004): Antibacterial resistance worldwide: causes, challenges and responses. In *Nature medicine* 10 (12 Suppl), S122-9. DOI: 10.1038/nm1145.

Li, Yangxiong; Lavey, Nathan P.; Coker, Jesse A.; Knobbe, Jessica E.; Truong, Dat C.; Yu, Hongtao et al. (2017): Consequences of Depsipeptide Substitution on the ClpP Activation Activity of Antibacterial Acyldepsipeptides. In *ACS Medicinal Chemistry Letters* 8 (11), pp. 1171–1176. DOI: 10.1021/acsmedchemlett.7b00320.

Li, Yanping; Kumar, Suresh; Zhang, Lihu (2024): Mechanisms of Antibiotic Resistance and Developments in Therapeutic Strategies to Combat Klebsiella pneumoniae Infection. In *Infection and drug resistance* 17, pp. 1107–1119. DOI: 10.2147/IDR.S453025.

Liu, Kaiyin; Ologbenla, Adedeji; Houry, Walid A. (2014): Dynamics of the ClpP serine protease: a model for self-compartmentalized proteases. In *Critical reviews in biochemistry and molecular biology* 49 (5), pp. 400–412. DOI: 10.3109/10409238.2014.925421.

Liu, Qian; Wang, Xing; Qin, Juanxiu; Cheng, Sen; Yeo, Won-Sik; He, Lei et al. (2017): The ATP-Dependent Protease ClpP Inhibits Biofilm Formation by Regulating Agr and Cell Wall Hydrolase Sle1 in Staphylococcus aureus. In *Frontiers in cellular and infection microbiology* 7, p. 181. DOI: 10.3389/fcimb.2017.00181.

Livermore, D. M. (1995): beta-Lactamases in laboratory and clinical resistance. In *Clinical microbiology reviews* 8 (4), pp. 557–584. DOI: 10.1128/CMR.8.4.557.

Lyddiard, Dane; Jones, Graham L.; Greatrex, Ben W. (2016): Keeping it simple: lessons from the golden era of antibiotic discovery. In *FEMS microbiology letters* 363 (8). DOI: 10.1093/femsle/fnw084.

Mabanglo, Mark F.; Houry, Walid A. (2022): Recent structural insights into the mechanism of ClpP protease regulation by AAA+ chaperones and small molecules. In *The Journal of biological chemistry* 298 (5). DOI: 10.1016/j.jbc.2022.101781.

Mabanglo, Mark F.; Wong, Keith S.; Barghash, Marim M.; Leung, Elisa; Chuang, Stephanie H. W.; Ardalan, Afshan et al. (2023): Potent ClpP agonists with anticancer properties bind with improved structural complementarity and alter the mitochondrial N-terminome. In *Structure (London, England : 1993)* 31 (2), 185-200.e10. DOI: 10.1016/j.str.2022.12.002.

MacKenzie, Donald W. (2013): Applying the Anderson-Darling test to suicide clusters: evidence of contagion at U. S. universities? In *Crisis* 34 (6), pp. 434–437. DOI: 10.1027/0227-5910/a000197.

Makinde, Taiwo Mary; Ako-Nai, Kwashie Ajibade; Shittu, A. O. (2019): A study on the antibiotic susceptibility of Staphylococcus aureus from nasal samples of female students at the Obafemi Awolowo university campus. In *JMEN* 7 (2). DOI: 10.15406/jmen.2019.07.00246.

Malik, Imran T.; Pereira, Rebeca; Vielberg, Marie-Theres; Mayer, Christian; Straetener, Jan; Thomy, Dhana et al. (2020): Functional Characterisation of ClpP Mutations Conferring Resistance to Acyldepsipeptide Antibiotics in Firmicutes. In *Chembiochem* 21 (14), pp. 1997–2012. DOI: 10.1002/cbic.201900787.

Manalastas-Cantos, Karen; Konarev, Petr V.; Hajizadeh, Nelly R.; Kikhney, Alexey G.; Petoukhov, Maxim V.; Molodenskiy, Dmitry S. et al. (2021): ATSAS 3.0: expanded functionality and new tools for small-angle scattering data analysis. In *Journal of applied crystallography* 54 (Pt 1), pp. 343–355. DOI: 10.1107/S1600576720013412.

Martin, Andreas; Baker, Tania A.; Sauer, Robert T. (2007): Distinct static and dynamic interactions control ATPase-peptidase communication in a AAA+ protease. In *Molecular cell* 27 (1), pp. 41–52. DOI: 10.1016/j.molcel.2007.05.024.

Martin, Andreas; Baker, Tania A.; Sauer, Robert T. (2008): Diverse pore loops of the AAA+ ClpX machine mediate unassisted and adaptor-dependent recognition of ssrA-tagged substrates. In *Molecular cell* 29 (4), pp. 441–450. DOI: 10.1016/j.molcel.2008.02.002.

Maurizi, Michael R.; Di Xia (2004): Protein binding and disruption by Clp/Hsp100 chaperones. In *Structure (London, England : 1993)* 12 (2), pp. 175–183. DOI: 10.1016/j.str.2004.01.021.

Maxson, Tucker; Mitchell, Douglas A. (2016): Targeted Treatment for Bacterial Infections: Prospects for Pathogen-Specific Antibiotics Coupled with Rapid Diagnostics. In *Tetrahedron* 72 (25), pp. 3609–3624. DOI: 10.1016/j.tet.2015.09.069.

McDonald, Marguerite; Blondeau, Joseph M. (2010): Emerging antibiotic resistance in ocular infections and the role of fluoroquinolones. In *Journal of cataract and refractive surgery* 36 (9), pp. 1588–1598. DOI: 10.1016/j.jcrs.2010.06.028.

McLoughlin, Isabella J.; Wright, Eva M.; Tagg, John R.; Jain, Rohit; Hale, John D. F. (2022): Skin Microbiome-The Next Frontier for Probiotic Intervention. In *Probiotics and antimicrobial proteins* 14 (4), pp. 630–647. DOI: 10.1007/s12602-021-09824-1.

Ménard, R.; Storer, A. C. (1992): Oxyanion hole interactions in serine and cysteine proteases. In *Biological chemistry Hoppe-Seyler* 373 (7), pp. 393–400. DOI: 10.1515/bchm3.1992.373.2.393.

Mendelson, Marc; Lewnard, Joseph A.; Sharland, Mike; Cook, Aislinn; Pouwels, Koen B.; Alimi, Yewande et al. (2024): Ensuring progress on sustainable access to effective antibiotics at the 2024 UN General Assembly: a target-based approach. In *Lancet (London, England)*. DOI: 10.1016/S0140-6736(24)01019-5.

Micale, Nicola; Ettari, Roberta; Lavecchia, Antonio; Di Giovanni, Carmen; Scarbaci, Kety; Troiano, Valeria et al. (2013): Development of peptidomimetic boronates as proteasome inhibitors. In *European journal of medicinal chemistry* 64, pp. 23–34. DOI: 10.1016/j.ejmech.2013.03.032.

Micale, Nicola; Scarbaci, Kety; Troiano, Valeria; Ettari, Roberta; Grasso, Silvana; Zappalà, Maria (2014): Peptide-based proteasome inhibitors in anticancer drug design. In *Medicinal research reviews* 34 (5), pp. 1001–1069. DOI: 10.1002/med.21312.

Michels, Andreas; Malyeyev, Artem; Titov, Ivan; Honecker, Dirk; Cubitt, Robert; Blackburn, Elizabeth; Suzuki, Kiyonori (2020): Magnetic Guinier law. In *IUCrJ* 7 (Pt 1), pp. 136–142. DOI: 10.1107/S2052252519016439.

Minasyan, Hayk (2019): Sepsis: mechanisms of bacterial injury to the patient. In *Scandinavian journal of trauma, resuscitation and emergency medicine* 27 (1), p. 19. DOI: 10.1186/s13049-019-0596-4.

Mishra, Ratnesh Chandra; Grover, Anil (2016): ClpB/Hsp100 proteins and heat stress tolerance in plants. In *Critical reviews in biotechnology* 36 (5), pp. 862–874. DOI: 10.3109/07388551.2015.1051942.

Moreno-Cinos, Carlos; Goossens, Kenneth; Salado, Irene G.; van der Veken, Pieter; Winter, Hans de; Augustyns, Koen (2019): ClpP Protease, a Promising Antimicrobial Target. In *International journal of molecular sciences* 20 (9). DOI: 10.3390/ijms20092232.

Morgan, Rhodri M. L.; Pal, Mohinder; Roe, S. Mark; Pearl, Laurence H.; Prodromou, Chrisostomos (2015): Tah1 helix-swap dimerization prevents mixed Hsp90 co-

chaperone complexes. In *Acta crystallographica. Section D, Biological crystallography* 71 (Pt 5), pp. 1197–1206. DOI: 10.1107/S1399004715004551.

Mroue, Nader; Arya, Anu; Brown Gandt, Autumn; Russell, Cameron; Han, Angel; Gavrish, Ekaterina; LaFleur, Michael (2019): Pharmacodynamics of ClpP-Activating Antibiotic Combinations against Gram-Positive Pathogens. In *Antimicrobial agents and chemotherapy* 64 (1). DOI: 10.1128/AAC.01554-19.

Nakatsuji, Teruaki; Gallo, Richard L. (2018): The role of the skin microbiome in atopic dermatitis. In *Annals of allergy, asthma & immunology : official publication of the American College of Allergy, Asthma, & Immunology* 122 (3), pp. 263–269. DOI: 10.1016/j.anai.2018.12.003.

Nasrollahian, Sina; Graham, Jay P.; Halaji, Mehrdad (2024): A review of the mechanisms that confer antibiotic resistance in pathotypes of E. coli. In *Frontiers in cellular and infection microbiology* 14, p. 1387497. DOI: 10.3389/fcimb.2024.1387497.

Ni, Tengfeng; Ye, Fei; Liu, Xing; Zhang, Jie; Liu, Hongchuan; Li, Jiahui et al. (2016): Characterization of Gain-of-Function Mutant Provides New Insights into ClpP Structure. In *ACS chemical biology* 11 (7), pp. 1964–1972. DOI: 10.1021/acschembio.6b00390.

Nirschl, Hermann; Guo, Xiaoai (2018): Characterisation of structured and functionalised particles by small-angle X-ray scattering (SAXS). In *Chemical Engineering Research and Design* 136, pp. 431–446. DOI: 10.1016/j.cherd.2018.06.012.

Nissenson, Allen R.; Dylan, Michelle L.; Griffiths, Robert I.; Yu, Hsing-Ting; Dean, Bonnie B.; Danese, Mark D.; Dubois, Robert W. (2005): Clinical and economic outcomes of Staphylococcus aureus septicemia in ESRD patients receiving hemodialysis. In *American journal of kidney diseases : the official journal of the National Kidney Foundation* 46 (2), pp. 301–308. DOI: 10.1053/j.ajkd.2005.04.019.

Nwobodo, Cynthia Ebere; Nwokolo, Blessing; Iwuchukwu, Juliana Chinasa; Ohagwu, Violet Amarachukwu; Ozioko, Remigius Ikechukwu (2022): Determinants of Ruminant Farmers' Use of Sustainable Production Practices for Climate Change Adaptation and Mitigation in Enugu State, Nigeria. In *Frontiers in Veterinary Science* 9. DOI: 10.3389/fvets.2022.735139.

Okuno, Emico; Fratin, Luciano (2014): Rotations. In Emico. Okuno, Luciano. Fratin (Eds.): Biomechanics of the Human Body. New York, NY: Springer New York; Imprint; Springer (Undergraduate Lecture Notes in Physics), pp. 59–75.

Olivares, Adrian O.; Baker, Tania A.; Sauer, Robert T. (2018): Mechanical Protein Unfolding and Degradation. In *Annual review of physiology* 80, pp. 413–429. DOI: 10.1146/annurev-physiol-021317-121303.

O'Toole, G. A.; Kolter, R. (1998): Initiation of biofilm formation in Pseudomonas fluorescens WCS365 proceeds via multiple, convergent signalling pathways: a genetic analysis. In *Molecular microbiology* 28 (3), pp. 449–461. DOI: 10.1046/j.1365-2958.1998.00797.x.

Otto, Michael (2009): Staphylococcus epidermidis – the "accidental" pathogen. In *Nature reviews. Microbiology* 7 (8), pp. 555–567. DOI: 10.1038/nrmicro2182.

Pahl, Axel; Lakemeyer, Markus; Vielberg, Marie-Theres; Hackl, Mathias W.; Vomacka, Jan; Korotkov, Vadim S. et al. (2015): Reversible Inhibitors Arrest ClpP in a Defined Conformational State that Can Be Revoked by ClpX Association. In *Angewandte Chemie (International ed. in English)* 54 (52), pp. 15892–15896. DOI: 10.1002/anie.201507266.

Pamp, Sünje Johanna; Frees, Dorte; Engelmann, Susanne; Hecker, Michael; Ingmer, Hanne (2006): Spx Is a Global Effector Impacting Stress Tolerance and Biofilm

Formation in Staphylococcus aureus. In *Journal of Bacteriology* 188 (13), pp. 4861–4870. DOI: 10.1128/JB.00194-06.

Panjkovich, Alejandro; Svergun, Dmitri I. (2018): CHROMIXS: automatic and interactive analysis of chromatography-coupled small-angle X-ray scattering data. In *Bioinformatics (Oxford, England)* 34 (11), pp. 1944–1946. DOI: 10.1093/bioinformatics/btx846.

Paquete-Ferreira, João; Leisico, Francisco; Correia, Márcia A. S.; Engrola, Filipa S. S.; Santos-Silva, Teresa; Santos, Marino F. A. (2023): Using Small-angle X-ray Scattering to Characterize Biological Systems: A General Overview and Practical Tips. In *Methods in molecular biology (Clifton, N.J.)* 2652, pp. 381–403. DOI: 10.1007/978-1-0716-3147-8_22.

Parkhurst, James M.; Thorn, Andrea; Vollmar, Melanie; Winter, Graeme; Waterman, David G.; Fuentes-Montero, Luis et al. (2017): Background modelling of diffraction data in the presence of ice rings. In *IUCrJ* 4 (Pt 5), pp. 626–638. DOI: 10.1107/S2052252517010259.

Parsek, Matthew R.; Singh, Pradeep K. (2003): Bacterial biofilms: an emerging link to disease pathogenesis. In *Annual review of microbiology* 57, pp. 677–701. DOI: 10.1146/annurev.micro.57.030502.090720.

Périchon, Bruno; Courvalin, Patrice (2009): VanA-type vancomycin-resistant Staphylococcus aureus. In *Antimicrobial agents and chemotherapy* 53 (11), pp. 4580–4587. DOI: 10.1128/AAC.00346-09.

Photon Science (2024): P11 - High-throughput Macromolecular Crystallography beamline. https://photon-science.desy.de/facilities/petra_iii/beamlines/

Piiadov, Vassili; Ares de Araújo, Evandro; Oliveira Neto, Mario; Craievich, Aldo Felix; Polikarpov, Igor (2019): SAXSMoW 2.0: Online calculator of the molecular weight of proteins in dilute solution from experimental SAXS data measured on a relative scale. In *Protein science : a publication of the Protein Society* 28 (2), pp. 454–463. DOI: 10.1002/pro.3528.

Pope, Christopher G. (1997): X-Ray Diffraction and the Bragg Equation. In *J. Chem. Educ.* 74 (1), pp. 129–131.

Pouget, Jean-Paul; Levelut, Anne-Marie; Sadoc, Jean-François (2019): André Guinier: Local order in condensed matter. In *Comptes Rendus Physique* 20 (7-8), pp. 725–745. DOI: 10.1016/j.crhy.2019.03.005.

Pouladfar, G.; Jafarpour, Z.; Hosseini, S. A. M.; Janghorban, P.; Roozbeh, J. (2015): Antibiotic selective pressure and development of bacterial resistance detected in bacteriuria following kidney transplantation. In *Transplantation proceedings* 47 (4), pp. 1131–1135. DOI: 10.1016/j.transproceed.2014.11.062.

Putnam, Christopher D. (2016): Guinier peak analysis for visual and automated inspection of small-angle X-ray scattering data. In *Journal of applied crystallography* 49 (Pt 5), pp. 1412–1419. DOI: 10.1107/S1600576716010906.

Putnam, Daniel K.; Lowe, Edward W.; Meiler, Jens (2013): Reconstruction of SAXS Profiles from Protein Structures. In *Computational and structural biotechnology journal* 8, e201308006. DOI: 10.5936/csbj.201308006.

Queraltó, Camila; Álvarez, Ricardo; Ortega, Constanza; Díaz-Yáñez, Fernando; Paredes-Sabja, Daniel; Gil, Fernando (2023): Role and Regulation of Clp Proteases: A Target against Gram-Positive Bacteria. In *Bacteria* 2 (1), pp. 21–36. DOI: 10.3390/bacteria2010002.

Rahimzadeh, Maral; Sadeghizadeh, Majid; Najafi, Farhood; Arab, Seyed; Mobasheri, Hamid (2016): Impact of heat shock step on bacterial transformation efficiency. In *Molecular biology research communications* 5 (4), pp. 257–261.

Rambo, Robert P.; Tainer, John A. (2011): Characterizing flexible and intrinsically unstructured biological macromolecules by SAS using the Porod-Debye law. In *Biopolymers* 95 (8), pp. 559–571. DOI: 10.1002/bip.21638.

Rao, Nalini; Cannella, Barbara; Crossett, Lawrence S.; Yates, A. J.; McGough, Richard (2008): A Preoperative Decolonization Protocol for Staphylococcus aureus Prevents Orthopaedic Infections. In *Clinical Orthopaedics and Related Research* 466 (6), pp. 1343–1348. DOI: 10.1007/s11999-008-0225-4.

Rather, Muzamil A.; Gupta, Kuldeep; Bardhan, Pritam; Borah, Munmi; Sarkar, Anupama; Eldiehy, Khalifa S. H. et al. (2021): Microbial biofilm: A matter of grave concern for human health and food industry. In *Journal of basic microbiology* 61 (5), pp. 380–395. DOI: 10.1002/jobm.202000678.

ReAct (2024): How did we end up here? https://www.reactgroup.org/toolbox/understand/how-did-we-end-up-here/

Receveur-Brechot, Veronique; Durand, Dominique (2012): How random are intrinsically disordered proteins? A small angle scattering perspective. In *Current Protein & Peptide Science* 13 (1), pp. 55–75. DOI: 10.2174/138920312799277901.

Ripstein, Zev A.; Vahidi, Siavash; Houry, Walid A.; Rubinstein, John L.; Kay, Lewis E. (2020a): A processive rotary mechanism couples substrate unfolding and proteolysis in the ClpXP degradation machinery. In *eLife* 9. DOI: 10.7554/eLife.52158.

Ripstein, Zev A.; Vahidi, Siavash; Rubinstein, John L.; Kay, Lewis E. (2020b): A pH-Dependent Conformational Switch Controls N. meningitidis ClpP Protease Function. In *Journal of the American Chemical Society* 142 (49), pp. 20519–20523. DOI: 10.1021/jacs.0c09474.

Robert, Xavier; Gouet, Patrice (2014): Deciphering key features in protein structures with the new ENDscript server. In *Nucleic Acids Research* 42 (Web Server issue), W320-4. DOI: 10.1093/nar/gku316.

Roberts, M. C. (1996): Tetracycline resistance determinants: mechanisms of action, regulation of expression, genetic mobility, and distribution. In *FEMS microbiology reviews* 19 (1), pp. 1–24. DOI: 10.1111/j.1574-6976.1996.tb00251.x.

Sadekuzzaman, M.; Yang, S.; Mizan, M.F.R.; Ha, S. D. (2015): Current and Recent Advanced Strategies for Combating Biofilms. In *Comp Rev Food Sci Food Safe* 14 (4), pp. 491–509. DOI: 10.1111/1541-4337.12144.

Sangpuii, Lal; Dixit, Sunil Kumar; Kumawat, Manoj; Apoorva, Shekhar; Kumar, Mukesh; Kappala, Deepthi et al. (2018): Comparative roles of clpA and clpB in the survival of S. Typhimurium under stress and virulence in poultry. In *Scientific Reports* 8. DOI: 10.1038/s41598-018-22670-6.

Sauer, Robert T.; Baker, Tania A. (2011): AAA+ proteases: ATP-fueled machines of protein destruction. In *Annual review of biochemistry* 80, pp. 587–612. DOI: 10.1146/annurev-biochem-060408-172623.

Scorei, Romulus I.; Popa, Radu (2010): Boron-containing compounds as preventive and chemotherapeutic agents for cancer. In *Anti-cancer agents in medicinal chemistry* 10 (4), pp. 346–351. DOI: 10.2174/187152010791162289.

Shaw, K. J.; Rather, P. N.; Hare, R. S.; Miller, G. H. (1993): Molecular genetics of aminoglycoside resistance genes and familial relationships of the aminoglycoside-

modifying enzymes. In *Microbiological reviews* 57 (1), pp. 138–163. DOI: 10.1128/mr.57.1.138-163.1993.

Shen, Qingshan; Zhou, Wei; Hu, Liangbin; Qi, Yonghua; Ning, Hongmei; Chen, Jian; Mo, Haizhen (2017): Bactericidal activity of alpha-bromocinnamaldehyde against persisters in Escherichia coli. In *PloS one* 12 (7), e0182122. DOI: 10.1371/journal.pone.0182122.

Shi, Zhenfeng; Zhang, Jie; Tian, Lei; Xin, Liang; Liang, Chengyuan; Ren, Xiaodong; Li, Min (2023): A Comprehensive Overview of the Antibiotics Approved in the Last Two Decades: Retrospects and Prospects. In *Molecules (Basel, Switzerland)* 28 (4). DOI: 10.3390/molecules28041762.

Silbergeld, Ellen K.; Graham, Jay; Price, Lance B. (2008): Industrial food animal production, antimicrobial resistance, and human health. In *Annual review of public health* 29, pp. 151–169. DOI: 10.1146/annurev.publhealth.29.020907.090904.

Skou, Soren; Gillilan, Richard E.; Ando, Nozomi (2014): Synchrotron-based small-angle X-ray scattering of proteins in solution. In *Nature protocols* 9 (7), pp. 1727–1739. DOI: 10.1038/nprot.2014.116.

Smoum, Reem; Rubinstein, Abraham; Dembitsky, Valery M.; Srebnik, Morris (2012): Boron containing compounds as protease inhibitors. In *Chemical reviews* 112 (7), pp. 4156–4220. DOI: 10.1021/cr608202m.

Sousa Farias, S. S. de; Nemezio, M. A.; Corona, S. A. M.; Aires, C. P.; Borsatto, M. C. (2016): Effects of low-level laser therapy combined with toluidine blue on polysaccharides and biofilm of Streptococcus mutans. In *Lasers in medical science* 31 (5), pp. 1011–1016. DOI: 10.1007/s10103-016-1944-5.

Stahl, Matthias; Korotkov, Vadim S.; Balogh, Dóra; Kick, Leonhard M.; Gersch, Malte; Pahl, Axel et al. (2018): Selective Activation of Human Caseinolytic Protease P (ClpP). In *Angewandte Chemie (International ed. in English)* 57 (44), pp. 14602–14607. DOI: 10.1002/anie.201808189.

Stahl, Matthias; Sieber, Stephan A. (2017): An amino acid domino effect orchestrates ClpP's conformational states. In *Current opinion in chemical biology* 40, pp. 102–110. DOI: 10.1016/j.cbpa.2017.08.007.

Stahlhut, Steen G.; Alqarzaee, Abdulelah A.; Jensen, Camilla; Fisker, Niclas S.; Pereira, Ana R.; Pinho, Mariana G. et al. (2017): The ClpXP protease is dispensable for degradation of unfolded proteins in Staphylococcus aureus. In *Scientific Reports* 7. DOI: 10.1038/s41598-017-12122-y.

Stanley, Nicola R.; Britton, Robert A.; Grossman, Alan D.; Lazazzera, Beth A. (2003): Identification of Catabolite Repression as a Physiological Regulator of Biofilm Formation by Bacillus subtilis by Use of DNA Microarrays. In *Journal of Bacteriology* 185 (6), pp. 1951–1957. DOI: 10.1128/JB.185.6.1951-1957.2003.

Stetefeld, Jörg; McKenna, Sean A.; Patel, Trushar R. (2016): Dynamic light scattering: a practical guide and applications in biomedical sciences. In *Biophysical reviews* 8 (4), pp. 409–427. DOI: 10.1007/s12551-016-0218-6.

Stewart, Philip S.; White, Ben; Boegli, Laura; Hamerly, Timothy; Williamson, Kerry S.; Franklin, Michael J. et al. (2019): Conceptual Model of Biofilm Antibiotic Tolerance That Integrates Phenomena of Diffusion, Metabolism, Gene Expression, and Physiology. In *Journal of Bacteriology* 201 (22). DOI: 10.1128/JB.00307-19.

Storm, D. R.; Rosenthal, K. S.; Swanson, P. E. (1977): Polymyxin and related peptide antibiotics. In *Annual review of biochemistry* 46, pp. 723–763. DOI: 10.1146/annurev.bi.46.070177.003451.

Studier, F. W. (1991): Use of bacteriophage T7 lysozyme to improve an inducible T7 expression system. In *Journal of molecular biology* 219 (1), pp. 37–44. DOI: 10.1016/0022-2836(91)90855-z.

Sutherland, Mary Elizabeth (2018): Antibiotic use across the globe. In *Nature human behaviour* 2 (6), p. 373. DOI: 10.1038/s41562-018-0347-y.

Svergun, D. I.; Petoukhov, M. V.; Koch, M. H. (2001): Determination of domain structure of proteins from X-ray solution scattering. In *Biophysical journal* 80 (6), pp. 2946–2953. DOI: 10.1016/S0006-3495(01)76260-1.

Thomsen, L. E.; Olsen, J. E.; Foster, J. W.; Ingmer, H. (2002): ClpP is involved in the stress response and degradation of misfolded proteins in Salmonella enterica serovar Typhimurium. In *Microbiology (Reading, England)* 148 (Pt 9), pp. 2727–2733. DOI: 10.1099/00221287-148-9-2727.

Veerachamy, Suganthan; Yarlagadda, Tejasri; Manivasagam, Geetha; Yarlagadda, Prasad Kdv (2014): Bacterial adherence and biofilm formation on medical implants: a review. In *Proceedings of the Institution of Mechanical Engineers. Part H, Journal of engineering in medicine* 228 (10), pp. 1083–1099. DOI: 10.1177/0954411914556137.

Vera, Laura; Stura, Enrico A. (2014): Strategies for Protein Cryocrystallography. In *Crystal Growth & Design* 14 (2), pp. 427–435. DOI: 10.1021/cg301531f.

Vivas, Roberto; Barbosa, Ana Andréa Teixeira; Dolabela, Silvio Santana; Jain, Sona (2019): Multidrug-Resistant Bacteria and Alternative Methods to Control Them: An Overview. In *Microbial drug resistance (Larchmont, N.Y.)* 25 (6), pp. 890–908. DOI: 10.1089/mdr.2018.0319.

Walsh, Timothy R.; Gales, Ana C.; Laxminarayan, Ramanan; Dodd, Philippa C. (2023): Antimicrobial Resistance: Addressing a Global Threat to Humanity. In *PLoS medicine* 20 (7), e1004264. DOI: 10.1371/journal.pmed.1004264.

Wang, Chongzhen; Li, Min; Dong, Dandan; Wang, Jianping; Ren, Jun; Otto, Michael; Gao, Qian (2007): Role of ClpP in biofilm formation and virulence of Staphylococcus epidermidis. In *Microbes and infection* 9 (11), pp. 1376–1383. DOI: 10.1016/j.micinf.2007.06.012.

Wang, Mengjie; Shen, Jin; Thomas, John C.; Mu, Tongtong; Liu, Wei; Wang, Yajing et al. (2021): Particle Size Measurement Using Dynamic Light Scattering at Ultra-Low Concentration Accounting for Particle Number Fluctuations. In *Materials (Basel, Switzerland)* 14 (19). DOI: 10.3390/ma14195683.

Wei, Bingyan; Zhang, Tao; Wang, Pengyu; Pan, Yihui; Li, Jiahui; Chen, Weizhong et al. (2022): Anti-infective therapy using species-specific activators of Staphylococcus aureus ClpP. In *Nature communications* 13 (1), p. 6909. DOI: 10.1038/s41467-022-34753-0.

Welch, William J.; Brown, C. Randell (1996): Influence of molecular and chemical chaperones on protein folding. In *Cell Stress & Chaperones* 1 (2), pp. 109–115.

Wilson, Daniel N. (2014): Ribosome-targeting antibiotics and mechanisms of bacterial resistance. In *Nature reviews. Microbiology* 12 (1), pp. 35–48. DOI: 10.1038/nrmicro3155.

Witte, W. (2000): Selective pressure by antibiotic use in livestock. In *International Journal of Antimicrobial Agents* 16 Suppl 1, S19-24. DOI: 10.1016/S0924-8579(00)00301-0.

Witte, W. (2004): Glycopeptide resistant Staphylococcus. In *Journal of veterinary medicine. B, Infectious diseases and veterinary public health* 51 (8-9), pp. 370–373. DOI: 10.1111/j.1439-0450.2004.00774.x.

Wittig, Ilka; Braun, Hans-Peter; Schägger, Hermann (2006): Blue native PAGE. In *Nature protocols* 1 (1), pp. 418–428. DOI: 10.1038/nprot.2006.62.

Wittig, Ilka; Schägger, Hermann (2008): Features and applications of blue-native and clear-native electrophoresis. In *Proteomics* 8 (19), pp. 3974–3990. DOI: 10.1002/pmic.200800017.

Wlodawer, Alexander; Dauter, Zbigniew; Jaskolski, Mariusz (Eds.) (2017): Protein crystallography. Methods and protocols. New York NY: Humana Press (Springer protocols, 1607).

Wu-Wu, Jannette Wen Fang; Guadamuz-Mayorga, Carolina; Oviedo-Cerdas, Douglas; Zamora, William J. (2023): Antibiotic Resistance and Food Safety: Perspectives on New Technologies and Molecules for Microbial Control in the Food Industry. In *Antibiotics (Basel, Switzerland)* 12 (3). DOI: 10.3390/antibiotics12030550.

Wyatt (2024): Dynamic Light Scettering Instruments. https://www.wyatt.com/products/

Xie, Fang; Zhang, Yanhe; Li, Gang; Zhou, Long; Liu, Siguo; Wang, Chunlai (2013): The ClpP Protease Is Required for the Stress Tolerance and Biofilm Formation in Actinobacillus pleuropneumoniae. In *PloS one* 8 (1). DOI: 10.1371/journal.pone.0053600.

Xu, Qifang; Dunbrack, Roland L. (2019): Principles and characteristics of biological assemblies in experimentally determined protein structures. In *Current opinion in structural biology* 55, pp. 34–49. DOI: 10.1016/j.sbi.2019.03.006.

Xu, Xiaolong; Wang, Yanhui; Huang, Wei; Li, Danyang; Deng, Zixin; Long, Feng (2024): Structural insights into the Clp protein degradation machinery. In *mBio* 15 (4). DOI: 10.1128/mbio.00031-24.

Ye, Fei; Zhang, Jie; Liu, Hongchuan; Hilgenfeld, Rolf; Zhang, Ruihan; Kong, Xiangqian et al. (2013): Helix unfolding/refolding characterizes the functional dynamics of Staphylococcus aureus Clp protease. In *The Journal of biological chemistry* 288 (24), pp. 17643–17653. DOI: 10.1074/jbc.M113.452714.

Yin, Wen; Wang, Yiting; Liu, Lu; He, Jin (2019): Biofilms: The Microbial "Protective Clothing" in Extreme Environments. In *International journal of molecular sciences* 20 (14). DOI: 10.3390/ijms20143423.

Yin, Wen; Xu, Siyang; Wang, Yiting; Zhang, Yuling; Chou, Shan-Ho; Galperin, Michael Y.; He, Jin (2021): Ways to control harmful biofilms: prevention, inhibition, and eradication. In *Critical reviews in microbiology* 47 (1), pp. 57–78. DOI: 10.1080/1040841X.2020.1842325.

Young, Jasmine Y.; Westbrook, John D.; Feng, Zukang; Sala, Raul; Peisach, Ezra; Oldfield, Thomas J. et al. (2017): OneDep: Unified wwPDB System for Deposition, Biocuration, and Validation of Macromolecular Structures in the PDB Archive. In *Structure (London, England : 1993)* 25 (3), pp. 536–545. DOI: 10.1016/j.str.2017.01.004.

Yu, Angela Yeou Hsiung; Houry, Walid A. (2007): ClpP: a distinctive family of cylindrical energy-dependent serine proteases. In *FEBS letters* 581 (19), pp. 3749–3757. DOI: 10.1016/j.febslet.2007.04.076.

Zanwar, Saurabh; Abeykoon, Jithma Prasad; Kapoor, Prashant (2018): Ixazomib: a novel drug for multiple myeloma. In *Expert review of hematology* 11 (10), pp. 761–771. DOI: 10.1080/17474086.2018.1518129.

Zeth, Kornelius; Ravelli, Raimond B.; Paal, Klaus; Cusack, Stephen; Bukau, Bernd; Dougan, David A. (2002): Structural analysis of the adaptor protein ClpS in complex with the N-terminal domain of ClpA. In *Nature structural biology* 9 (12), pp. 906–911. DOI: 10.1038/nsb869.

Zhang, Jie; Ye, Fei; Lan, Lefu; Jiang, Hualiang; Luo, Cheng; Yang, Cai-Guang (2011): Structural switching of Staphylococcus aureus Clp protease: a key to understanding protease dynamics. In *The Journal of biological chemistry* 286 (43), pp. 37590–37601. DOI: 10.1074/jbc.M111.277848.

Zhang, Xiaozhou; Adwal, Alaknanda; Turner, Andrew G.; Callen, David F.; Abell, Andrew D. (2016): New Peptidomimetic Boronates for Selective Inhibition of the Chymotrypsin-like Activity of the 26S Proteasome. In *ACS Medicinal Chemistry Letters* 7 (12), pp. 1039–1043. DOI: 10.1021/acsmedchemlett.6b00217.

Zheng, Jinxin; Wu, Yang; Lin, Zhiwei; Wang, Guangfu; Jiang, Sibo; Sun, Xiang et al. (2020): ClpP participates in stress tolerance, biofilm formation, antimicrobial tolerance, and virulence of Enterococcus faecalis. In *BMC microbiology* 20 (1), p. 30. DOI: 10.1186/s12866-020-1719-9.

Appendix

A1. Chemicals and Hazards
The symbol of each GHS code is shown in A3.

Table A1 - Chemicals with their respective HP-statements

Chemical	GHS code	H-statements	P-statements
Acetic acid glacial	GHS02, GHS05	H226 - H314	P210
Acrylamide	GHS08, GHS06	H301 - H312 + H332 - H315 -H317 - H319 -H340 - H350 - H361f - H372	P201 - P280-P302 + P352 - P304 +P340 - P305 + P351 + P338 - P308 + P313
Ammonium persulfate	GHS02, GHS07, GHS08	H272 - H302 + H312 - H315 -H317 - H319 - H334 - H335 - H412	P210 - P220 - P221 - P261 - P264 - P270 - P271 - P272 - P27 3- P280 - P285 -P301 + P312 - P302 + P352 - P304 + P340 -P305 + P351 + P338 - P332 - P330 - P333 + P313 - P337 + P313 -P342 + P311 - P362 -P370 + P378 - P403 + P233 - P405 - P501
ONC212	GHS07, GHS08	H302 – H315 – H319 – H335 – H351 – H361 – H373	P201 – P202 – P261 – P264 – P270 – P280 – P301 + P312- P302 + P352 – P304 + P340– P305 + P351 + P338– P308 + P313– P337 + P313 – P362 – P403 + P233 – P405 –P501

Chemical	GHS code	H-statements	P-statements
Ammonium sulfate	GHS06, GHS08, GHS09	H300 - H315- H319 - H361 - H372 - H411	P260 - P273 - P280
Bortezomib	GHS07	H227	P210 - P280 -P370 + P378 - P403 + P235 - P501
Coomassie brilliant blue R 250	GHS07	H227 - H315 - H319	P210 - P264 - P280 - P302 + P352 -P305 + P351 + P338 - P321 - P337 + P313 - P362 - P403 + P235 - P501
Dimethyl sulfoxide	GHS07	H302 - H315 - H319	P301 + P312 + P330 - P305 + P351 + P338
Dithiothreitol	GHS07	H319	P280 -P305 + P351 + P338 - P337 + P313
Calcium chloride	GHS02, GHS07	H225 - H319	P210 - P233 -P337 + P313 - P370 + P378 - P403 + P235 - P501
Glycerol	GHS05, GHS07	H290	P234-P390
Hydrochloric acid	GHS05, GHS07	H290 - H314 - H335	P280 - P303 + P361 + P353 - P304 + P340 -P305 + P353 + P338 - P310
Acrylamide	GHS06, GHS07, GHS08	H301 – H311 – H331 – H315 – H319 – H340 – H350 – H372	P201 – P202 – P261 – P264 – P270 – P271 – P272 – P273 – P280 – P301 + P310 – P302 + P352 – P304 + P340– P305 + P351 + P338 – P308 + P313– P310 – P333 + P313 – P362 + P364– P403 + P233– P405 – P501

Chemical	GHS code	H-statements	P-statements
4-(2-hydroxyethyl)piperazin-1-ylethanesulphonic acid	GHS02, GHS07	H225-H319-H336	P210-P305+P351+P338 - P312-P370+P378 - P403+P233 - P403+P235-P501
Isopropyl-β-D-thiogalacto-pyranoside	GHS07	H315 – H319 – H335	P261 – P264 – P270 – P280 – P305 + P351 + P338 – P302 + P352 – P332 + P313
Ixazomib	GHS07	H302-H315-H319-H335	P261-P305+P351+P338
2-Methyl-2,4-pentanediol	GHS07, GHS08	H315-H319-H361d	P280-P305+P351+P338 - P308+P313
N-(3-carboxyl-1-oxopropyl)-L-leucyl-N-(4-methyl-2-oxo-2H-1-benzopyran-7-yl)-L-tyrosamide	GHS07	H302 – H315 – H319 – H335 – H341 - H351	P201 – P202 – P261 – P264 – P270 – P271 – P280 – P301 + P312 – P302 + P352 – P305 + P351 + P338– P308 + P313– P405 – P501
Nitrogen	GHS04	H280	P403
ONC206	GHS07, GHS08	H302 – H315 – H319 – H335 – H341 - H351	P201 – P202 – P261 – P264 – P270 – P271 – P280 – P301 + P312 – P302 + P352 – P305 + P351 + P338– P308 + P313– P405 – P501
Tavaborole	GHS07	H302-H315-H319-H335	P261 - P264 - P270 - P271 - P280 - P302 + P352 -P304 + P340 -P305 + P351 + P338 -P321 - P330 - P337 - P362 + P364 -P403 + P233 - P405 - P501-

136

Chemical	GHS code	H-statements	P-statements
Tris(hydroxymethyl) aminomethane	GHS07	H315 – H319 – H335	
Sodium acetate	GHS07	H319	P264 – P280 – P305 + P351 + P338– P337 + P313
Sodium dodecyl sulfate	GHS05, GHS07	H302-H315-H318	P270-P280-P302+P352-P305+P351+P338-P321-P330-P501
Sodium chloride			P264 – P270
Sodium hydroxide	GHS05	H290-H314	P233-P280-P303+P361+P353-P305+P351+P338-P310
Kanamycin	GHS07, GHS08	H302 – H319 – H334 – H335 – H373	P261 – P264 – P270 – P271 – P272 – P280 – P301 + P312 – P304 + P340– P305 + P351 + P338 – P314 – P501
Ethanol	GHS02, GHS07	H225, H319, H336	P210 – P233 – P240 – P241 – P242 – P243 – P261 – P264 – P271 – P280 – P303 + P361 + P353 – P304 + P340– P305 + P351 + P338 – P337 + P313– P370 + P378– P405 – P501 – P403 + P233
Nickel(II) sulphate	GHS05, GHS07, GHS08, GHS09	H302 – H315 – H317 – H319 – H334 – H341 – H350 – H360 – H372 – H400 – H410	P201 – P202 – P261 – P264 – P270 – P272 – P273 – P280 – P301 + P312– P302 + P352– P304 + P340 – P305 + P351 + P338– P308 + P313 – P314 – P333 + P313– P391 – P403 + P233– P405 – P501 -

A2. Crystallization screens

Table A2 - Crystallization screens used for crystallization and co-crystallization trials.

Screen	GHS code	H-statements	P-statements
AmSO4-suite (Quiagen)	GHS02, GHS06, GHS08, GHS09	H225 - H301 -H330 - H350 - H340 - H360fd - H372 - H411	P101 - P201 – P273 - P280 -P309 + P311
ComPAS-suite (Quiagen)	GHS02, GHS06, GHS07, GHS08, GHS09	H225 - H301 - H302 - H315 -H319 - H331 - H332 - H335 - H340 -H350 - H360fd - H373 - H411	P101 - P201 - P270 - P273 - P280 - P305 + P351 + P338 - P309 + P311 - P313
JCSG-plus (Molecular Dimensions)	GHS02, GHS05, GHS06, GHS07, GHS09	H225 - H301 -H312 - H315 - H31 8- H331 - H335 -H350 - H411	P101 - P201 - P270 - P280 -P305 + P51+ P338 -P309 + P311 - P313
Morpheus (Molecular Dimensions)	GHS02, GHS06, GHS07, GHS08, GHS09	H225 - H301 -H302 - H315 - H319 - H331 - H332 -H335 - H340 - H350 - H360fd - H373 - H411	P101 - P201 - P270 - P273 - P280 - P305 + P351 + P338 - P309 + P311 - P313
PACT premier (Molecular Dimensions)	GHS06	H301 - H331 - H412	P101 - P270 - P273 - P280 - P309 + P311
Structure (Molecular Dimensions)	GHS02, GHS06, GHS07, GHS08, GHS09	H225 - H301 -H302 - H315 - H319 - H331 - H332 -H335 - H340 - H350 - H360fd - H373 - H411	P101 - P201 - P270 - P273 - P280 - P305 + P351 + P338 - P309 + P311 - P313
SturaFootprint&Macrosol (Molecular Dimensions)	GHS02, GHS06, GHS07, GHS08, GHS09	H225 - H301 -H302 - H315 - H319 - H331 - H332 - H335 - H340 -H350 - H360fd - H373 - H411	P101 - P201 - P270 - P273 - P280 - P305 + P351 + P338 - P309 + P311 - P313

A3. GHS and risk symbols

Figure A1. Identification of each GHS pictogram related to chemicals used in the present work.

A4. Hazard statements

H225	Highly flammable liquid and vapor.
H227	Combustible liquid.
H272	May intensify fire; oxidizer.
H290	May be corrosive to metals.
H280	Contains gas under pressure; may explode if heated.
H300	Fatal if swallowed.
H301	Toxic if swallowed.
H302	Acute toxicity, oral.
H302 + H312	Harmful if swallowed or in contact with skin.
H312+H332	Harmful in contact with skin or if inhaled.
H312	Harmful in contact with skin.
H314	Causes severe skin burns and eye damage.
H315	Causes skin irritation.
H317	May cause an allergic skin reaction.
H318	Causes serious eye damage.
H319	Causes serious eye irritation.
H330	Fatal if inhaled.
H331	Toxic if inhaled.
H332	Harmful if inhaled.
H334	May cause allergy or asthma symptoms or breathing difficulties if inhaled.
H335	May cause respiratory irritation.
H336	May cause drowsiness or dizziness.
H340	May cause genetic defects.
H350	May cause cancer.
H360fd	May damage fertility or the unborn child.
H361	Suspected of damaging fertility or the unborn child.
H361d	Suspected of damaging the unborn child.
H361f	Suspected of damaging fertility.
H372	Causes damage to organs through prolonged or repeated exposure.
H373	May cause damage to organs through prolonged or repeated exposure.
H411	Toxic to aquatic life with long lasting effects.
H412	Harmful to aquatic life with long lasting effects.

A5. Precautionary statements

P101	If medical advice is needed, have product container or label at hand.
P201	Obtain special instructions before use.
P210	Keep away from heat.
P220	Keep/store away from clothing/combustible materials.
P221	Take any precaution to avoid mixing with combustibles.
P233	Keep container tightly closed.
P260	Do not breathe dust/fume/gas/mist/vapors/spray.
P261	Avoid breathing dust/fume/gas/mist/vapors/spray.
P264	Wash skin thoroughly after handling.
P270	Do not eat, drink or smoke when using this product.
P271	Use only outdoors or in a well-ventilated area.
P272	Contaminated work clothing should not be allowed out of the workplace.
P273	Avoid release to the environment.
P280	Wear protective gloves/protective clothing/eye protection/face protection.
P285	In case of inadequate ventilation wear respiratory protection.
P301 + P312 + P330	IF SWALLOWED: Call a POISON CENTER or doctor/physician if you feel unwell.
P302 + P352	IF ON SKIN: Wash with plenty of soap and water.
P303+P361+P353	IF ON SKIN (or hair): take off immediately all contaminated clothing. Rinse skin with water [or shower].
P304 + P340	IF INHALED: remove victim to fresh air and keep at rest in a position comfortable for breathing.
P305 + P351 + P338	IF IN EYES: rinse cautiously with water for several minutes. Remove contact lenses, if present and easy to do. Continue rinsing.
P308+P313	IF exposed or concerned: get medical advice/attention.
P309+P311	IF exposed or you feel unwell: call a POISON CENTER or doctor.
P310	Immediately call a POISON CENTER/doctor.
P313	Get medical advice/attention.
P321	specific measures
P322	specific measures
P330	Rinse mouth.
P333 + P313	If skin irritation or rash occurs: get medical advice/attention.
P337	If eye irritation persists: get medical advice/attention.
P337 + P313	If eye irritation persists: get medical advice/attention.
P341 + P311	If experiencing respiratory symptoms: call a POISON CENTER or doctor/physician.
P362	Take off contaminated clothing and wash before reuse.

P362+P364	Take off contaminated clothing and wash it before reuse.
P370 + P378	In case of fire: use dry sand, dry chemical or alcohol-resistant foam for extinction.
P390	Absorb spillage to prevent material damage.
P403+P233	Store in a well-ventilated place. Keep container tightly closed.
P403 + P233 + P235	Store in a well-ventilated place. Keep container tightly closed.
P405	Store locked up.
P501	Dispose of contents/container to an approved waste disposal plant.

A6. Statistics of DAMMIN reconstitutions – native *Se*ClpP
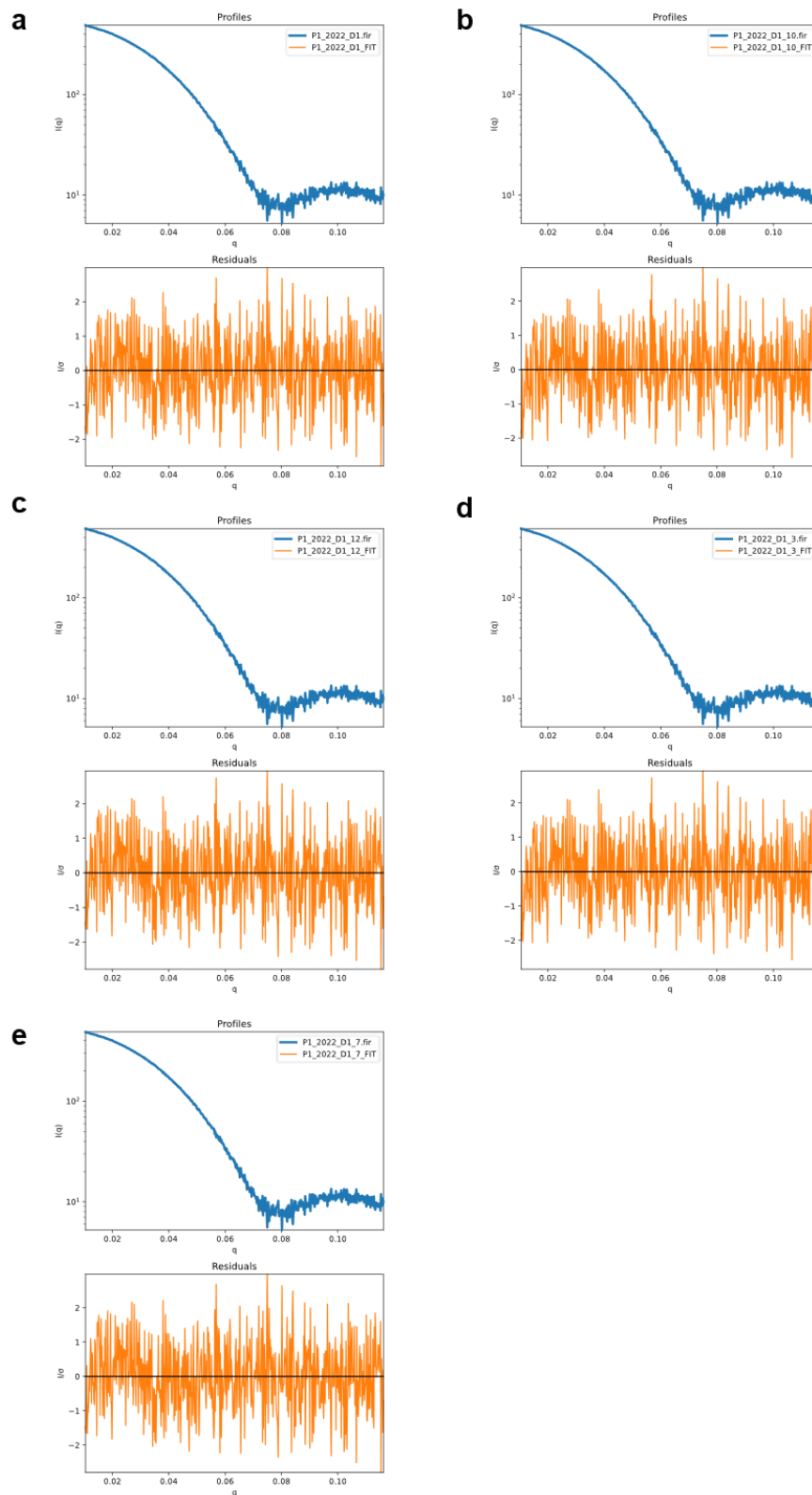
Figure A6.1 – Curve fitting and residual plot for 5 DAMMIN reconstitutions of *Se*ClpP-P1.
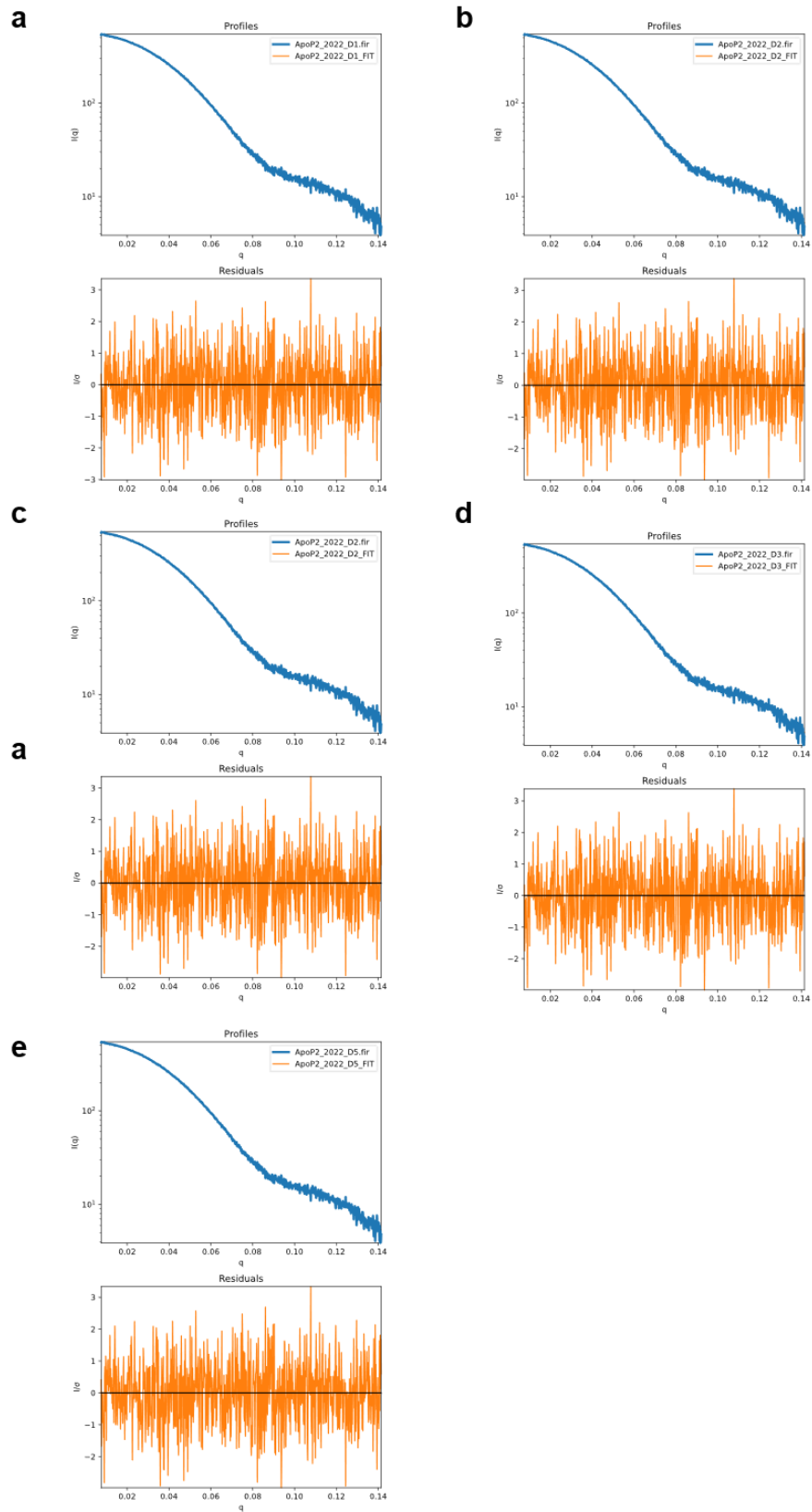
Figure A6.2 - Curve fitting and residual plot for 5 DAMMIN reconstitutions of *Se*ClpP-P2.

Tables A6.1 (a – e) – Statistical validation of the 5 DAMMIN reconstitutions for *Se*ClpP – P1.

a

Reconstruction 1 (P1_2022_D1)	
χ^2 value	0.95
CorMap P-value	0.46
Anderson-Darling's P-value	0.98

b

Reconstruction 2 (P1_2022_D1_10)	
χ^2 value	0.95
CorMap P-value	0.46
Anderson-Darling's P-value	0.97

c

Reconstruction 3 (P1_2022_D1_12)	
χ^2 value	0.96
CorMap P-value	0.07
Anderson-Darling's P-value	0.98

d

Reconstruction 4 (P1_2022_D1_3)	
χ^2 value	0.949
CorMap P-value	0.46
Anderson-Darling's P-value	0.98

e

Reconstruction 5 (P1_2022_D1_7)	
χ^2 value	0.96
CorMap P-value	0.26
Anderson-Darling's P-value	0.96

Tables 6.2 (a – e) – Statistical validation of the 5 DAMMIN reconstitutions for *Se*ClpP – P2.

a

Reconstruction 1 (ApoP2_2022_D1)	
χ^2 value	1.00
CorMap P-value	0.79
Anderson-Darling's P-value	0.87

b

Reconstruction 2 (ApoP2_2022_D2)	
χ^2 value	1.00
CorMap P-value	0.54
Anderson-Darling's P-value	0.89

c

Reconstruction 3 (Apo2_2022_D3)	
χ^2 value	1.00
CorMap P-value	0.79
Anderson-Darling's P-value	0.88

d

Reconstruction 4 (ApoP2_2022_D4)	
χ^2 value	1.00
CorMap P-value	0.79
Anderson-Darling's P-value	0.86

e

Reconstruction 5 (ApoP2_2022_D5)	
χ^2 value	1.00
CorMap P-value	0.54
Anderson-Darling's P-value	0.85

A7. Ixazomib bound to the 14 *Se*ClpP's catalytic sites
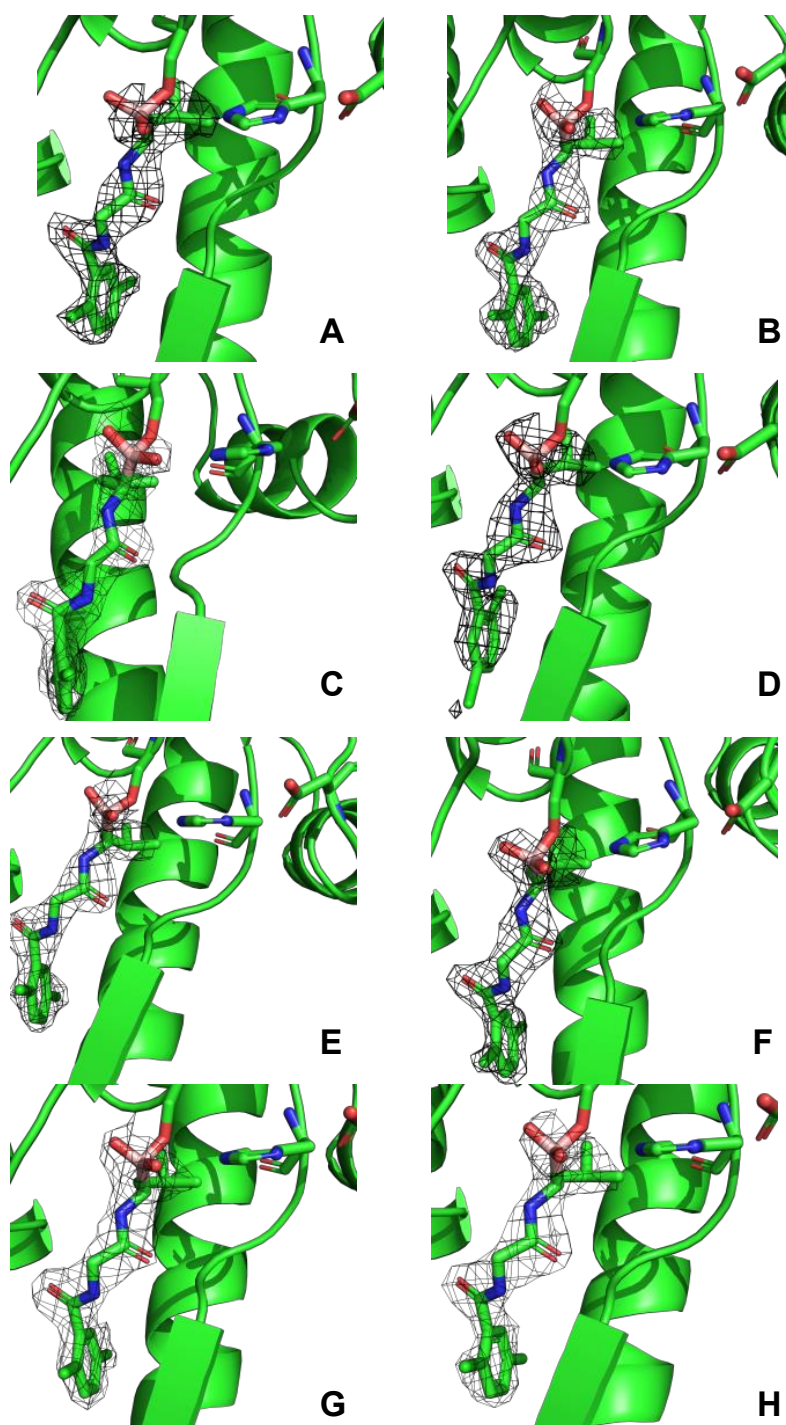
Figure A7.1 - Catalytic sites of all 14 *Se*ClpP monomers in complex with ixazomib. The ligand molecule is shown with the corresponding 2Fo-Fc electron density at 1.5σ. The refined ligand occupancy varies from 0.80 to 1.0 (Chains A to H).
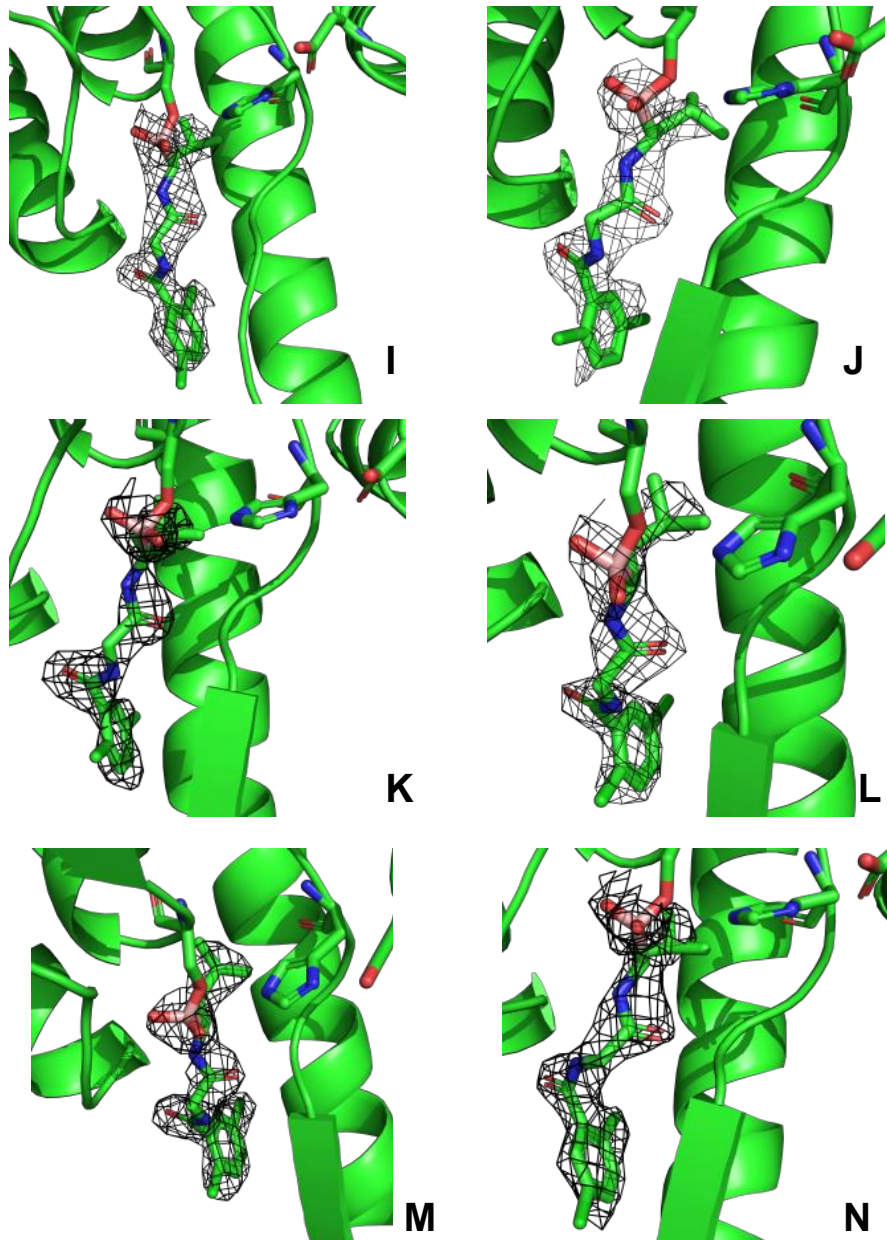
Figure A7.2 - Catalytic sites of all 14 *Se*ClpP monomers in complex with ixazomib. The ligand molecule is shown with the corresponding 2Fo-Fc electron density at 1.5σ. The refined ligand occupancy varies from 0.80 to 1.0 (Chains I to N).

Acknowledgments

List of Figures

Figure 13 – P11 beamline and the sample robot for data collection with single crystals (MX crystallography). Picture obtained from Photon Science, 2024.

Figure 14 – (**a**) Encoding gene sequence of ClpP from *S. epidermidis* (*Se*ClpP) found on UniProt database (UniProtKB: A0A0N1MQL5). (**b**) Gene of *Se*ClpP after codon optimization for heterologous expression in *E. coli* (altered codons are in bold). (**c**) The illustration of the vector pET28a(+) and the region where the gene copy was inserted is zoomed in. The removed portion of the plasmid between the restriction sites for NcoI and XhoI is displayed. The insert (brown color), the *clpP* gene, is also shown after the assembly.

Figure 15 – Depiction of (**a**) IMAC with Ni-NTA matrix and (**b**) SEC as a polishing step.

Figure 16 - General illustration of main elements in DLS measurements.

Figure 17 – P12 beamline (EMBL/PETRA III) in Hamburg, Germany. Illustration of SEC-SAXS and Batch-SAXS setups. Regardless of the method of choice, the sample is conducted to a capillary where the incident X-ray beam is scattered. The recorded one-dimensional scattering profile is then used for the low-resolution structural analysis and the *ab initio* modeling of native protein and protein-ligand complexes in solution.

Figure 18 – Illustration of the Bragg's law. Extracted from Britannica, 2024.

Figure 19 – The phase diagram and its main zones (Wlodawer et al. 2017).

Figure 20 – Expression and purification of *Se*ClpP. (**a**) 15% SDS-PAGE after expression tests with three *E. coli* expression systems: BL21(DE3), BL21 Rosetta, and BL21 Star. Note that the control sample, the one without IPTG, is marked with an asterisk. Control was removed after 4h to prove there was no band in the control lanes at around 25 kDa, the region where ClpP is expected to be seen. (**b**) SEC chromatogram after the last purification step of *Se*ClpP with the preparative column HiLoad 26/600 Superdex 200 pg. The presence of two main peaks, P1 and P2, is observed at this stage. (**c**) 15% SDS-PAGE with fractions from P1 and P2. (**d**) Native-PAGE after pooling the fractions from P1 and P2.

Figure 21 – Main graphs obtained from SAXS measurements with native *Se*ClpP. (**a**) SEC chromatogram confirms the presence of two main species: P1 and P2. (**b**) X-ray scattering intensities were measured from P1 (dark blue curve) and P2 (light blue curve) samples. Moreover, (**c**) and (**d**) represent Guinier fits, the calculation of R_G, and the fidelity values within the validity range $0 < sR_G < 1.3$. (**e**) P(r) functions of P1 (purple curve) and P2 (blue curve). (**f**) Kratky plot for P1 and P2 demonstrates the complete folding of both species. **s** in 1/nm.

Figure 22 – *ab initio* representations of native SeClpP. The models confirm the oligomeric state of the protein samples P1 and P2: tetradecamer and heptamer, respectively. (**a**) DAM of the 14-mer structure and (**b**) DAM of the 7-mer structure. Both were constructed by DAMMIN/ATSAS suite with a collection of densely packed beads within a search volume. (**c**) Model of the 14-mer and (**d**) 7-mer structures obtained by GASBOR/ATSAS suite. This program uses the concept of dummy residues corresponding to amino acids in the protein chain.

Figure 23 – Quality assessment of how well the theoretical curve (light blue) calculated from GASBOR models fits the experimental data (dark blue). (**a**) Scattering intensity in logarithmic scale ($\log_{10}I$) *vs.* the scattering magnitude (**s** as 1/nm), and (**b**) normalized residual plot for P1 sample. Likewise, for P2 sample, (**c**) the graph scattering intensity in logarithmic scale *vs.* the scattering magnitude (**s** as 1/nm) and the (**d**) normalized residual plot. In (**c**) and (**d**), the electron density is well distributed along $\Delta I/\sigma$ within ±3, not informing systematic errors or model inadequacies. $\Delta I/\sigma$ is dimensionless.

Figure 24 – Steps prior to X-ray diffraction: (**a**) Radius distribution and (**b**) radius plots to evaluate the sample monodispersity. (**c**) Needle-like crystals in a droplet inside a Linbro-like plate (vapor diffusion, hanging-drop technique) and (**d**) Single native *Se*ClpP crystals prior to X-ray diffraction at different angles.

Figure 25 – Overview of the crystal structure of native *Se*ClpP – P1 (14-mer). (**a**) Front view of the barrel-like structure. (**b**) Another illustration where 14 molecules of MPD, the precipitating agent, are found in each of the protein's catalytic sites. (**c**) Two-color scheme of the stacked heptameric rings forming the tetradecamer. An internal view of a heptamer with 7 MPD molecules and a subunit in yellow.

Figure 26 – One axial pore, two representations. (**a**) Given the flexibility of the loops that constitute the ClpP's gating mechanism, they could not be wholly resolved by using X-ray diffraction data. Then, the pore looks larger than it really is. Nevertheless, in (**b**), a low-resolution *ab initio* model, even without a view at an atomic level, demonstrates the actual dimension of the same region. The diameter, in both cases, is represented by approximate values defined with PyMOL.

Figure 27 – General view of a *Se*ClpP subunit with its main constituent parts: partial N-terminal loop (gating mechanism), head domain, E-helix region (connection between the opposing rings), catalytic site with a MPD molecule, and C-terminal portion. Zoomed-in depiction of the catalytic site with the Ser98-His123-Asp142 triad: the alignment of those residues with the formation of hydrogen bonds (black dashed lines) makes the protein active for hydrolysis.

Figure 28 – Lipophilicity profile of the contact region between two vicinal subunits. (**a**) An example of a "hydrophobic pocket" is delimited by a black dashed rectangle. (**b**) In one *Se*ClpP subunit, the contact zone responsible for forming the allosteric site is shown inside a red dashed rectangle. According to the scale, blue areas are more hydrophilic, and brownish portions are more hydrophobic.

Figure 29 – Overall lipophilic profile of *Se*ClpP. As seen in (**a**), the external area of the head domain of each monomer is predominantly hydrophilic. At the same time, in (**b**), the allosteric sites (red dashed circles) and the portion surrounding the axial pore are more lipophilic, unveiling that hydrophobic interactions constitute the controlling mechanism of the pore geometry. (**c**) Hydrophilic zone of interactions between gly-rich regions protruding from monomers in opposing rings, and (**d**) catalytic cavity with a hydrophobicity around 0.70, according to the GeoMine server (Diedrich et al. 2024).

Figure 30 – Detailed depiction of the connection between two monomers from opposing subunits. E-helices are in red, and sticks represent the amino acid residues in the gly-rich regions. The hydrogen bonds, as yellow dashed lines, have lengths of approx. 2.8 – 3.0 Å and form an ordered secondary structure of antiparallel beta-sheets that support stability to a functional ClpP.

Figure 31 – Peptidolytic assays with the fluorogenic substrate Suc-LY-AMC, the inactive mutant *Se*ClpP S98A (red curve), and wild-type *Se*ClpP (black curve).

Figure 32 – Effect of DMSO on melting temperature (T_M) obtained from nanoDSF measurements.

Figure 33 – Dimensionless plots built from scattering intensities measured with samples containing apo *Se*ClpP free from DMSO (dark green curve) and apo *Se*ClpP supplemented with 1% v/v DMSO (light green curve).

Figure 34 – Ixazomib molecule with its elemental parts.

Figure 35 – Bortezomib with its elemental parts.

Figure 36 – (**a**) Chromatogram after SEC during SAXS measurements. The red graph represents the sample composed of native *Se*ClpP in P1 and P2 states. After incubation with ixazomib (1:50 protein-to-ligand ratio), the black graph shows the presence of tetradecamers only. (**b**) Intensity scattering profiles of Native P1, native P2, and *Se*ClpP-ixazomib complex. **s**, the scattering vector, as 1/nm.

Figure 37 – Guinier plots of (**a**) native P1 and (**b**) *Se*ClpP-ixazomib complex.

Figure 38 – Dimensionless plots with curves related to (**a**) apo protein with 1% v/v DMSO (purple color) and (**b**) *Se*ClpP-ixazomib complex (green color).

Figure 39 – Dimensionless Kratky plot showing that the second peak of the *Se*ClpP-ixazomib complex (black graph) is slightly shifted to the right.

Figure 40 – (**a**) R_h variation calculated for the sample with native P2 before (black bar) and after incubation with the ligand (gray bar). (**b**) R_h variation calculated for the sample with native P1 before (black bar) and after incubation with the ligand (gray bar). t-test shows that the changes in both cases were significant: (**a**) p = 0.0363 ($p < 0.05$) and (**b**) p = 0.0004 ($p < 0.05$).

Figure 41 – First derivative peaks obtained from nanoDSF measurements. At low protein-to-ligand ratios, there are two peaks for two different states. At higher ixazomib concentrations, one predominant peak is observed at high T_M values.

Figure 42 – Crystal structure of *Se*ClpP-ixazomib complex and a ligand molecule bound to one of the ClpP's catalytic sites.

Figure 43 – (**a**) Fluorescence assays with different *Se*ClpP concentrations. (**b**) Linear fitting with the initial velocity (V_0) for each one of the *Se*ClpP concentrations in (**a**). FI means fluorescence intensity.

Figure 44 – Determination of optima pH and temperature values for assays with *Se*ClpP. FI is fluorescence intensity.

Figure 45 – (**a**) Degradation of Suc-LY-AMC in the presence of different ixazomib concentrations. Lower protein-to-ligand ratios result in the enhancement of peptidolysis up to 1:3. In sequence, as more ligand is added, only inhibition is observed. This dual modulation is justified by (**b**) ITC measurements: when the drug starts populating the protein, a cooperative effect happens with heat release.

At this stage, the peptidolytic activity increases until a second process of heat release is noted, and then the inhibitory effect becomes predominant.

Figure 46 – Interaction between ixazomib and *Se*ClpP: While the boronic acid moiety is covalently bound to Ser98, the peptidomimetic portion forms hydrogen bonds with important amino acid residues in the vicinity of the catalytic triad, making the entire protein structure more stable and optimizing its function. Ixazomib is shown with the 2Fo-Fc electron density at 1.5σ.

Figure 47 – 15% SDS-PAGE after reactions with β-casein monitored for a period of 60 minutes. (**a**) ixazomib and *Se*ClpP concentrations: 200µM and 10µM, respectively; (**b**) ixazomib and *Se*ClpP concentrations: 500µM and 10µM, respectively; (**c**) Comparative experiment with ixazomib (1mM) and ONC206 (10µM), where it is noticeable that the MWs of product fragments vary, in accordance with the ligand used. A possible explanation for this difference is that ixazomib occupies the catalytic sites, affecting the processive degradation of the substrate. ONC206 only binds to the allosteric regions. Degradation products of low molecular weight can be clearly seen in (**b**) and (**c**). *t= 0 min corresponds to the time point with no incubation, but until the complete denaturation of the protein prior to the SDS-PAGE, b-casein degradation happened in the quick reaction with ONC206.

Figure 48 – (**a**) *Se*ClpP-ixazomib complex, (**b**) *Sa*ClpPY63A mutant, and (**c**) native *Se*ClpP. In (**a**) and (**b**), the Asn42 residue is in "down" position, indicating that the structure is active for proteolysis and open for the access of globular proteins, and explaining the observations in Figure 47. Conversely, the "up" Asn42 in apo *Se*ClpP reflects the closed nature of (**c**).

Figure 49 – MSA with assigned secondary structures of *Se*ClpP and its homologs: *Sa*ClpP (PDB: 3QWD), *Bs*ClpP (PDB: 3TT6), and *Nm*ClpP (PDB: 7KR2). Identical, similar and non-conserved regions are highlighted in red boxes, red letters, and black letters respectively. There are no considerable variations in the E-helix (a5) and gly-rich portion (b7), regions involved in the heptamer-heptamer interactions. The residues of the catalytic triad, Ser98-His123-Asp172, are indicated by green asterisks. Sequence alignment was performed by EsPript3 server (Robert and Gouet 2014).

Figure 50 – (**a**) Catalytic triad of *Se*ClpP where the amino acid residues Ser98-His123-Asp172 interact via hydrogen bonds (active and extended conformation). On the other hand, in (**b**), His123 is flipped and far away from Ser98 (inactive and compressed conformation) in *Sa*ClpP (PDB: 3QWD). (**c**) shows that the gly-rich region and E-helix are organized in the extended *Se*ClpP. Stabilizing hydrogen bonds are in yellow (**c**), and the disordered gly-rich region and kinked E-helix in the compressed state are highlighted in (**d**).

Figure 51 – Impact of glycerol, a common chemical chaperone, on the *Se*ClpP state and hydrodynamic radius (R_H). (**a**) SEC chromatograms represent the samples free from glycerol (black curve) and containing it (red curve). In the second case, P1 starts being eluted earlier, and DLS measurements in (**b**) demonstrate that its R_H is approx. 17% higher.

Figure 52 – T-ramp experiments with (**a**) *Se*ClpP P1 free from glycerol (red curve) and (**b**) with 20% w/v glycerol (black curve). The T_{onset} for each set of measurements is presented here. R_h is the hydrodynamic radius in nanometers.

Figure 53 – Enzymatic assays with different glycerol concentrations.

Figure 54 – Details of the ClpP's catalytic site with glycerol and details of the network of hydrogen bonds with His123, Gly69, and Leu126 (yellow dashed lines). The hydrogen bonds in the catalytic triad are depicted as black dashed lines.

Figure 55 – Visualization of the network of hydrogen bonds (yellow dashes) connecting two opposing SeClpP subunits and the two heptameric rings, consequently. On the right side, the location of the extra bond is located within the ellipsis: it is the result of the interaction between the side chain of Gln130 and the backbone of Gly128.

Figure 56 – Enzymatic assays with Suc-LY-AMC, ixazomib, and 10% (w/v) glycerol. Control (0) is a sample free from ixazomib.

Figure 57 – ITC measurements with different ixazomib concentrations added to a ClpP sample supplemented by 10% (w/v) glycerol. After curve fitting, the following parameters were calculated: N = 9.53 ±0.0993 sites, K = 1.86E5 ±1.99E4 M^{-1}, ΔH= -1.390E4 ±198.0 cal/mol, and ΔS= -20.8 cal/mol/deg.

Figure 58 – Microcrystals of native SeClpP suitable for time-resolved serial crystallography.

List of Tables

Eidesstattliche Versicherung

Hiermit versichere ich an Eides statt, die vorliegende Dissertationsschrift selbst verfasst und keine anderen als die angegebenen Quellen und Hilfsmittel benutzt zu haben. Sofern im Zuge der Erstellung der vorliegenden Dissertationsschrift generative Künstliche Intelligenz (gKI) basierte elektronische Hilfsmittel verwendet wurden, versichere ich, dass meine eigene Leistung im Vordergrund stand und dass eine vollständige Dokumentation aller verwendeten Hilfsmittel gemäß der Guten wissenschaftlichen Praxis vorliegt. Ich trage die Verantwortung für eventuell durch die gKI generierte fehlerhafte oder verzerrte Inhalte, fehlerhafte Referenzen, Verstöße gegen das Datenschutz- und Urheberrecht oder Plagiat.

Hamburg, 02.08.2024   Bruno Alves França